Deliverable D3.5
Final publications

Contractual delivery date:

December 2014

Actual delivery date:

December 2014

Partner responsible for the Deliverable:

MPI

Authors:

Frank Nieuwenhuizen, Lewis Chuang

Dissemination level[1]		
PU	Public	X
PP	Restricted to other programme participants (including the Commission Services)	
RE	Restricted to a group specified by the consortium (including the Commission Services)	
CO	Confidential, only for members of the consortium (including the Commission Services)	

[1] Dissemination level using one of the following codes: **PU** = Public, **PP** = Restricted to other programme participants (including the Commission Services), **RE** = Restricted to a group specified by the consortium (including the Commission Services), **CO** = Confidential, only for members of the consortium (including the Commission Services)

Document Information Table

Grant agreement no.	ACPO-GA-2010-266470
Project full title	myCopter – Enabling Technologies for Personal Air Transport Systems
Deliverable number	D3.5
Deliverable title	Final publications
Nature[2]	R
Dissemination Level	PU
Version	1.0
Work package number	3
Work package leader	Max Planck Institute for Biological Cybernetics
Partner responsible for Deliverable	Max Planck Institute for Biological Cybernetics
Reviewer(s)	Prof. Dr. Heinrich H. Bülthoff

The research leading to these results has received funding from the European Community's Seventh Framework Programme (FP7/2007-2013) under grant agreement no 266470.

[2] Nature of the deliverable using one of the following codes: **R** = Report, **P** = Prototype, **D** = Demonstrator, **O** = Other

Revision Table

Version	Date	Modified Page/Section	Author	Comments
1.0	December 2014	Initial revision	Frank Nieuwenhuizen, Lewis Chuang	

Executive Summary

In this deliverable, we present the results of our human-machine interface prototype development and experimental studies related to haptic guidance and human factors for PAV flight. These studies cover a range of topics such as a prototype human-machine interface with Haptic shared control and a highway-in-the-sky display, the design of haptic aids, workload assessment with physiological metrics, looming warning signals and the development and identification of dynamic models of helicopters to aid the implementation of real-world augmentation strategies to aid non-expert pilots. All studies have been published and presented at European and international conferences.

Table of Contents

1. Haptic shared control and a highway-in-the-sky display for PAVs

In “Deliverable 3.4: Results from experiments”, we reported on an evaluation of a haptic shared control framework that was combined with a Highway-in-the-Sky display. An experiment was performed in which it was investigated whether this combination could result in better performance for non-expert pilots flying a personal aerial vehicle. Various representations of a flight trajectory in a highway-in-the-sky display were evaluated. It was found that a tunnel and a wall representation led to the best performance, whereas a highway representation resulted in worse performance and higher control activity and effort. Haptic guidance cues on the sidestick allowed pilots to achieve better performance with lower control activity.

The implementation of the haptic shared control framework in Deliverable 3.4 was limited to the roll degree of freedom. We have extended this prototype to include all degrees of freedom and demonstrated it to the general public and the press at the myCopter Project Day on 20 November 2014 in Braunschweig, Germany. Although no formal evaluation has been performed yet, anecdotal evidence suggests that anybody with at least some driving experience can easily get accustomed to the PAV flight dynamics and use the supplied haptic guidance cues to follow a flight trajectory without large deviations. Participants reported that they found the guidance forces in the various degrees of freedom very intuitive.

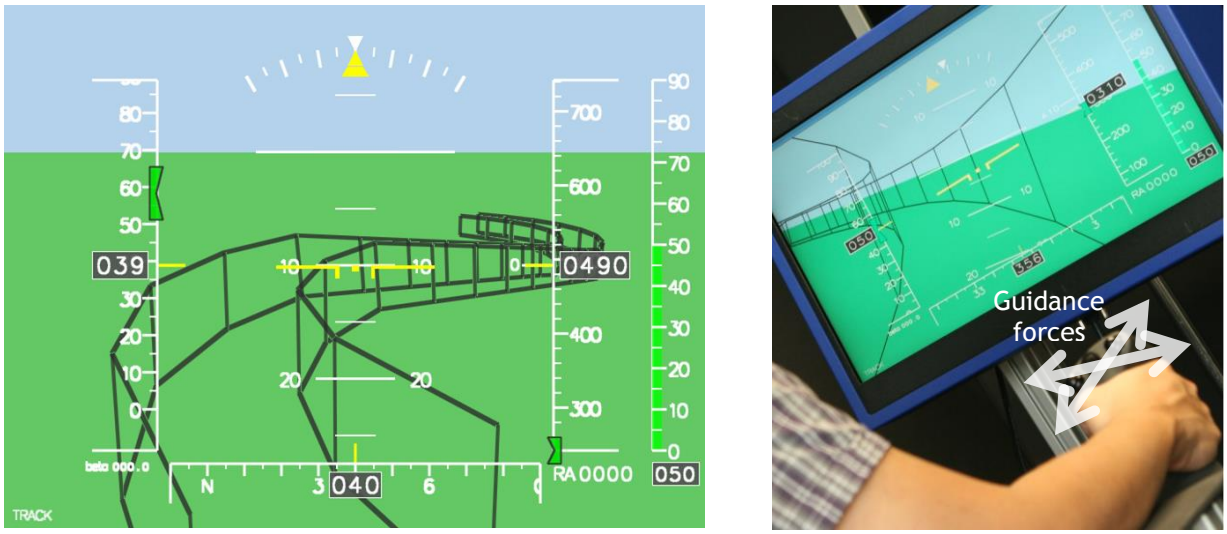

Left: An overview of a flight trajectory. Right: lateral guidance forces and velocity cues were provided to participants on a sidestick. Additionally, a collective lever was used to provide guidance forces related to the vertical changes in the flight path (not shown).

A participant is the fixed-base simulator that was used as a demonstrator at the myCopter Project Day in Braunschweig, Germany. The participant is wearing eye-tracking glasses to determine his gaze on the screen. The EEG electrodes are used for demonstration purposes to highlight the work of the Max Planck Institute for Biological Cybernetics towards assessing metrics for pilot workload measurements.

2. Pilot adaptation to different classes of haptic aids

This study was published in the Journal of Guidance, Control, and Dynamics:

M. Olivari, F. M. Nieuwenhuizen, H. H. Bülthoff and L. Pollini (2014) **Pilot Adaptation to Different Classes of Haptic Aids in Tracking Tasks** *Journal of Guidance, Control, and Dynamics* **37(6)** 1741-1753.

Abstract

Haptic aids have been largely used in manual control tasks to complement the visual information through the sense of touch. To analytically design a haptic aid, adequate knowledge is needed about how pilots adapt their visual response and the biomechanical properties of their arm (i.e., admittance) to a generic haptic aid. In this work, two different haptic aids, a direct haptic aid and an indirect haptic aid, are designed for a target tracking task, with the aim of investigating the pilot response to these aids. The direct haptic aid provides forces on the control device that suggest the right control action to the pilot, whereas the indirect haptic aid provides forces opposite in sign with respect to the direct haptic aid. The direct haptic aid and the indirect haptic aid were tested in an experimental setup with non-pilot participants and compared to a condition without haptic support. It was found that control performance improved with haptic aids. Participants significantly adapted both their admittance and visual response to fully exploit the haptic aids. They were more compliant with the direct haptic aid force, whereas they showed stiffer neuromuscular settings with the indirect haptic aid, as this approach required opposing the haptic forces.

JOURNAL OF GUIDANCE, CONTROL, AND DYNAMICS
Vol. 37, No. 6, November–December 2014

Pilot Adaptation to Different Classes of Haptic Aids in Tracking Tasks

Mario Olivari,* Frank M. Nieuwenhuizen,† and Heinrich H. Bülthoff‡
Max Planck Institute for Biological Cybernetics, 72012 Tübingen, Germany
and
Lorenzo Pollini§
University of Pisa, 56126 Pisa, Italy

DOI: 10.2514/1.G000534

Haptic aids have been largely used in manual control tasks to complement the visual information through the sense of touch. To analytically design a haptic aid, adequate knowledge is needed about how pilots adapt their visual response and the biomechanical properties of their arm (i.e., admittance) to a generic haptic aid. In this work, two different haptic aids, a direct haptic aid and an indirect haptic aid, are designed for a target tracking task, with the aim of investigating the pilot response to these aids. The direct haptic aid provides forces on the control device that suggest the right control action to the pilot, whereas the indirect haptic aid provides forces opposite in sign with respect to the direct haptic aid. The direct haptic aid and the indirect haptic aid were tested in an experimental setup with nonpilot participants and compared to a condition without haptic support. It was found that control performance improved with haptic aids. Participants significantly adapted both their admittance and visual response to fully exploit the haptic aids. They were more compliant with the direct haptic aid force, whereas they showed stiffer neuromuscular settings with the indirect haptic aid, as this approach required opposing the haptic forces.

I. Introduction

THE control of an aerial vehicle is a complex task that requires a pilot's continuous attention. Automated systems are commonly used to aid pilots during manual control tasks by accomplishing different functions with minimal or reduced human intervention [1]. However, previous studies have highlighted several issues concerning improper design of automation [2]. A main issue is that pilots are not aware of the control signal provided by the automated system. This could lead to a decrease in pilot vigilance, overreliance on automation, and loss of situational awareness [3,4]. To overcome these issues, an external aid should always inform pilots about its control strategy in order to keep the pilot in the loop [5].

Haptic aids have been proposed as a powerful approach to keep the pilot in the loop by providing a tactile feedback on the control device [6,7]. The pilot can sense the tactile feedback and is always aware of the haptic control strategy. A growing body of literature has investigated haptic aids for car-driving tasks [8,9] and for remotely piloted vehicles [10,11]. However, to the best of our knowledge, haptic aids are not commonly used in aviation, except as alert systems (e.g., stick shaker that warns pilots of an imminent stall [12]). Recently, researchers at NASA Langley developed a haptic flight control system (HFC) for aircrafts with the main goal of achieving easy-to-use personal air vehicles [13]. The HFC continuously moved the stick by repositioning its neutral point in order to perform a desired maneuver. Pilots can either follow the HFC control signal or override it if they disagreed with its control action. The HFC was evaluated in a motion-based simulator, showing beneficial effects in terms of pilot workload and situational awareness [13]. In a different research project (ALLFlight), the Institute of Flight Systems Germany (DLR) developed an HFC for an EC135 helicopter [14,15]. Similar to the NASA's system, this HFC was designed to move the stick to a position corresponding to a desired trajectory. Evaluations in flight showed workload reductions and improved situational awareness when the HFC was activated [15]. Although both studies found that tactile feedback can have beneficial effects from the pilot point of view, they did not investigate the possibility of using different designs of haptic aids.

The design of the force provided by the haptic aid becomes a crucial issue, because it has to represent information that pilots can easily exploit. Two different approaches have been proposed for designing the haptic aid: the direct haptic aid (DHA) and the indirect haptic aid (IHA) [16]. The DHA and IHA approaches are different in nature; however, both showed beneficial effects in terms of pilot performance [17]. This indicates that pilots are able to modify their control strategy in order to take advantage of both DHA and IHA approaches. The question arises as to how pilots adapt their control behavior in relation to different haptic aids.

Control behavior can be analyzed by looking at pilot's dynamic responses to the external cues [18,19]. In a control task with haptic and visual cues, two different dynamic responses need to be investigated: the visual response and the neuromuscular response [20,21]. The visual response describes the pilot response to the visual cue, whereas the neuromuscular response represents the dynamic settings of the pilot's arm and determines how the pilot interacts with forces (from disturbances or from haptic aids). Identification of these two responses during control tasks with different haptic aids will provide quantitative insights into the influence of haptic aids on pilot control behavior.

Identification of pilot visual responses has been widely addressed in the literature. McRuer's theories highlight that humans modify their visual response depending on external conditions such as the dynamics of the controlled element [22]. However, these theories do not consider the use of haptic cues, and, to the best of our knowledge, nobody has studied whether these rules are still valid when pilots are supported with haptic systems.

Presented as Paper 2012-4795 at the AIAA Modeling and Simulation Technologies Conference, Minneapolis, MN, 13–16 August 2012; received 1 February 2014; revision received 29 May 2014; accepted for publication 1 June 2014; published online 12 September 2014.

*Ph.D. Student, P.O. Box 2169; currently University of Pisa, 56126 Pisa, Italy; mario.olivari@tuebingen.mpg.de. Student Member AIAA.

†Research Scientist, P.O. Box 2169; frank.nieuwenhuizen@tuebingen.mpg.de. Member AIAA.

‡Professor and Director, P.O. Box 2169; currently Adjunct Professor, Department of Brain and Cognitive Engineering, Korea University, Seoul 136-713, South Korea; heinrich.buelthoff@tuebingen.mpg.de. Member AIAA.

§Assistant Professor, Dipartimento di Ingegneria dell'Informazione; lorenzo.pollini@dsea.unipi.it. Senior Member AIAA.

There is also a vast amount of literature on the human capabilities to adapt the neuromuscular response to the performed task. Research has focused on neuromuscular adaptation during disturbance–rejection tasks that require humans to adopt different neuromuscular settings in response to force disturbances on the control device [23–25]. More recent work has shown that the neuromuscular response in an aircraft tracking task with different dynamics of the control device is highly variable [26,27]. Other studies indicated that the ankle–foot neuromuscular response of car drivers changes when a haptic aid is employed during a car-following task [21]. The haptic aid was designed in order to suggest to pilots the right control action. These studies show that pilots adapt their neuromuscular response depending on the task they have to perform, and that haptic cues influence their neuromuscular response. However, these studies do not offer a complete discussion about how the neuromuscular response changes in relation to different kinds of haptic aid.

The goal of this paper is to obtain a quantitative insight into how the pilot neuromuscular and visual responses change with different haptic aids. Two haptic systems are tested in a tracking task, one designed according to the DHA approach, and the other according to the IHA approach. The two approaches provide haptic information in opposite ways and require humans to adopt different control strategies. The pilot neuromuscular and visual responses are estimated by using three different multiloop identification techniques. The first is based on cross-spectral density analysis (CSD-based method) and has been commonly used for identifying pilot responses [21,27]. However, a recent work showed that the CSD-based method might provide a biased estimate of neuromuscular response if a non-interference hypothesis is not fulfilled [28]. In the same study two novel approaches were proposed to overcome this issue [20,28]: a method based on autoregressive models with exogenous inputs (ARX method), and an adapted version of CSD for a multiloop tracking task (CSD-ML method). Our paper extends the ARX and CSD-ML methods to a tracking task with haptic aids, and compares the results with those obtained by the commonly used CSD-based method. Analysis of the estimates shed new light on how humans adapt their control behavior to take advantage of both haptic aids.

The paper is structured as follows: Section II outlines the design of the two haptic aids. Section III presents a model that can be used to describe pilot control behavior during a tracking task with a haptic aid. Identification methods suitable for this model are then detailed. The experimental procedure and setup are discussed in Sec. IV, followed by the experimental results in Sec. V. Finally, conclusions are drawn in Sec. VI.

II. Design of Haptic Aids for a Tracking Task

Haptic cues can be used as pilot support systems, with the main objective of increasing the level of safety and performance in a particular task. This paper focuses on a compensatory pitch tracking task as depicted in Fig. 1. This task involves the minimization of a tracking error e between a target trajectory θ_{tar} and the pitch angle θ_{CE} of the controlled element CE, i.e., the aircraft. The tracking error is shown on a compensatory display [18]. Haptic forces F_{hapt} are continuously presented on the control device. As will be explained in Sec. II.B, the forces provided by the haptic aid are combined with a neutral point shift δ_{NPS} of the control device in some cases. Based on both the visual information e and the haptic information felt through the deflection of control device δ_{CD}, the pilot generates a force F_{pilot} that results in a control action u. Two different approaches can be taken to design the haptic cue: the DHA and the IHA [16].

A. DHA Approach

The DHA approach consists of producing kinesthetic sensations that suggest the right control action to the pilot. This is achieved by designing the DHA force generation system as a standard compensator, which provides forces that reduce or regulate the tracking error to zero. Figure 2 shows an example of force given by the DHA system. With a negative tracking error e (pitch angle of aircraft too large), the force F_{hapt} provided by DHA pushes the control device in the forward direction. This generates a control signal u to the aircraft that makes it pitch down, thus reducing the tracking error.

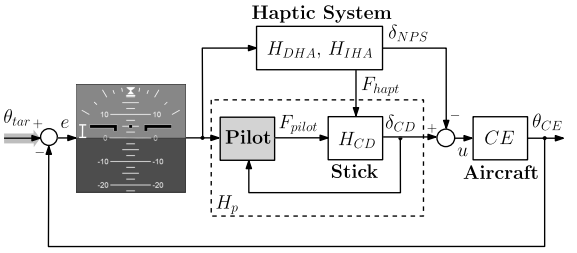

Fig. 1 Tracking task with compensatory display and haptic aids.

Although several techniques can be used to design a compensator, experience shows that many of these may lead to a haptic "controller" that generates stick motion differently from what the pilot would do to minimize the tracking error [29]. In such a case, the pilot may oppose the haptic cues instead of following them, which would result in degraded closed-loop performance. To overcome this issue, our approach is to design a DHA that "mimics" the pilot control strategy.

As described by McRuer's theories, pilots adapt their control strategy to yield pilot–aircraft open-loop dynamics that resemble a single integrator around the crossover frequency ω_c [22,30]:

$$H_p H_{\text{CE}} = \frac{\omega_c e^{-s\tau_e}}{s} \tag{1}$$

Here, H_{CE} is the transfer function of the controlled element CE, whereas H_p represents the pilot response as a transfer function between the tracking error e and the control signal u. Note that H_p includes the dynamics of both pilot and control device (see Fig. 1). The parameters ω_c and τ_e represent the pilot crossover frequency and the equivalent time delay, respectively. The values of these parameters depend on the dynamics H_{CE} and other external conditions.

To mimic pilot behavior, the dynamics of DHA were chosen to yield open-loop dynamics of the combined DHA–aircraft that resembles the crossover model in Eq. (1):

$$H_{\text{DHA}} H_{\text{CD}} H_{\text{CE}} = \frac{\omega_c e^{-s\tau_e}}{s} \tag{2}$$

where H_{DHA} and H_{CD} represent the transfer functions of the DHA and control device, respectively. Equation (2) describes the open-loop dynamics corresponding to the H_{DHA} without pilot's input. Contrary to Eq. (1), the open-loop dynamics in Eq. (2) includes the term H_{CD}. This is because the force provided by the DHA is not

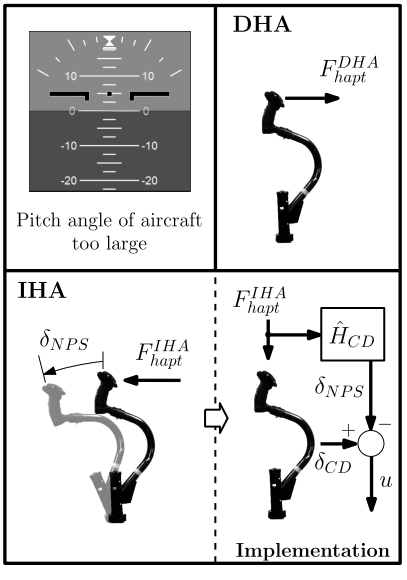

Fig. 2 DHA and IHA systems.

applied directly to CE, but passes through the dynamics of the control device. The dynamics H_{DHA} can be deduced from Eq. (2):

$$H_{\mathrm{DHA}} = \frac{\omega_c e^{-s\tau_e}}{sH_{\mathrm{CD}}H_{\mathrm{CE}}} \tag{3}$$

The resulting DHA force is given by

$$F_{\mathrm{hapt}}^{\mathrm{DHA}} = H_{\mathrm{DHA}} e \tag{4}$$

According to this design, the DHA can perform the tracking task without pilot in the loop. When the pilot is in the loop, haptic aid and pilot share the control of the aircraft. The pilot could either be as compliant as possible and follow the haptic aid, or try to amplify the forces to improve performance. In addition, the pilot could always override the haptic control strategy in case of discordance.

B. IHA Approach

Contrary to the DHA approach, the IHA is designed to inform pilots and increase situational awareness indirectly, and not to suggest control actions. The challenging design aspect of IHA is to convey the desired information in a way that appears natural to pilots. This approach has been adopted in different control tasks with the aim of exploiting the natural tendency of humans to counteract external forces presented on the control device. In some works dealing with wind gust rejection in teleoperation, a tactile disturbance was generated on the control device based on the effect of the wind gust on the controlled element [16]. By opposing the disturbance on the control device, pilots were able to reject the wind gust and control the trajectory of the controlled element. In other cases dealing with obstacle avoidance or with trajectory tracking, IHA systems were derived from a DHA system designed for the same goal by simply reversing the sign of the generated force [17,20,31,32]. The operator had to oppose the forces given by IHA to achieve the task also in these cases.

In our study, the IHA was designed to provide a force opposite in sign with respect to the DHA, i.e., opposite in sign to the force from a controller that reduces the tracking error. However, this design presents a considerable drawback: If the pilot is not in the loop or is not providing correct commands, the IHA force would generate a control action that would lead the aircraft to fly away from the target trajectory. It is clearly unwise to insert a possibly destabilizing component in the control loop. To overcome this issue, the neutral point of the control device is shifted according to the current force provided by the IHA system, so that the actual control command to the aircraft is zero when the pilot does not interact with the control device [32,33]. This allows the IHA system to provide sensations to the pilot (via the stick motion) without having an effect on the actual command given to the aircraft. Note that, according to this design, pilots can follow the target trajectory by simply holding the stick in the center. However, experimental evidence has shown that a pilot can improve the performance by actively responding to the resulting visual error.

The neutral point shift is implemented by using the compensation scheme shown in Fig. 2. The control device is subject to two external forces: the force applied by the pilot F_{human} and the force applied by the haptic system F_{hapt}. The deflection induced by F_{hapt} must become the new neutral point δ_{NPS}. To achieve this, the effect of F_{hapt} on the control device is simulated with a model of the control device $\hat{H}_{\mathrm{CD}}$ and subtracted from the actual position of the stick. This difference becomes the actual input u for the aircraft:

$$u = \delta_{\mathrm{CD}} - \delta_{\mathrm{NPS}} = \delta_{\mathrm{CD}} - \hat{H}_{\mathrm{CD}} F_{\mathrm{hapt}} \tag{5}$$

Figure 2 shows an example of an application of the IHA. With a negative tracking error (pitch angle of aircraft too large), the IHA generates a force that pulls the control device in the backward direction. The neutral point is shifted in the backward direction according to the IHA force, so that the control command provided to the aircraft is zero if the pilot is out of the loop. If the pilot counteracts the haptic force instead, he or she would move the control device to a more forward position than the neutral point. This generates a control signal to the aircraft that makes it pitch down, reducing the tracking error.

C. Comparison of the DHA and IHA Approaches

It is now possible to compare a general DHA with a general IHA with neutral point shift. Let us consider the behavior of the DHA and IHA in two different conditions: a pilot showing infinite compliance with a DHA system, and a pilot showing infinite stiffness with an IHA system. These conditions represent extreme situations in which pilots do not actively respond to the visual feedback, but adopt only a passive behavior that allows to take advantage of the two haptic aids. In the first case, the haptic force $F_{\mathrm{hapt}}^{\mathrm{DHA}}$ is the only force applied to the control device; thus, the resulting control signal u is given by

$$u^{\mathrm{DHA}} = H_{\mathrm{CD}} F_{\mathrm{hapt}}^{\mathrm{DHA}} \tag{6}$$

where H_{CD} represents the real transfer function of the control device. On the other hand, with IHA and an infinitely rigid pilot, the control device is constantly held in the center ($\delta_{\mathrm{CD}} = 0$). The resulting IHA control signal is thus caused only by the neutral point shift:

$$u^{\mathrm{IHA}} = \delta_{\mathrm{CD}} - \delta_{\mathrm{NPS}} = 0 - \delta_{\mathrm{NPS}} = -\hat{H}_{\mathrm{CD}} F_{\mathrm{hapt}}^{\mathrm{IHA}} \tag{7}$$

Under the hypothesis of an exact model of the control device ($H_{\mathrm{CD}} = \hat{H}_{\mathrm{CD}}$) and if the IHA force is calculated with the same dynamics as the DHA but opposite in sign (i.e., $F_{\mathrm{hapt}}^{\mathrm{IHA}} = -F_{\mathrm{hapt}}^{\mathrm{DHA}}$), the two approaches result in the same control signal for the aircraft: $u^{\mathrm{IHA}} = u^{\mathrm{DHA}}$. This analogy induced us to employ an identical design of the IHA and the DHA forces, except for a difference in sign. The full dynamics of both haptic aids will be detailed in Sec. IV.

III. Modeling and Identification of Pilot Control Behavior

In previous studies, the use of haptic cues based on DHA and IHA has shown beneficial effects in terms of pilot performance [8,17]. The question arises as to how pilots can take advantage of two haptic aids that actually feed forces opposite in sign into the control loop. This can be explained by the pilot capability of modifying the control strategy to handle different external conditions [34]. To gain a quantitative insight into how haptic cues influence pilot control strategy, a model of pilot control behavior is needed that can highlight the effects of haptic cues on the pilot's dynamic responses.

In a compensatory tracking task with haptic aid, two dynamic responses define the pilot control behavior: the visual response and the neuromuscular response [35]. The visual response describes how the pilot generates a control action based on the tracking error shown in the visual display. The neuromuscular response represents the dynamic settings of pilot's arm. By varying these settings, pilots can oppose, or be compliant with, the haptic aid. Thus, the neuromuscular response provides an indication of how the pilot interacts with haptic aids.

A model of pilot control behavior that includes both visual and neuromuscular responses was previously developed [35] and was used for various scenarios, such as a tracking task without haptic aid [35] and car following with haptic aid [21]. Figure 3 shows the model adapted for the task investigated in this paper, i.e., a compensatory tracking task with haptic aid. The pilot is described with two describing functions: the visual response VIS and the inverse of admittance ADM^{-1}. The visual response VIS describes the force response to the display presentation e. In the literature, the term "visual response" often denominates the response from e to the stick deflection δ_{CD}, i.e., the system H_{control} in Fig. 3 [18,27]. However, in a control task with haptic aids, H_{control} includes the dynamics of the haptic aid. Defining the visual response as the transfer function from e to F_{vis} allows us to separate the haptic system from the pilot responses.

The admittance ADM represents the dynamic properties of neuromuscular response and is defined as the causal relationship

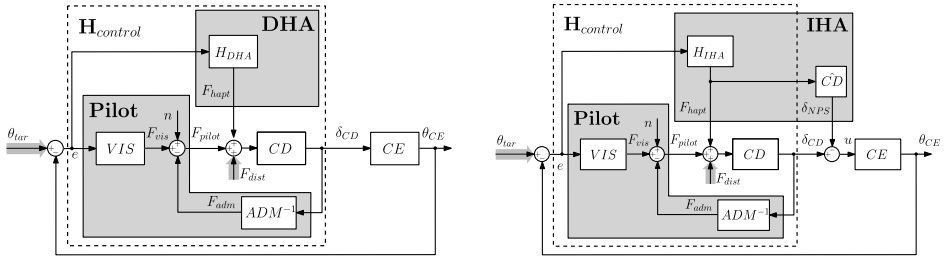

a) DHA **b) IHA**

Fig. 3 Model of pilot behavior in a compensatory tracking task with a haptic aid.

between the force acting on the arm (input) and the position of the arm (output) [36]. Higher values of admittance during the tracking task indicate that pilots are compliant with the haptic aid, whereas lower values indicate that pilots are counteracting the force provided by the haptic aid. It is possible to measure the range in which admittance varies by performing disturbance–rejection tasks, the so-called *classical tasks* [36]. These tasks consist of minimizing the stick deflection δ_{CD} (position task, PT), relaxing the arm (relax task, RT), and minimizing the force F_{pilot} applied on the control device (force task, FT), in response to force disturbances on the control device. The PT and FT force pilots to adopt minimum and maximum admittance, respectively, whereas the RT highlights inertial properties of the arm [36].

For the purposes of this study, the two blocks VIS and ADM^{-1} are assumed to be linear. Noise and nonlinear contributions to the pilot force F_{pilot} are accounted for by the remnant signal n [22]. The blocks H_{DHA} and H_{IHA} represent transfer functions of the DHA and IHA, respectively. Both the DHA and IHA generate a force F_{hapt} on the control device based on the dynamics of the visual error e. The force generated by the haptic aid is sensed by pilots through its effect on the deflection of the control device δ_{CD}. The signal δ_{NPS} represents the neutral point shift used in the IHA approach. As explained in Sec. II, the dynamics of δ_{NPS} are calculated by simulating the effect of the haptic force F_{hapt} on the identified dynamics $\widehat{CD}$ of the control device. In the DHA approach, δ_{NPS} is absent.

Identification of the model in Fig. 3 allows for an evaluation of how haptic cues influence a pilot's admittance and visual response. Because two dynamic responses need to be estimated, i.e., the admittance and the visual response, identification methods require two external forcing functions to be inserted into the control loop [37]. The target trajectory θ_{tar} and an additional disturbance force on the control device F_{dist} can be used for this purpose. Figure 4 shows power spectral densities and time realizations of the two forcing functions adopted in our experiment. Their design will be detailed in Sec. IV. For now, we would indicate that F_{dist} and θ_{tar} are chosen to have power at different sets of frequency points, $\{f_d\}$ and $\{f_t\}$, respectively.

Three different identification techniques are used in this paper: a CSD-based method, an ARX method, and a novel CSD-ML method [20,28]. These three methods were tested and compared in a previous study dealing with a compensatory tracking task without haptic aids [28]. This paper extends their applicability to the presence of a haptic aid.

The CSD-based method has been largely applied to multiloop pilot identification [21,27]. This method estimates the frequency response function (FRF) of the admittance at frequencies in $\{f_d\}$ by using sample cross-spectral densities:

$$\hat{H}_{\mathrm{adm}}(f) = \frac{\hat{S}_{F_{\mathrm{dist}}\delta_{\mathrm{CD}}}(f)}{\hat{S}_{F_{\mathrm{dist}}F_{\mathrm{pilot}}}(f)}, \qquad f \in \{f_d\} \tag{8}$$

The term $\hat{S}_{vw}$ indicates the sample CSD between the generic signals v and w, which is calculated as

$$\hat{S}_{vw}(f) = \bar{V}(f)W(f) \tag{9}$$

where V and W are the discrete Fourier transforms of v and w, respectively, and $\bar{V}$ indicates the complex conjugate of V [38]. The squared coherence function $\hat{\Gamma}^2$ is usually used to evaluate the reliability of the estimate [39]:

$$\hat{\Gamma}^2_{\mathrm{adm}}(f) = \frac{|\hat{S}_{F_{\mathrm{dist}}\delta_{\mathrm{CD}}}(f)|^2}{\hat{S}_{F_{\mathrm{dist}}F_{\mathrm{dist}}}(f)\hat{S}_{\delta_{\mathrm{CD}}\delta_{\mathrm{CD}}}(f)}, \qquad f \in \{f_d\} \tag{10}$$

The coherence $\hat{\Gamma}^2$ is a measure of how much an output signal is linearly related to an input signal [40]. It assumes values between 0 and 1 and decreases with noise and nonlinearities.

The FRF of the pilot visual response cannot be estimated directly with the CSD-based method [28]. On the other hand, the FRF of the control transfer function H_{control} between the visual error e and the deflection of the control device δ_{CD} can be estimated at the frequencies $\{f_t\}$ according to

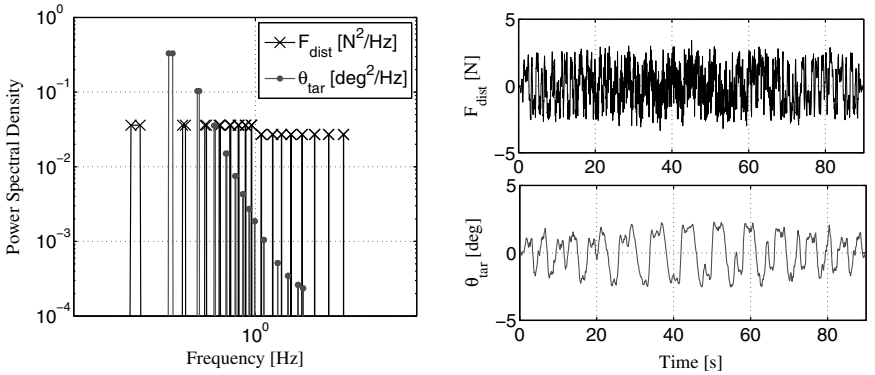

a) Power spectral densities **b) Time realizations**

Fig. 4 Forcing signals θ_{tar} and F_{dist}.

$$\hat{H}_{\text{control}}(f) = \frac{\hat{S}_{\theta_{\text{tar}}\delta_{\text{CD}}}(f)}{\hat{S}_{\theta_{\text{tar}}e}(f)}, \qquad f \in \{f_t\} \tag{11}$$

The squared coherence function corresponding to $\hat{H}_{\text{control}}$ is given by

$$\hat{\Gamma}^2_{\text{control}}(f) = \frac{|\hat{S}_{\theta_{\text{tar}}\delta_{\text{CD}}}(f)|^2}{\hat{S}_{\theta_{\text{tar}}\theta_{\text{tar}}}(f)\hat{S}_{\delta_{\text{CD}}\delta_{\text{CD}}}(f)}, \qquad f \in \{f_t\} \tag{12}$$

Similarly, the open-loop transfer function between the visual error e and the position of the controlled element θ_{CE} and the corresponding squared coherence function are estimated as

$$\hat{H}_{\text{OL}}(f) = \frac{\hat{S}_{\theta_{\text{tar}}\theta_{\text{CE}}}(f)}{\hat{S}_{\theta_{\text{tar}}e}(f)}, \qquad f \in \{f_t\} \tag{13}$$

$$\hat{\Gamma}^2_{\text{OL}}(f) = \frac{|\hat{S}_{\theta_{\text{tar}}\theta_{\text{CE}}}(f)|^2}{\hat{S}_{\theta_{\text{tar}}\theta_{\text{tar}}}(f)\hat{S}_{\theta_{\text{CE}}\theta_{\text{CE}}}(f)}, \qquad f \in \{f_t\} \tag{14}$$

As previous works have highlighted, the CSD-based method requires that the contribution of the disturbance force F_{dist} in the visual error is negligible (*noninterference hypothesis*) [20,28]. If the noninterference hypothesis is not fulfilled, the CSD-based method provides a biased estimate of the admittance even with high values of $\hat{\Gamma}^2_{\text{adm}}$. In such cases, the ARX and CSD-ML methods can be employed. These methods do not require any noninterference hypothesis, because they explicitly account for the possible presence of the contribution of F_{dist} in the visual error [20,28].

The ARX method operates in the time domain. The method considers the stick deflection δ_{CD} as the output of a linear system with inputs e and F_{dist} (see Fig. 3):

$$\delta_{\text{CD}} = H_e e + H_F F_{\text{dist}} + H_n n \tag{15}$$

where H_e, H_F, and H_n represent the transfer functions between e and δ_{CD}, between F_{dist} and δ_{CD}, and between n and δ_{CD}, respectively. Note that H_e, H_F, and H_n depend on the values of the transfer functions H_{adm}, H_{vis}, H_{CD}, and H_{HAPT}.

The linear system in Eq. (15) is fitted with a multi-input linear ARX model, which provides estimates of H_e and H_F as polynomial transfer functions [38]. The pilot admittance $\hat{H}_{\text{adm}}$, the visual response $\hat{H}_{\text{vis}}$, the control transfer function $\hat{H}_{\text{control}}$, and the open-loop transfer function $\hat{H}_{\text{OL}}$ are then calculated from the estimates $\hat{H}_e$ and $\hat{H}_F$ and from the known transfer functions H_{CD}, H_{HAPT}, H_{NPS}, and H_{CE} by using block diagram algebra:

$$\hat{H}_{\text{adm}} = \frac{H_{\text{CD}}\hat{H}_F}{H_{\text{CD}} - \hat{H}_F} \tag{16}$$

$$\hat{H}_{\text{vis}} = \frac{\hat{H}_e - H_{\text{HAPT}}\hat{H}_F}{\hat{H}_F} \tag{17}$$

$$\hat{H}_{\text{control}} = \hat{H}_e \tag{18}$$

$$\hat{H}_{\text{OL}} = (\hat{H}_e - H_{\text{NPS}})H_{\text{CE}} \tag{19}$$

Here, H_{HAPT} represents the force generation dynamics of the haptic aid ($H_{\text{HAPT}} = H_{\text{DHA}}$ and $H_{\text{HAPT}} = H_{\text{IHA}}$ for DHA and IHA, respectively). H_{NPS} describes the dynamics according to which the neutral point shift is calculated from the tracking error. In the DHA approach, $H_{\text{NPS}} = 0$ because there is no neutral point shift, whereas in the IHA approach, $H_{\text{NPS}} = H_{\text{HAPT}}H_{\text{CD}}$. Note that the estimates $\hat{H}_{\text{vis}}$ and $\hat{H}_{\text{adm}}$ account only for pilot contributions, because the dynamics of haptic aids are removed by using block diagram algebra. On the other hand, the systems $\hat{H}_{\text{control}}$ and $\hat{H}_{\text{OL}}$ also include the haptic dynamics (see Fig. 3).

To test how well the estimated ARX model predicts the measured output signal, the variance accounted for (VAF) index can be calculated [41]. The VAF is defined as

$$\text{VAF} = \left[1 - \frac{\sum_{k=1}^{N} |\delta_{\text{CD}}(t_k) - \hat{\delta}_{\text{CD,ARX}}(t_k)|^2}{\sum_{k=1}^{N} |\delta_{\text{CD}}(t_k)|^2}\right] \times 100\% \tag{20}$$

where t_k represent the time samples, and δ_{CD} and $\hat{\delta}_{\text{CD,ARX}}$ are the measured and predicted (by the ARX model) deflection of the control device, respectively. The value of the VAF varies between 0% and 100%, with 100% indicating that the ARX model perfectly models the measured output signal.

The CSD-ML operates in the frequency domain. This method first uses estimates of cross-spectral densities to calculate the FRF $\hat{H}_{\text{tar}}$ between θ_{tar} and δ_{CD}, and the FRF $\hat{H}_{\text{dist}}$ between F_{dist} and δ_{CD}:

$$\hat{H}_{\text{tar}}(f) = \frac{\hat{S}_{\theta_{\text{tar}}\delta_{\text{CD}}}(f)}{\hat{S}_{\theta_{\text{tar}}\theta_{\text{tar}}}(f)} \tag{21}$$

$$\hat{H}_{\text{dist}}(f) = \frac{\hat{S}_{F_{\text{dist}}\delta_{\text{CD}}}(f)}{\hat{S}_{F_{\text{dist}}F_{\text{dist}}}(f)} \tag{22}$$

In our experiment, the forcing functions F_{dist} and θ_{tar} were designed to have power at different sets of frequencies, $\{f_d\}$ and $\{f_t\}$, respectively (see Fig. 4). This implies that $\hat{H}_{\text{dist}}$ can be estimated only on frequencies $\{f_d\}$, and $\hat{H}_{\text{tar}}$ on frequencies $\{f_t\}$.

To obtain estimates of $\hat{H}_{\text{tar}}$ and $\hat{H}_{\text{dist}}$ on a common set of frequencies, the CSD-ML method applies an interpolation procedure. More precisely, the values $\hat{H}_{\text{dist}}(f_d)$ are interpolated to estimate $\hat{H}_{\text{dist}}$ at frequencies in $\{f_t\}$, and the values $\hat{H}_{\text{tar}}(f_t)$ are interpolated to estimate $\hat{H}_{\text{tar}}$ at frequencies in $\{f_d\}$. Note that extrapolation of the values $\hat{H}_{f_d}(f_t)$ at frequencies outside the range of $\{f_t\}$ would give unreliable estimates. Because the range of $\{f_t\}$ is smaller than the range of $\{f_d\}$ (see Fig. 4), $\hat{H}_{\text{tar}}$ cannot be estimated on all the frequencies $\{f_d\}$, but only on those frequencies of $\{f_d\}$ that are within the range of $\{f_t\}$. These frequencies, together with the frequencies in $\{f_t\}$, constitute the set $\bar{f}$ in which both $\hat{H}_{\text{dist}}$ and $\hat{H}_{\text{tar}}$ can be calculated:

$$f_{\min} = \max(\min\{f_t\}, \min\{f_d\}) \tag{23}$$

$$f_{\max} = \min(\max\{f_t\}, \max\{f_d\}) \tag{24}$$

$$\bar{f} = \{f | f \in (\{f_t\} \cup \{f_d\}) \text{ and } f_{\min} \le f \le f_{\max}\} \tag{25}$$

After $\hat{H}_{\text{tar}}$ and $\hat{H}_{\text{dist}}$ have been estimated for the common set of frequencies $\bar{f}$, they are combined using block diagram algebra to obtain estimates of the admittance $\hat{H}_{\text{adm}}$, the visual response $\hat{H}_{\text{vis}}$, the control transfer function $\hat{H}_{\text{control}}$, and the open-loop transfer function $\hat{H}_{\text{OL}}$. Expressions for $\hat{H}_{\text{adm}}$, $\hat{H}_{\text{vis}}$, $\hat{H}_{\text{control}}$, and $\hat{H}_{\text{OL}}$ are given as follows:

$$\hat{H}_{\text{adm}}(f) = \frac{\hat{H}_{\text{dist}}(f)H_{\text{CD}}(f)}{H_{\text{CD}}(f) - H_{\text{CD}}(f)\hat{H}_{\text{tar}}(f)H_{\text{CE}}(f) - \hat{H}_{\text{dist}}(f)} \tag{26}$$

$$\hat{H}_{\text{vis}}(f) = -H_{\text{HAPT}}(f) + \frac{\hat{H}_{\text{tar}}(f)}{\hat{H}_{\text{dist}}(f)}[1 - H_{\text{NPS}}(f)H_{\text{CE}}(f)] \tag{27}$$

$$\hat{H}_{\text{control}}(f) = \frac{\hat{H}_{\text{tar}}(f) - H_{\text{NPS}}(f)}{1 - \hat{H}_{\text{tar}}(f)H_{\text{CE}}(f)} + H_{\text{NPS}}(f) \tag{28}$$

$$\hat{H}_{\mathrm{OL}}(f) = H_{\mathrm{CE}}(f)\frac{\hat{H}_{\mathrm{tar}}(f) - H_{\mathrm{NPS}}(f)}{1 - \hat{H}_{\mathrm{tar}}(f)H_{\mathrm{CE}}(f)}, \qquad f \in \{\bar{f}\} \tag{29}$$

These expressions are essentially the same as those for a generic closed-loop control task [28] but include the influence of the DHA and IHA.

IV. Experiment Design for Identification of Pilot Behavior

An experiment was conducted to investigate the effects of different haptic aids on human behavior in a pitch tracking task. The experimental design and hypotheses are described in this section.

A. Control Task and Apparatus

The experiment was designed to evaluate human behavior in a compensatory pitch tracking task with haptic aids as described in Sec. II. The experimental setup is shown in Fig. 5. Participants had to minimize the error between the target signal θ_{tar} and the pitch attitude of the controlled element θ_{CE}. Only the tracking error was shown on the visual display. During the tracking task, participants were provided with continuous haptic information as additional forces on the control device. In addition to the haptic aid, the control device was perturbed by the disturbance force F_{dist} introduced to allow identification of the neuromuscular admittance.

The control device was a control-loading cyclic stick from Wittenstein Aerospace & Simulation GmbH, Germany, which can provide force feedback to participants. The stick dynamics were estimated and are given by

$$H_{\mathrm{CD}}(s) = \frac{1}{1.522s^2 + 8.832s + 86.469}\ [\mathrm{rad/N}] \tag{30}$$

During the experiment, the lateral axis of the stick was fixed, leaving the longitudinal axis free for performing the control task. No armrest was present for the arm that controlled the stick, and subjects were asked not to use their legs as support. All the components were driven by a real-time computer running xPC Target (MathWorks, Inc.) and data were logged at 100 Hz.

B. Independent Variables

To investigate the effects of haptic aids on human behavior, different approaches were implemented to provide the force feedback on the control device. The independent variable in this experiment was the approach used to design the haptic aid. Two haptic aids designed according DHA and IHA approaches were tested and compared to a baseline tracking condition without haptic aid. This resulted in three experimental conditions.

Fig. 5 Experimental setup.

C. Controlled Element and Haptic Aid Dynamics

The controlled element was simulated using the following dynamics:

$$H_{\mathrm{CE}} = \frac{18}{s(s+3)}\ [\mathrm{rad/rad}] \tag{31}$$

These dynamics, although idealized and not representative of a wide range of aircrafts, have been commonly used to investigate pilot behavior in tracking tasks [30,42]. At higher frequencies, the selected dynamics are similar to a double integrator, which are difficult to control for a participant. These dynamics are expected to accentuate the differences in human performance between different haptic aid conditions.

The design of the DHA and IHA was extensively explained in Sec. II. To make sure that the haptic aid is designed such that it behaves similarly to the human, values for the human crossover frequency ω_c and the equivalent time delay τ_e were estimated during a preliminary design phase for a tracking task without haptic aids. The preliminary study used the same apparatus, controlled element, and target signal as the real experiment. The resulting values were $\omega_c = 2$ rad/s and $\tau_e = 0.16$ s. These values were comparable with values found in a previous study with similar experimental conditions [30]. The dynamics of the DHA were then chosen as in Eq. (3), but the delay τ_e in Eq. (3) was set to 0 s instead of the value estimated in the preliminary design phase, so that the haptic response was slightly faster than the human response. This was expected to improve the help provided by the haptic aid. Furthermore, the dynamics of the control device H_{CD} were approximated by its static gain $K_{\mathrm{CD}} = H_{\mathrm{CD}}|_{s=0}$, as H_{CD} behaves like a gain at frequencies around ω_c, where the crossover model provides reliable estimates for the human behavior. Finally, an additional pole was placed at high frequency to ensure causality of H_{DHA}. The resulting dynamics H_{DHA} are given by

$$H_{\mathrm{DHA}} = \frac{\omega_c}{sK_{\mathrm{CD}}H_{\mathrm{CE}}} \cdot \frac{1}{0.05s+1} \approx 10\frac{s+3}{0.05s+1}\ [\mathrm{N/rad}] \tag{32}$$

The corresponding DHA force is given by Eq. (4).

As detailed in Sec. II, the IHA force was generated with the same dynamics of the DHA force but opposite in sign. Thus, the dynamics of the IHA are given as

$$H_{\mathrm{IHA}} = -H_{\mathrm{DHA}} \tag{33}$$

and the IHA force as

$$F_{\mathrm{hapt}}^{\mathrm{IHA}} = H_{\mathrm{IHA}}e \tag{34}$$

The IHA was combined with a neutral point shift. The dynamics of the neutral point δ_{NPS} are calculated as explained in Sec. II:

$$\delta_{\mathrm{NPS}} = \hat{H}_{\mathrm{CD}}F_{\mathrm{hapt}}^{\mathrm{IHA}} \tag{35}$$

D. Forcing Functions

The two forcing functions F_{dist} and θ_{tar} were designed as multisine signals [43]:

$$\theta_{\mathrm{tar}}(t) = \sum_{j=1}^{N_t} T_j\ \sin(2\pi f_{T_j}t + \psi_{T_j}) \tag{36}$$

$$F_{\mathrm{dist}}(t) = \sum_{j=1}^{N_d} D_j\ \sin(2\pi f_{D_j}t + \psi_{D_j}) \tag{37}$$

Each frequency f_{T_j} and f_{D_j} was chosen as an integer multiple of the experimental base frequency $f_B = 1/T$, where T is the measurement

time. The measurement time of an individual trial was $T = 81.92$ s, yielding a base frequency $f_B = 0.0122$ Hz.

To distinguish the contribution of each forcing function to the measurements, different sets of frequency points were assigned to F_{dist} and θ_{tar} [36] (see Fig. 4a). The two sets consisted of cluster of two adjacent frequency points to allow for frequency averaging.

The force disturbance F_{dist} contained power at frequencies from 0.01 up to 10 Hz, to allow for estimation of admittance on a large range of frequencies. The power level at low frequencies, from 0.01 up to 1 Hz, was set to 1.2 N^2 and distributed among linearly spaced frequencies. In this way, the contribution of F_{dist} on the measurements could be distinguished while participants were not disturbed during the tracking task. At high frequencies, from 1 up to 10 Hz, the power level was set to 0.8 N^2 and distributed among logarithmically spaced frequencies according to the reduced power method [44]. In this method, reduced power is applied at high frequencies in order to enable estimation of the admittance at high frequencies without influencing low-frequency behavior.

The target signal θ_{tar} contained power at frequencies from 0.1 up to 3 Hz. To avoid crossover regression, the distribution of the amplitudes T_j was shaped according to the following filter [43,45]:

$$H_f = \frac{(s+10)^2}{(s+1.25)^2} \tag{38}$$

For both θ_{tar} and F_{dist}, the phases were chosen randomly to obtain unpredictable behavior. A cresting technique was applied to avoid amplitude peaks in the time realization [39,46]. Figure 4b shows the time realizations of F_{dist} and θ_{tar}. Note that both forcing signals were smoothed in the first and in the last 2 s of the experimental time interval to avoid transient effects.

E. Haptic System Performance and Influence of Force Disturbance

According to our design of haptic aids, participants could perform the task by adopting a passive behavior, i.e., by being as compliant as possible with DHA, and by holding the stick in the center with IHA. In these cases, the control input to the aircraft is essentially provided by the haptic aid. Analysis of performance and control activity in these extreme situations is crucial to understand how much participants add to the haptic control action during the real experiment. It is also important to test these situations with and without injecting the F_{dist} signal that must be present during the experiment with pilots for identification purposes.

Table 1 shows the variances of the force F_{hapt}, the stick deflection δ_{CD}, the neutral point shift δ_{NPS}, and the tracking error e, obtained in this two extreme situations: human showing infinite compliance with DHA, and human holding the stick in the center with IHA. The first two columns show the results without F_{dist}. It is possible to note that

1) $\sigma^2(F_{\text{hapt}}^{\text{DHA}}) \approx \sigma^2(F_{\text{hapt}}^{\text{IHA}})$
2) $\sigma^2(\delta_{\text{CD}}^{\text{DHA}}) \approx \sigma^2(\delta_{\text{NPS}}^{\text{IHA}})$
3) $\sigma^2(e^{\text{DHA}}) \approx \sigma^2(e^{\text{IHA}})$

These equalities are in complete agreement with the haptic aid design concepts explained in Sec. IV.C.

The last two columns of Table 1 show the variances obtained when F_{dist} is chosen as in Eq. (37). The IHA is not influenced by the disturbance force. In fact, the stick is clamped in the center with an infinitely stiff pilot, and F_{dist} does not result in any disturbance to the aircraft. However, the values of DHA variances change when F_{dist} is chosen as in Eq. (37). This is because the force disturbance F_{dist} actually deflects the control device and thus becomes a disturbance input for the aircraft.

Table 1 Measures for haptic aids with passive pilot

	No F_{dist}		With F_{dist}	
	DHA	IHA	DHA	IHA
$\sigma^2(F_{\text{hapt}})$ [N^2]	0.72	0.70	2.35	0.70
$\sigma^2(\delta_{\text{CD}})$ [deg^2]	0.45	0	2.18	0
$\sigma^2(\delta_{\text{NPS}})$ [deg^2]	0	0.44	0	0.44
$\sigma^2(e)$ [deg^2]	0.55	0.54	2.00	0.54

F. Participants and Experimental Procedure

Eight participants took part in the experiment, seven men and one woman. All participants were Ph.D. students at the Max Planck Institute for Biological Cybernetics, and some had general experience with flight simulators and closed-loop control tasks. A financial compensation was offered for their participation. Before starting the experiment, participants received instructions about the objective of the experiment and the control tasks they would perform.

The experiment was split into two parts. The first part consisted of measuring admittance during force–disturbance–rejection tasks, the so-called classical tasks. Participants were asked to adopt three different control behaviors in response to a disturbance force applied to the control device [47]:

1) RT: Participants relaxed their arm and adopted a passive behavior. The display was turned off to prevent any distraction.

2) PT: Participants minimized the stick deviation by resisting the disturbance force. The display showed the stick deviation to help participants perform the task.

3) FT: Participants were compliant with the disturbance force and minimized the force applied to the stick. During the first trials, the display showed the force applied to the stick. After some training, the display was switched off.

During PT trials, participants must adopt maximum stiffness (low admittance), whereas during FT trials participants must adopt minimum stiffness (high admittance). Identification of admittance in these two tasks thus gives an indication of the range over which admittance changes. On the other hand, the RT trials allow for an evaluation of the inertial properties of the arm. The disturbance force for the classical tasks was designed as a multi-sine signal similar to F_{dist} used in tracking tasks, but with different power at low frequencies. The power at low frequencies was varied between the three tasks to obtain the same standard deviation of the stick deflection for all classical tasks. In this way, nonlinearities of the neuromuscular system due to large stick deflections were negligible. The values of the power at low frequencies for FT, RT, and PT were approximately chosen 1, 1.5, and 6.5 times larger than in the tracking task, respectively.

To avoid learning effects, the three classical tasks were presented in a counterbalanced order between participants using a Latin square matrix [48]. Participants were trained on each task until a stable performance was achieved. The performance was evaluated using the variance of the stick deflection for the PT and RT, and the variance of the force applied by participants for the FT. After the training phase, three 90 s runs of each task were performed for averaging purposes.

The second part of the experiment consisted of the compensatory tracking task. Participants were instructed to minimize the tracking error shown on the compensatory display. Three different tracking conditions were investigated, i.e., tracking with No Haptic Aid (NoHA), tracking with DHA, and tracking with IHA. In each condition, participants were informed on the possible presence of haptic aids, but they were not informed of how the haptic aids were designed. This was done to reduce the possibility that participants would have focused only on following or opposing the force generated by the haptic aid, instead of actively performing the tracking task. The conditions were presented in counterbalanced order between participants using a Latin square matrix. For each condition, participants performed a training phase and a measurement phase. During the training phase, a number of runs were executed until participants achieved a stable performance evaluated using the variance of the tracking error. After the training phase, eight repetitions of the condition were executed and measurement data were recorded. Participants took regular breaks during the experiment. The whole experiment lasted approximately 3 h.

G. Dependent Measures

During the experiment, the force F_{hum}, the stick deflection δ_{CD}, and the visual error e were logged at 100 Hz. The experimental time

was 90 s, of which 81.92 s was considered for data analysis. To reduce the noise, the measured signals were averaged in the time domain over all repetitions of each experimental condition (NoHA, DHA, and IHA).

A number of dependent measures were calculated from the recorded data. The variance of the tracking error e was calculated as a measure of tracking performance:

$$\sigma^2(e) = \frac{\sum_{k=1}^{N} [e(k) - \bar{e}]^2}{N} \tag{39}$$

where N represents the number of time samples and $\bar{e}$ is the mean value of the visual error. Lower values of $\sigma^2(e)$ indicate better tracking performance. The control activity was evaluated using the variance of control signal δ_{CD}. The variance of the force F_{pilot} was calculated as an indication of the amount of force needed by participants to perform the tracking task. A one-way repeated measures analysis of variance (ANOVA) was used to investigate the statistical effect of the haptic aid on the measured variance metrics. For each ANOVA, the hypothesis of sphericity was tested by Mauchly's test. If data violate the sphericity hypothesis, the values of the F-ratio cannot be compared to tabulated values of the F-distribution. In this case, the Greenhouse–Geisser correction was applied [49]. The correction adjusts the degrees of freedom of the F-ratio to make the F-ratio more conservative and comparable to the tabulated values. Post-hoc tests using the Bonferroni correction were performed to allow for pairwise comparisons between the three tracking conditions. This correction uses a reduced critical level to test statistical significance of each pairwise comparison.

Furthermore, the measured signals were used to identify and compare pilot control behavior between the experimental conditions. The identification methods detailed in Sec. III were used to estimate the admittance, the visual response, and the open-loop transfer function. To reduce the variance of the estimates given by the CSD-based and CSD-ML methods, the estimates were averaged over each cluster of frequency points [50]. The estimates of H_{adm}, H_{vis}, $H_{control}$, and H_{OL} were compared by looking at their FRFs. In addition, the estimates of H_{adm} during the tracking tasks were compared with the admittances estimated during the classical tasks. For the classical tasks, admittance was estimated according to the CSD-based method shown in Eq. (8). In these tasks, the method provides unbiased estimates (contrary to during the tracking tasks) [20].

H. Hypotheses

Both DHA and IHA are expected to yield better tracking performance with respect to the tracking task with NoHA, because they are designed to help humans achieve their task. Furthermore, it is hypothesized that participants would adapt their admittance depending on the haptic aid. Because the DHA is designed to be followed by humans, participants are expected to be more compliant in the DHA condition, resulting in higher admittance values. Instead, the IHA system is designed as a disturbance that the human needs to reject, and thus participants are expected to show a stiffer neuromuscular setting, resulting in lower admittance values. During the NoHA condition, the admittance is expected to lay in the middle of the two previous cases.

Finally, it is hypothesized that the haptic aid would also influence the participants' visual response. Because the DHA provides a portion of the control action needed to track the target, a smaller control action is needed from the participants. The visual response is therefore expected to have a lower gain in DHA than during the other two conditions.

V. Results of Pilot Adaptation to Different Haptic Aids

This section presents the experimental results of the eight participants. Tracking performance and control effort are compared between the tracking conditions with and without haptic aids. The influence of haptic aids on human control behavior is investigated by estimating participants' admittance, the visual response, and the

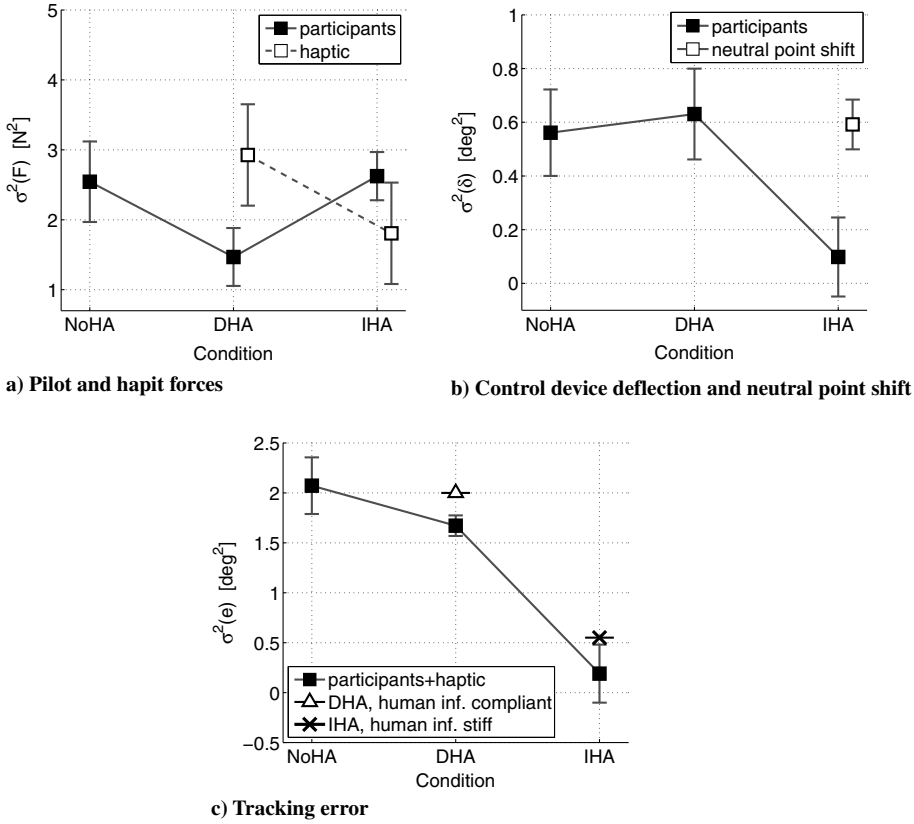

a) Pilot and hapit forces

b) Control device deflection and neutral point shift

c) Tracking error

Fig. 6 Means and 95% confidence intervals of measured variance over all participants.

Table 2 Results of post-hoc tests with Bonferroni correction for $\sigma^2(\cdot)$ data

Independent variables	Dependent measures					
	$\sigma^2(F_{\text{pilot}})$		$\sigma^2(\delta_{\text{CD}})$		$\sigma^2(e)$	
Factor	p	Significance	p	Significance	p	Significance
DHA vs NoHA	0.091	[a]	1.000	[c]	0.057	[a]
IHA vs NoHA	1.000	[c]	0.011	[b]	0.000	[b]
IHA vs DHA	0.003	[b]	0.007	[b]	0.000	[b]

[a]Significant ($0.050 \leq p < 0.100$).
[b]Highly significant ($p < 0.050$).
[c]Not significant ($p \geq 0.100$).

open-loop transfer function using the CSD-based, CSD-ML, and ARX methods detailed in Sec. III.

A. Tracking Performance and Control Activity

To evaluate the control effort, the variance of participant force $\sigma^2(F_{\text{pilot}})$ and control device deflection $\sigma^2(\delta_{\text{CD}})$ were calculated for three experimental conditions: tracking with NoHA, tracking task with DHA, and tracking task with IHA.

Figure 6a depicts the mean values and 95% confidence intervals of $\sigma^2(F_{\text{pilot}})$ over all participants, together with the values for the variances $\sigma^2(F_{\text{hapt}})$ of the force provided by the haptic aids. The effect of haptic aid on $\sigma^2(F_{\text{pilot}})$ was found to be statistically significant [$F(2, 14) = 7.508$ and $p < 0.05$]. Post-hoc tests with Bonferroni correction revealed that the DHA condition was statistically significantly different from the other two conditions (Table 2). Pilots applied lower forces with DHA in order to achieve the control task. This was because DHA provided part of the force needed for the tracking task, making the task less tiring for participants. The variance $\sigma^2(F_{\text{hapt}})$ of the force provided by DHA was approximately twice the variance of the force applied by participants (see Fig. 6a). This indicates a large contribution of the DHA to the tracking task. On the other hand, conditions IHA and NoHA were not significantly different (Table 2).

The variance of control device deflection $\sigma^2(\delta_{\text{CD}})$ was clearly reduced with the IHA (Fig. 6b). The ANOVA test confirmed that the effect of the haptic aid on $\sigma^2(\delta_{\text{CD}})$ was statistically significant ($F(2, 14) = 12.300$, $p < 0.05$). Post-hoc tests using Bonferroni correction showed that the differences between IHA and the other two cases were statistically significant (Table 2). Participants slightly moved the stick from the center position in the IHA condition. This behavior, combined with the large shift of the neutral point shown in Fig. 6b, allowed participants to keep the tracking error close to zero.

Pilot performance was evaluated by comparing the variance of the tracking error $\sigma^2(e)$ between the three tracking conditions. Both the DHA and IHA led to a lower variance compared with the NoHA condition (Fig. 6c). The ANOVA test showed that the effect of the haptic aid on $\sigma^2(e)$ was statistically significant ($F(1.2, 8.4) = 62.671$, $p < 0.05$). Post-hoc tests using the Bonferroni correction revealed that the differences between all the conditions were statistically significant (Table 2). Thus, both the DHA and IHA helped participants in increasing performance. Although performance differed only slightly between DHA and NoHA, the variance in the IHA condition was approximately 80% lower than the other two conditions. Figure 6c also shows the performance of DHA and IHA with an infinitely compliant and an infinitely stiff human, respectively. As explained in Sec. IV.E, the difference between the two values is due to the influence of the force disturbance F_{dist}. Nonetheless, it can be noted that in both DHA and IHA conditions, participants improved the performance that they would have obtained by assuming a passive behavior (i.e., infinitely compliant or infinitely stiff). This shows that a pilot who contributes actively to controlling the aircraft may achieve better performance with respect to the passive behavior described in the two extreme conditions.

B. Admittance

Figure 7 shows the admittance estimated with the three identification methods in conditions NoHA, DHA, and IHA, averaged over all participants. High VAF and coherence values $\hat{\Gamma}^2_{\text{adm}}$ were found for the ARX and the CSD-based estimates, respectively (see Fig. 8). However, in the NoHA and DHA conditions, the CSD-based method produced estimates that differed largely from those obtained with ARX and CSD-ML methods at frequencies below 1 Hz. On the contrary, the admittance values estimated by the ARX and CSD-ML methods were similar. Only in the IHA case, the three methods gave similar results.

As shown in previous papers [20,28], these differences could be due to a bias that characterizes the CSD-based estimates when the so-called noninterference hypothesis is not fulfilled, i.e., when the power content of the visual error e is not negligible at frequencies $\{f_d\}$ where the disturbance force F_{dist} has power.

To verify if the noninterference hypothesis was fulfilled during our tracking conditions, the power content of e at frequencies $\{f_d\}$ (where the disturbance force F_{dist} has power), $\{f_t\}$ (where the target trajectory θ_{tar} has power), and $\{f_N\}$ (where both forcing functions have no power) is shown in Fig. 9. The power content of e at frequencies $\{f_d\}$ is clearly not negligible for NoHA and DHA

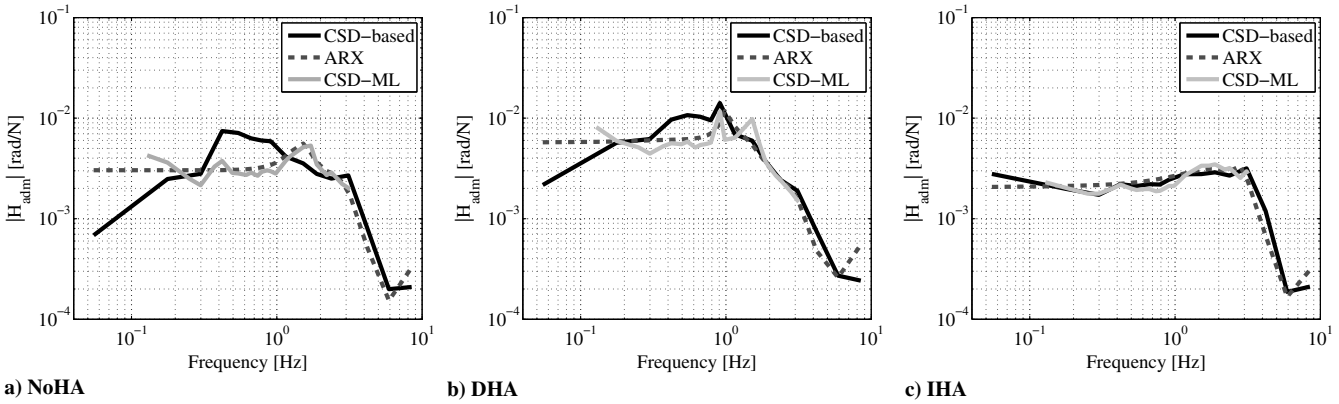

Fig. 7 Admittance estimates for NoHA, DHA, and IHA conditions, averaged over all participants.

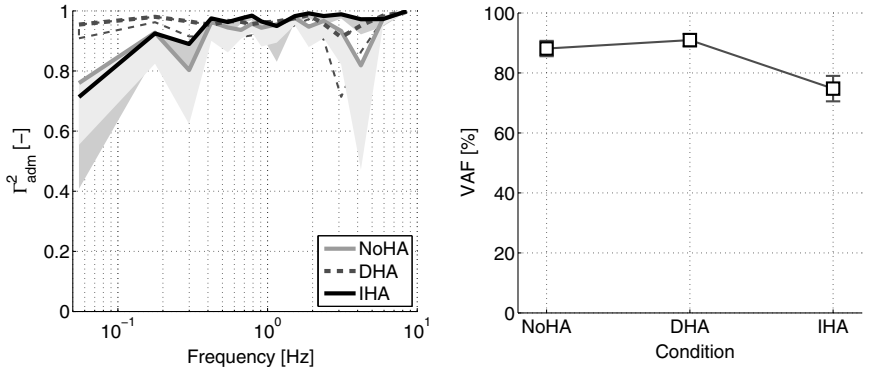

a) $\hat{\Gamma}^2_{adm}$ for CSD-based method **b) VAF for ARX method**

Fig. 8 Means and standard deviations of reliability measures for neuromuscular estimates, over all participants.

conditions (14% and 22% of the total power, respectively), whereas it is lower in the IHA case (7%). This explains the bias at low frequencies in the CSD-based estimates for the NoHA and DHA cases.

To better highlight differences between NoHA, DHA, and IHA, the admittance values estimated in the three conditions are shown together in Fig. 10 (dashed lines). Only estimates from the ARX method are provided, because they are similar but smoother than those obtained with the CSD-ML method. The admittance values given by the CSD-based method are not considered as these estimates clearly contain a bias. In addition, average admittance values estimated during the "classical tasks" are provided as a reference (continuous lines). Admittance varied mostly at frequencies below 1 Hz. Higher admittance values were found in the DHA condition with respect to the NoHA condition. This indicates that participants were more compliant with the DHA to follow the control action suggested by the DHA force. On the other hand, admittance was lower during the IHA condition. Thus, participants adopted a stiffer setting of their arm, which allowed them to oppose the IHA force.

Note that participants varied their admittance over a larger range during the classical tasks (see Fig. 10). More precisely, the admittance during the PT (i.e., adopt maximum stiffness) was lower, whereas the admittance estimates during RT (i.e., relax the arm) and FT (i.e., adopt maximum compliance) were higher. Thus, participants did not adopt maximum compliance during the DHA condition, or maximum stiffness during the IHA condition. We hypothesize that participants would be able to reach maximum and minimum admittances only if they rely solely on forces provided by the haptic aids, without trying to actively minimize the tracking error.

At frequencies above 1 Hz, the admittance of all tracking conditions and classical tasks converged to similar values. The shape of admittance magnitude had a slope of approximately $100\ [(\mathrm{rad/N})/\mathrm{dec}] = 40\ (\mathrm{dB/dec})$, which corresponds to the slope of the dynamics of a mass subjected to forces. This indicates that at high frequencies the admittance was mainly determined by inertial properties of the arm. The peak in the admittance of PT at frequencies around 4 Hz is consistent with previous results [24].

C. Pilot Visual Response

The visual response H_{vis} describes how participants generate a force F_{pilot} on the control device based on the error e presented on the display. Note that in the literature, the visual response often refers to the transfer function between the visual error and the stick control deflection σ_{CD} [18]. As explained in Sec. III, we adopted a different definition of H_{vis} not to include the haptic system in the visual response. Only ARX and CSD-ML methods can estimate H_{vis} directly. Results of the two methods are shown in Fig. 11, averaged over all participants.

Despite the fact that ARX method provided smoother estimates, both methods gave consistent results. The general shape of the visual response estimates was very similar for NoHA and DHA conditions. The estimates resembled a gain at low frequencies and a differentiator at higher frequencies; i.e., the participants generated leads. The only relevant difference between NoHA and DHA was that the magnitude of the visual response was lower at all frequencies for the DHA case. This indicates that participants applied lower forces on the control device in response to the visual tracking error. The IHA response was similar to the DHA response at higher frequencies but resembled a gain at frequencies below 0.7 Hz. Participants started to generate leads at higher frequencies than in the NoHA and DHA conditions.

D. Control and Open-Loop Transfer Functions

The control transfer function H_{control} represents the transfer function from the visual error e to the deflection of the control device δ_{CD}. In a compensatory tracking task without haptic aids, H_{control}

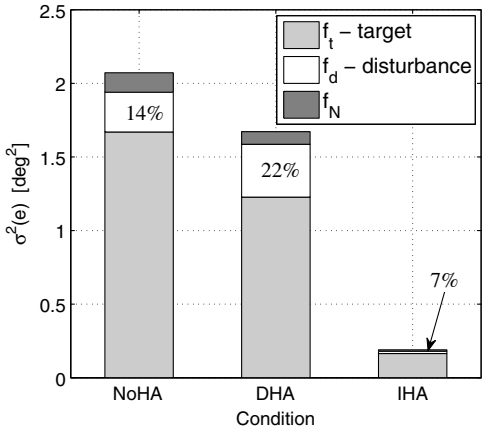

Fig. 9 Decomposition of the variance of the visual error and percentages at frequencies $\{f_d\}$.

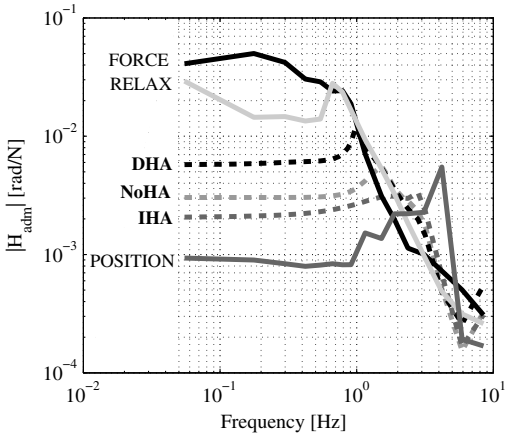

Fig. 10 Admittances for classical and tracking tasks obtained with CSD-based and ARX methods, respectively.

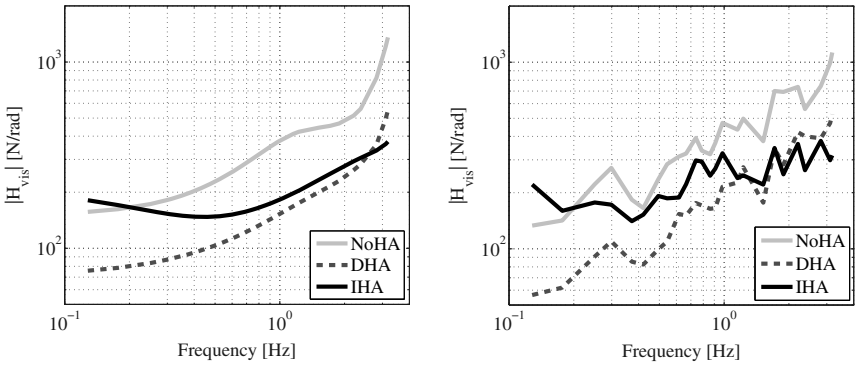

a) ARX **b) CSD-ML**

Fig. 11 Pilot visual responses estimated with ARX and CSD-ML methods, averaged over all participants.

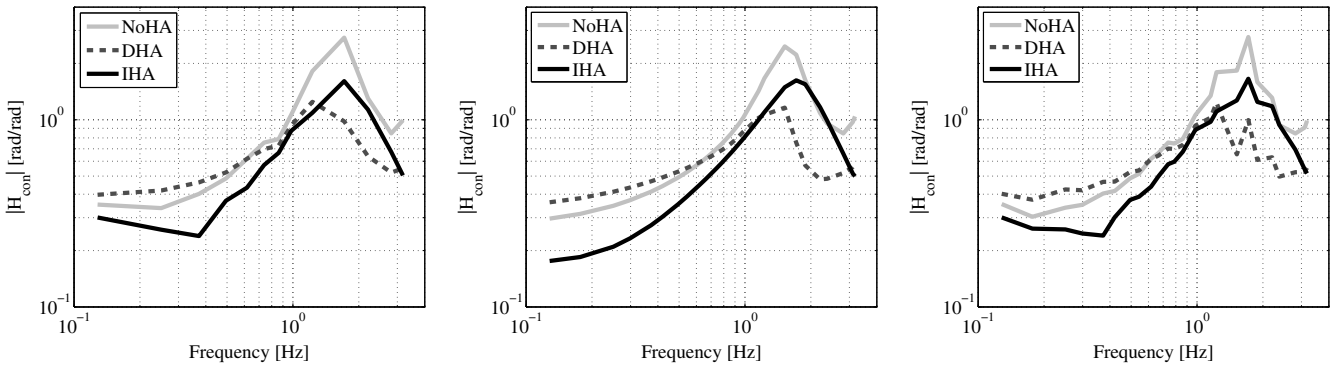

a) CSD-based **b) ARX** **c) CSD-ML**

Fig. 12 Responses H_{control} estimated with the three identification methods, averaged over all participants.

includes the pilot visual response VIS, the admittance ADM, and the control device CD. However, in the control task shown in Fig. 3, H_{control} also accounts for the dynamics of the haptic aid (H_{DHA} or H_{IHA}). Figure 12 depicts the estimated control transfer functions for experimental conditions NoHA, DHA, and IHA with all identification methods (CSD-based, CSD-ML, and ARX). For all conditions, the coherence $\Gamma^2_{\text{control}}$ associated to the CSD-based method was higher than 0.95. The estimates of $\hat{H}_{\text{control}}$ were similar for the three identification methods. The magnitude of $\hat{H}_{\text{control}}$ changed slightly between the conditions NoHA, DHA, and IHA, but the general shape was similar. The estimates resembled a gain at low frequencies and a differentiator at medium frequencies, as would be expected from the dynamics of the controlled element [18]. The peak at high frequency is due to the combined dynamics of the control device and the neuromuscular system [18]. The effect of DHA and IHA is to decrease the magnitude of this peak, which results in improved closed-loop stability and better performance [19].

The open-loop transfer function H_{OL} represents the transfer function from the visual error e to the position of the controlled element θ_{CE}. In the control task shown in Fig. 3, it includes the control response H_{control}, the dynamics of the neutral point shift (only for IHA), and the controlled element CE. Figure 13 shows the estimates of H_{OL} given by the CSD-based, CSD-ML, and ARX methods. High coherence values Γ^2_{OL} were found for the CSD-based estimates ($\Gamma^2_{\text{OL}} > 0.95$ at all frequencies). The three identification methods gave similar estimates. At frequencies below 1 Hz, the open-loop transfer functions resemble integrator-like dynamics for all NoHA, DHA, and IHA conditions. These findings correlate favorably with McRuer's theories [18], which assess that pilots adapt their responses to yield a combined pilot–aircraft dynamics similar to a single integrator. Although these theories were developed for tracking tasks *without* haptic aids, our results lend support to their validity also when haptic aids are used. The crossover frequency ω_c was about 0.3 Hz for NoHA and DHA cases, whereas it significantly increased to about

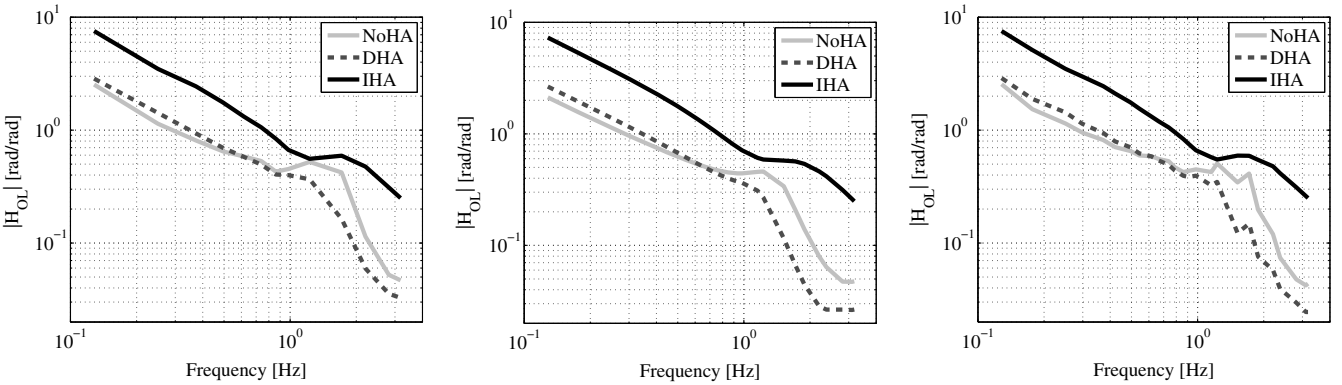

a) CSD-based **b) ARX** **c) CSD-ML**

Fig. 13 Open-loop responses estimated with the three identification methods, averaged over all participants.

0.8 Hz with IHA (Fig. 13). A larger crossover frequency indicates that the system has a faster dynamic response and an improved ability to track the signal. This is in complete agreement with high performance found for IHA tracking condition (see Fig. 9).

VI. Conclusions

In this paper, two different approaches for haptic aids design, the direct haptic aid (DHA) and indirect haptic aid (IHA), were evaluated in a tracking task and compared with a baseline condition without haptic support. The haptic aids were designed based on their effect on human behavior. Both approaches allowed participants to increase performance in tracking a target signal. In particular, the IHA outperformed the DHA and the baseline condition. On the other hand, the physical effort was significantly reduced by the DHA. This was shown by a decreased variance of the force that participants applied on the control device to perform the task.

Pilot control behavior was estimated with three identification methods: the commonly used cross-spectral density (CSD)–based method and the two novel autoregressive models with exogenous inputs (ARX method) and CSD for a multiloop tracking task (CSD-ML) method. The ARX and the CSD-ML methods gave similar estimates, whereas the admittance estimated by the CSD-based method contained a bias caused by noncompliance to the so-called noninterference hypothesis [20,28].

The identified pilot responses indicated that participants adapted their admittance to fully exploit the haptic aids. Participants adopted a lower admittance (stiffer neuromuscular dynamics) to oppose the IHA force, whereas they adopted a higher admittance (more compliant neuromuscular dynamics) to better follow the control action suggested by the DHA force. Furthermore, participants adapted their visual response to yield an open-loop transfer function similar to a single integrator in all the tracking conditions, with and without haptic aids. This finding suggests that McRuer's theories are still applicable when haptic aids are used, although this needs to be confirmed with different control dynamics from those used in this study.

These results shed light on human adaptation to different designs of haptic aids. However, the current study has considered only nonpilot participants. It remains to be further investigated how real pilots would interact with DHA and IHA aids.

Acknowledgments

The work in this paper was partially supported by the myCopter project, funded by the European Commission under the 7th Framework Program. This work was also partially supported by the Brain Korea 21 PLUS Program through the National Research Foundation of Korea funded by the Ministry of Education. Correspondence should be directed to Heinrich H. Bülthoff.

References

[1] Wickens, C. D., Mavor, A. S., Parasuraman, R., and McGee, J. P., *The Future of Air Traffic Control: Human Operators and Automation*, The National Academies Press, Washington, D.C., 1998, pp. 1–336.

[2] Billings, C. E., *Aviation Automation: The Search for a Human-Centered Approach*, Lawrence Erlbaum Associates Publishers, Mahwah, NJ, 1997, pp. 1–355.

[3] Endsley, M. R., "Toward a Theory of Situation Awareness in Dynamic Systems," *Human Factors: The Journal of the Human Factors and Ergonomics Society*, Vol. 37, No. 1, March 1995, pp. 32–64. doi:10.1518/001872095779049543

[4] Wickens, C. D., "Situation Awareness: Review of Mica Endsley's 1995 Articles on Situation Awareness Theory and Measurement," *Human Factors: The Journal of the Human Factors and Ergonomics Society*, Vol. 50, No. 3, June 2008, pp. 397–403. doi:10.1518/001872008X288420

[5] Norman, D. A., "The Problem of Automation: Inappropriate Feedback and Interaction, Not Over-Automation," *Philosophical Transactions of the Royal Society B: Biological Sciences*, Vol. 327, No. 1241, April 1990, pp. 585–593. doi:10.1098/rstb.1990.0101

[6] Abbink, D., Mulder, M., and Boer, E. R., "Haptic Shared Control: Smoothly Shifting Control Authority?" *Cognition, Technology and Work*, Vol. 14, No. 1, Nov. 2012, pp. 19–28. doi:10.1007/s10111-011-0192-5

[7] Mulder, M., Mulder, M., van Paassen, M. M., and Abbink, D. A., "Haptic Gas Pedal Feedback," *Ergonomics*, Vol. 51, No. 11, Oct. 2008, pp. 1710–1720. doi:10.1080/00140130802331583

[8] Abbink, D. A., and Mulder, M., "Exploring the Dimensions of Haptic Feedback Support in Manual Control," *Journal of Computing and Information Science in Engineering*, Vol. 9, No. 1, March 2009, pp. 011006-1–011006-9. doi:10.1115/1.3072902

[9] Abbink, D. A., Boer, E. R., and Mulder, M., "Motivation for Continuous Haptic Gas Pedal Feedback to Support Car Following," *2008 IEEE Intelligent Vehicles Symposium*, Inst. of Electrical and Electronics Engineers, Piscataway, NJ, June 2008, pp. 283–290. doi:10.1109/IVS.2008.4621325

[10] Lam, T. M., Mulder, M., and Van Paassen, M. M., "Haptic Interface for UAV Collision Avoidance," *The International Journal of Aviation Psychology*, Vol. 17, No. 2, Dec. 2007, pp. 167–195. doi:10.1080/10508410701328649

[11] Alaimo, S. M. C., Pollini, L., Magazzù, A., Bresciani, J.-P., Robuffo Giordano, P., Innocenti, M., and Bülthoff, H. H., "Preliminary Evaluation of a Haptic Aiding Concept for Remotely Piloted Vehicles," *EuroHaptics '10 Proceedings of the 2010 International Conference on Haptics: Generating and Perceiving Tangible Sensations*, Springer–Verlag, Berlin, July 2010, pp. 418–425.

[12] Bedell, J., and Berta, W., "Skew and Loss Detection System for Adjacent High Lift Devices," U.S. Patent 5,680,124, filed 15 May 1995, Oct. 1997.

[13] Goodrich, K., Schutte, P., and Williams, R., "Haptic-Multimodal Flight Control System Update," *Proceedings of 11th AIAA Aviation Technology, Integration, and Operations (ATIO) Conference*, AIAA, Reston, VA, Sept. 2011, pp. 1–17; also AIAA Paper 2011-6984, 2011.

[14] Doehler, H.-U., Lüken, T., and Lantzsch, R., "ALLFlight: A Full Scale Enhanced and Synthetic Vision Sensor Suite for Helicopter Applications," SPIE Defense, Security, and Sensing, International Soc. for Optics and Photonics, Bellingham, WA, April 2009, pp. 1–11. doi:10.1117/12.818454

[15] Abildgaard, M., and von Grünhagen, W., "Demonstration of an Active Sidestick in the DLR Flying Helicopter Simulator (FHS)," *European Rotorcraft Forum (ERF)*, Royal Aeronautical Soc., London, Oct. 2008, pp. 1174–1185.

[16] Alaimo, S. M., Pollini, L., Bresciani, J.-P., and Bülthoff, H. H., "A Comparison of Direct and Indirect Haptic Aiding for Remotely Piloted Vehicles," *Proceedings of the 19th IEEE International Symposium on Robot and Human Interactive Communication*, Inst. of Electrical and Electronics Engineers, Piscataway, NJ, Sept. 2010, pp. 506–512. doi:10.1109/ROMAN.2010.5598647

[17] Alaimo, S. M. C., Pollini, L., Bresciani, J.-P., and Bülthoff, H. H., "Experiments of Direct and Indirect Haptic Aiding for Remotely Piloted Vehicles with a Mixed Wind Gust Rejection/Obstacle Avoidance Task," *Proceedings of the AIAA Modeling and Simulation Technologies Conference*, AIAA, Reston, VA, Aug. 2011, pp. 1–18; also AIAA Paper 2011-6242, 2011.

[18] McRuer, D. T., "Human Pilot Dynamics in Compensatory Systems: Theory, Models and Experiments with Controlled Element and Forcing Function Variations," Air Force Flight Dynamics Laboratory, AFFDL-TR-65-15, Wright–Patterson AFB, OH, July 1965.

[19] Pool, D. M., Mulder, M., Van Paassen, M. M., and Van der Vaart, J. C., "Effects of Peripheral Visual and Physical Motion Cues in Roll-Axis Tracking Tasks," *Journal of Guidance, Control, and Dynamics*, Vol. 31, No. 6, Nov. 2008, pp. 1608–1622. doi:10.2514/1.36334

[20] Olivari, M., Nieuwenhuizen, F. M., Venrooij, J., Bülthoff, H. H., and Pollini, L., "Multi-Loop Pilot Behaviour Identification in Response to Simultaneous Visual and Haptic Stimuli," *Proceedings of the AIAA Modeling and Simulation Technlogies Conference*, AIAA, Reston, VA, Aug. 2012, pp. 1–23; also AIAA Paper 2012-4795, 2012.

[21] Abbink, D. A., Mulder, M., Van der Helm, F. C. T., Mulder, M., and Boer, E. R., "Measuring Neuromuscular Control Dynamics During Car Following with Continuous Haptic Feedback," *IEEE Transactions on Systems, Man, and Cybernetics. Part B*, Vol. 41, No. 5, Oct. 2011, pp. 1239–1249. doi:10.1109/TSMCB.2011.2120606

[22] McRuer, D. T., and Jex, H. R., "A Review of Quasi-Linear Pilot Models," *IEEE Transactions on Human Factors in Electronics*, Vol. HFE-8, No. 3, Sept. 1967, pp. 231–249. doi:10.1109/THFE.1967.234304

[23] Mugge, W., Abbink, D. A., Schouten, A. C., DeWald, J. P. A., and Van der Helm, F. C. T., "A Rigorous Model of Reflex Function Indicates That Position and Force Feedback Are Flexibly Tuned to Position and Force Tasks," *Experimental Brain Research*, Vol. 200, No. 3, Aug. 2009, pp. 325–340. doi:10.1007/s00221-009-1985-0

[24] Schouten, A. C., de Vlugt, E., Van Hilten, B. J., and Van der Helm, F. C. T., "Quantifying Proprioceptive Reflexes During Position Control of the Human Arm," *IEEE Transactions on Biomedical Engineering*, Vol. 55, No. 1, Jan. 2008, pp. 311–321. doi:10.1109/TBME.2007.899298

[25] Van der Helm, F. C. T., Schouten, A. C., de Vlugt, E., and Brouwn, G. G., "Identification of Intrinsic and Reflexive Components of Human Arm Dynamics During Postural Control," *Journal of Neuroscience Methods*, Vol. 119, No. 1, May. 2002, pp. 1–14. doi:10.1016/S0165-0270(02)00147-4

[26] Damveld, H. J., Abbink, D. A., Mulder, M., Mulder, M., Van Paassen, M. M., Van der Helm, F. C. T., and Hosman, R. J. A. W., "Measuring the Contribution of the Neuromuscular System During a Pitch Control Task," *Proceedings of the AIAA Modeling and Simulation Technologies Conference*, AIAA, Reston, VA, Aug. 2009, pp. 1–19; also AIAA Paper 2009-5824, 2009.

[27] Damveld, H. J., Abbink, D. A., Mulder, M., Mulder, M., Van Paassen, M. M., Van der Helm, F. C. T., and Hosman, R. J. A. W., "Identification of the Feedback Component of the Neuromuscular System in a Pitch Control Task," *Proceedings of the AIAA Guidance, Navigation, and Control Conference*, AIAA, Reston, VA, Aug. 2010, pp. 1–22; also AIAA Paper 2010-7915, 2010.

[28] Olivari, M., Nieuwenhuizen, F. M., Venrooij, J., Bülthoff, H. H., and Pollini, L., "Methods for Multi-Loop Identification of Visual and Neuromuscular Pilot Responses," *IEEE Transactions on Cybernetics*, April 2013, pp. 1–12 (accepted for publication).

[29] Alaimo, S. M. C., Pollini, L., and Bülthoff, H. H., "Admittance-Based Bilateral Teleoperation with Time Delay for an Unmanned Aerial Vehicle Involved in an Obstacle Avoidance Task," *Proceedings of the AIAA Modeling and Simulation Technologies Conference*, AIAA, Reston, VA, Aug. 2011, pp. 1–19; also AIAA Paper 2011-6243, 2011.

[30] McRuer, D. T., and Krendel, E. S., "Mathematical Models of Human Pilot Behavior," AGARD AD-775-905, Paris, Jan. 1974.

[31] Profumo, L., Pollini, L., and Abbink, D. A., "Direct and Indirect Haptic Aiding for Curve Negotiation," *Proceedings of the IEEE International Conference on System, Man and Cybernetics*, Inst. of Electrical and Electronics Engineers, Piscataway, NJ, Oct. 2013, pp. 1846–1852. doi:10.1109/SMC.2013.318

[32] Alaimo, S. M. C., Pollini, L., Bresciani, J.-P., and Bülthoff, H. H., "Evaluation of Direct and Indirect Haptic Aiding in an Obstacle Avoidance Task for Tele-Operated Systems," *Proceedings of the 18th World Congress of the International Federation of Automatic Control*, International Federation of Automatic Control, Laxenburg, Austria, Sept. 2011, pp. 1–6.

[33] De Stigter, S., Mulder, M., and Van Paassen, M. M., "Design and Evaluation of Haptic Flight Director," *Journal of Guidance, Control, and Dynamics*, Vol. 30, No. 1, Jan. 2007, pp. 35–46. doi:10.2514/1.20593

[34] McRuer, D., and Weir, D. H., "Theory of Manual Vehicular Control," *IEEE Transactions on Man-Machine Systems*, Vol. 10, No. 4, Dec. 1969, pp. 257–291. doi:10.1109/TMMS.1969.299930

[35] Van Paassen, M. M., "Biophysics in Aircraft Control, A Model of the Neuromuscular System of the Pilot's Arm," Ph.D. Thesis, Faculty of Aerospace Engineering, Delft Univ. of Technology, Delft, The Netherlands, June 1994.

[36] Venrooij, J., Abbink, D. A., Mulder, M., and Van Paassen, M. M., "A Method to Measure the Relationship Between Biodynamic Feedthrough and Neuromuscular Admittance," *IEEE Transactions on Systems, Man, and Cybernetics — Part B*, Vol. 41, No. 4, Aug. 2011, pp. 1158–1169. doi:10.1109/TSMCB.2011.2112347

[37] Van Lunteren, A., "Identification of Human Operator Describing Function Models with One or Two Inputs in Closed Loop Systems," Ph.D. Thesis, Faculty of Aerospace Engineering, Delft Univ. of Technology, Delft, The Netherlands, Jan. 1979.

[38] Ljung, L., *System Identification: Theory for the User*, 2nd ed., Prentice–Hall, Englewood Cliffs, NJ, 1999, pp. 1–672.

[39] Schouten, A. C., de Vlugt, E., and Van der Helm, F. C. T., "Design of Perturbation Signals for the Estimation of Proprioceptive Reflexes," *IEEE Transactions on Biomedical Engineering*, Vol. 55, No. 5, May 2008, pp. 1612–1619. doi:10.1109/TBME.2007.912432

[40] Bendat, J., and Piersol, A., *Random Data: Analysis and Measurement Procedures*, Wiley Series in Probability and Statistics, Wiley, Hoboken, NJ, 2010, pp. 1–640.

[41] Nieuwenhuizen, F. M., Zaal, P. M. T., Mulder, M., Van Paassen, M. M., and Mulder, J. A., "Modeling Human Multichannel Perception and Control Using Linear Time-Invariant Models," *Journal of Guidance, Control, and Dynamics*, Vol. 31, No. 4, July–Aug. 2008, pp. 999–1013. doi:10.2514/1.32307

[42] Hess, R. A., "Modeling the Effects of Display Quality upon Human Pilot Dynamics and Perceived Vehicle Handling Qualities," *IEEE Transactions on Systems, Man, and Cybernetics*, Vol. 25, No. 2, Feb. 1995, pp. 338–344. doi:10.1109/21.364831

[43] Damveld, H. J., Beerens, G. C., Van Paassen, M. M., and Mulder, M. M., "Design of Forcing Functions for the Identification of Human Control Behavior," *Journal of Guidance, Control, and Dynamics*, Vol. 33, No. 4, July–Aug. 2010, pp. 1064–1081. doi:10.2514/1.47730

[44] Mugge, W., Abbink, D. A., and Van der Helm, F. C. T., "Reduced Power Method: How to Evoke Low-Bandwidth Behaviour While Estimating Full-Bandwidth Dynamics," *Proceedings of the 2007 IEEE 10th International Conference on Rehabilitation Robotics*, Inst. of Electrical and Electronics Engineers, Piscataway, NJ, June 2007, pp. 575–581. doi:10.1109/ICORR.2007.4428483

[45] Zaal, P. M. T., Pool, D. M., de Bruin, J., Mulder, M., and Van Paassen, M. M., "Use of Pitch and Heave Motion Cues in a Pitch Control Task," *Journal of Guidance, Control, and Dynamics*, Vol. 32, No. 2, March–April 2009, pp. 366–377. doi:10.2514/1.39953

[46] Pintelon, R., and Schoukens, J., *System Identification: A Frequency Domain Approach*, 2nd ed., Wiley–IEEE Press, Hoboken, NJ, 2012, pp. 1–788.

[47] Abbink, D. A., and Mulder, M., "Neuromuscular Analysis as a Guideline in Designing Shared Control," *Advances in Haptics*, InTech, Rijeka, Croatia, April 2010, pp. 501–512.

[48] Dénes, J., and Keedwell, A. D., *Latin Squares, Vol. 46 of Annals of Discrete Mathematics*, North-Holland Publishing Co., Amsterdam, 1991, pp. 1–453.

[49] Field, A., *Discovering Statistics Using SPSS*, Introducing Statistical Methods Series, SAGE, London, 2007, pp. 1–856.

[50] Jenkins, G. M., and Watts, D. G., *Spectral Analysis and its Applications*, Holden–Day, San Francisco, 1969, pp. 1–525.

3. Identifying time-varying neuromuscular system dynamics

This study was published and presented at the IEEE conference on Systems, Man and Cybernetics:

M. Olivari, F.M. Nieuwenhuizen, H. H. Bülthoff and L. Pollini, (2014) **Identifying Time-Varying Neuromuscular System with a Recursive Least-Squares Algorithm: a Monte-Carlo Simulation Study** *Proceedings of the IEEE International Conference on Systems, Man and Cybernetics, San Diego (CA)*, 5-8 Oct. 2014.

Abstract

A human-centered design of haptic aids aims at tuning the force feedback based on the effect it has on human behavior. For this goal, a better understanding of the influence of haptic aids on the pilot neuromuscular response becomes crucial. In realistic scenarios, the neuromuscular response can continuously vary depending on many factors, such as environmental factors or pilot fatigue. This paper presents a method that online estimates time-varying neuromuscular dynamics during force-related tasks. This method is based on a Recursive Least Squares (RLS) algorithm and assumes that the neuromuscular response can be approximated by a Finite Impulse Response filter. The reliability and the robustness of the method were investigated by performing a set of Monte-Carlo simulations with increasing level or remnant noise. Even with high level of remnant noise, the RLS algorithm provided accurate estimates when the neuromuscular dynamics were constant or changed slowly. With instantaneous changes, the RLS algorithm needed almost 8s to converge to a reliable estimate. These results seem to indicate that RLS algorithm is a valid tool for estimating online time-varying admittance.

Identifying Time-Varying Neuromuscular System with a Recursive Least-Squares Algorithm: a Monte-Carlo Simulation Study

Mario Olivari*†, Frank M. Nieuwenhuizen*, Heinrich H. Bülthoff*‡, Lorenzo Pollini†
*Department of Human Perception, Cognition, and Action
Max Planck Institute for Biological Cybernetics, Tübingen 72012, Germany
†Dipartimento di Ingegneria dell'Informazione, Faculty of Automation Engineering
University of Pisa, Italy
‡Department of Brain and Cognitive Engineering
Korea University, Seoul, South Korea
Email: {mario.olivari; frank.nieuwenhuizen; heinrich.buelthoff}@tuebingen.mpg.de; lpollini@dsea.unipi.it

***Abstract*—A human-centered design of haptic aids aims at tuning the force feedback based on the effect it has on human behavior. For this goal, a better understanding of the influence of haptic aids on the pilot neuromuscular response becomes crucial. In realistic scenarios, the neuromuscular response can continuously vary depending on many factors, such as environmental factors or pilot fatigue. This paper presents a method that online estimates time-varying neuromuscular dynamics during force-related tasks. This method is based on a Recursive Least Squares (RLS) algorithm and assumes that the neuromuscular response can be approximated by a Finite Impulse Response filter. The reliability and the robustness of the method were investigated by performing a set of Monte-Carlo simulations with increasing level or remnant noise. Even with high level of remnant noise, the RLS algorithm provided accurate estimates when the neuromuscular dynamics were constant or changed slowly. With instantaneous changes, the RLS algorithm needed almost 8s to converge to a reliable estimate. These results seem to indicate that RLS algorithm is a valid tool for estimating online time-varying admittance.**

I. Introduction

Haptic aids aim at helping pilots during a control task by providing force feedback on the control device [1]. To assess whether haptic forces have a positive effect on the pilot performing the task, an insight is required into the control behavior of the pilot. The dynamics of the neuromuscular system play an important role when trying to investigate the effect of haptic aids on pilot behavior [2]. Previous works have investigated methods to estimate the neuromuscular system during force-related tasks [3] or more complex control tasks [2], [4], [5]. However, a key limitation with much of the literature is that the estimation methods assume a time-invariant neuromuscular response. In realistic control scenarios, the neuromuscular response is likely to be time-variant, since pilots change their behavior depending on environmental variables, fatigue, etc. [6]. Thus, there is a need for identification methods that can be used to assess the time-varying nature of the neuromuscular response.

Ensemble methods have been applied to estimate time-varying neuromuscular system [7]–[9]. These methods use a series (ensemble) of input-output measurements to obtain a least-square estimate of the system impulse response. Application to experimental data showed that ensemble methods provide reliable neuromuscular estimates [7]. However, these methods require the same time-varying behavior for each realization in the ensemble [7]. This is not suitable for a generic control task, in which pilots are likely to change their behavior depending on environmental variables.

Recently, a method based on the Morlet wavelet transformation was used to estimate time-varying neuromuscular response [6], [10]. This technique was able to identify a simulated time-varying neuromuscular response without requiring several repetitions of the same time-varying behavior. However, the method was performed offline, i.e., it provided the estimate of time-varying neuromuscular response only after having collected all the measured data. Online estimation becomes important in control tasks with haptic aids, since it offers a means to continuously assess how pilots interact with the haptic forces.

The aim of this paper is to present a proof of concept and simulation evaluation of an *online* estimation technique to be used for neuromuscular response estimation. The technique uses a Recursive Least Squares (RLS) method that provides an estimate of time-varying neuromuscular dynamics during force-related tasks. The reliability and the robustness of the method is analyzed by using a set of Monte-Carlo simulations. Our ultimate goal is to apply the developed algorithm to experimental data.

The paper is organized as follows. Section II provides an overview of the interactions between the neuromuscular system and the control device. Section III gives a brief overview of the RLS algorithm, and Section IV presents how the RLS algorithm was used for estimating a time-varying neuromuscular response. In Section V results of Monte-Carlo simulations are presented to assess the algorithm and identification approach. Our conclusions are drawn in the final section.

II. Control Task

Humans interact with a generic Control Device, e.g., a control stick or a steering wheel, by moving their arm. In

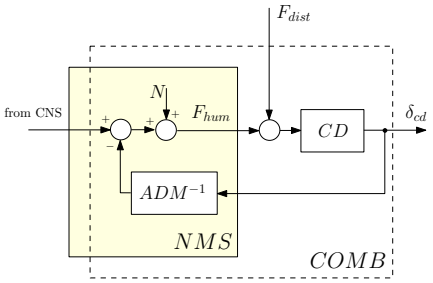

Fig. 1. Interaction of a pilot with the control device. The combined block of the admittance and the control device (COMB) and the signal F_{dist} are needed for the identification algorithm detailed in Section IV.

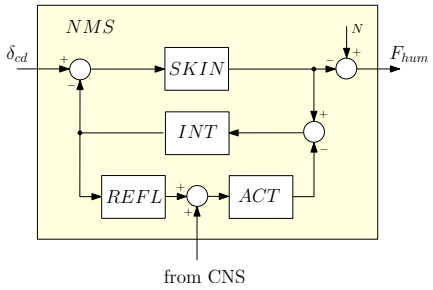

Fig. 2. Main components of the neuromuscular system of the human arm.

TABLE I. ELEMENTS OF NEUROMUSCULAR SYSTEM

Block	Transfer Function	Physical Meaning
INT	$H_{int}(s) = \frac{1}{m_{int}s^2 + b_{int}s + k_{int}}$	Intrinsic muscle dynamics
$SKIN$	$H_{skin}(s) = b_{skin}s + k_{skin}$	Skin dynamics
$REFL$	$H_{refl}(s) = (k_a s + k_v s + k_p)e^{-\tau s}$	Reflexive dynamics
ACT	$H_{act}(s) = \frac{1}{\frac{1}{\omega_0^2}s^2 + \frac{2\beta}{\omega_0}s + k_i}$	Activation dynamics

general, the movement of the arm has several degrees of freedom. However, it can be simplified when considering the manipulation of a control stick [5]. Firstly, we consider a control stick that possesses one degree of freedom (lateral axis). Secondly, an arm rest is employed to keep the elbow at a fixed position. In this situation, humans tend to move the control device by immobilizing the wrist and by rotating the lower arm (hand and ulna) around the upper arm (humerus) [5]. Thus, the movement of the arm can be expressed as a rotation of the lower arm around the upper arm, which corresponds to a one-degree of freedom joint.

Fig. 1 shows a model for the interaction of a human arm with a control stick in the one-degree of freedom situation. The pilot generates a force F_{hum} to control the lateral deflection δ_{cd} of the Control Device (CD). At the same time, proprioceptive sensors of the neuromuscular system of the arm (NMS) sense the deflection δ_{cd} and its velocity (feedback path in Fig. 1) [3].The dynamics of neuromuscular system are described by the admittance ADM, which is defined as the causal relationship between the force acting on the arm and the position of the arm. All the elements of Fig. 1 are assumed to be linear, and the signal N (*Remnant*) accounts for all the unmodeled nonlinearities. The notation *from CNS* represents all cognitive actions that are communicated from the Central Nervous System, e.g., the pilot response to external visual cues.

The main components of the one-degree of freedom neuromuscular system are shown in Fig. 2 [3]. The block SKIN represents the visco-elasticity of the arm contact with the control device, generated by the skin of the hand. The block INT describes the intrinsic arm dynamics, which include the lumped mass of hand, lower arm, and upper arm, together with the contractile and elastic components of antagonistic muscles. The contractile components are activated by the efferent neurons ACT. The muscle spindle sensory system is represented by the reflexive dynamics REFL. Table I gives an overview of the dynamics of each block. The dynamics of the whole neuromuscular system are determined by the settings of these components. Humans are able to adapt the neuromuscular dynamics to the task they perform [2]–[4]. In realistic control situations, e.g., during postural control or driving tasks, humans vary their admittance continuously depending on the external environment [6].

III. RECURSIVE LEAST-SQUARES ALGORITHM

This section presents a method that can be applied to estimate dynamics of a time-varying neuromuscular system. The method uses a Recursive Least Square algorithm to estimate the impulse response of a system by approximating the response with a discrete-time Finite Impulse Response (FIR).

A. Impulse Response

A linear discrete time-varying system is completely described by its impulse response. The impulse response $h(n \cdot T, m \cdot T)$ represents the output of the system at time instant $n \cdot T$ when presented with an impulse signal δ at time instant $m \cdot T$, where T represents the sample time [7]. To simplify the notation, in the rest of the paper, the sample time is omitted when describing time instants. The response of the system $y(n)$ to a generic signal $u(n)$ is given by the discrete convolution of the impulse response $h(n, m)$ and the input itself $u(n)$ [7]:

$$y(n) = T \sum_{m=-\infty}^{\infty} h(n, m)u(m) \tag{1}$$

Eq. (1) can be further simplified if $h(n, m)$ describes a physical system. The impulse response of a physical system is causal, i.e. $h(n, m) = 0$ for $n < m$. Furthermore, the impulse response of many physical systems (e.g., the neuromuscular impulse response) becomes approximately zero after an initial transient, i.e., $h(n, m) = 0$ for $n > m + N_{imp}$ where N_{imp} represents the system memory. For such systems, eq. (1) becomes:

$$\begin{aligned} y(n) &= T \sum_{m=n-N_{imp}}^{n} h(n, m)u(m) \\ &= T \left[h(n, N_{imp}) \ \ldots \ h(n, n) \right] \begin{bmatrix} u(n - N_{imp}) \\ \ldots \\ u(n) \end{bmatrix} \\ &= T \, \mathbf{h}^T(n) \, \mathbf{u}(n) \end{aligned} \tag{2}$$

In time-varying systems, the vector $\mathbf{h}(n)$ assumes different values at each time step. However, if the system appears as time-invariant for large periods of time and only varies its dynamics seldomly, the vector $\mathbf{h}(n)$ remains constant for large periods. Thus, if the dynamics of the system change from a time-invariant condition $\mathbf{h}_1$ to a different time-invariant condition $\mathbf{h}_2$, the following holds:

$$y(n) = T \begin{cases} \mathbf{h}_1^T \mathbf{u}(n), & n \leq n_{last} \\ \mathbf{h}(n) \mathbf{u}(n), & n_{last} < n < n_{first} + N_{imp} \\ \mathbf{h}_2^T \mathbf{u}(n), & n \geq n_{first} + N_{imp} \end{cases} \tag{3}$$

where N_{imp} represents the system memory for both conditions, and n_{last} and n_{first} represent the last time sample where $\mathbf{h}(n) = \mathbf{h}_1$ and the first time sample where $\mathbf{h}(n) = \mathbf{h}_2$, respectively.

The change of the impulse response from $\mathbf{h}_1$ to $\mathbf{h}_2$ can be estimated based on input and output measurements. To achieve this, a Recursive Least-Squares algorithm can be applied.

B. Algorithm

A Recursive Least-Squares algorithm (RLS) can be used to estimate the coefficients of the impulse response $\mathbf{h}(n)$ such that the scalar product between the estimate $\tilde{\mathbf{h}}(n)$ and the measured input $\mathbf{u}(n)$ best matches the measured output $y(n)$ in a least square sense [11]. In a time-invariant system the impulse response $\mathbf{h}(n)$ does not vary with the time, i.e., $\mathbf{h}(n) = \mathbf{h}_1$. In this case, the estimate can be found as the optimal solution that minimizes the cost function V:

$$V(\mathbf{h}, n) = \sum_{i=0}^{n} \epsilon^2(i), \qquad \epsilon(i) = y(i) - \mathbf{h}^T \mathbf{u}(i) \tag{4}$$

$$\tilde{\mathbf{h}}(n) = \min_{\mathbf{h}} V(\mathbf{h}, n) \tag{5}$$

and the solution is given by:

$$\tilde{\mathbf{h}}(n) = \left[\sum_{i=0}^{n} \mathbf{u}(i) \mathbf{u}^T(i) \right]^{-1} \sum_{i=0}^{n} \mathbf{u}(i) y(i) \tag{6}$$

The cost function V in eq. (4) gives the same weight to all the sample errors $\epsilon(i)$. If the system $\mathbf{h}(n)$ changes its dynamics to a different value $\mathbf{h}_2$, the estimator in eq. (6) can not provide reliable estimates, since V is influenced more by the sum of the past errors than by the current error. To overcome this issue, a forgetting factor λ is included that gives a smaller weight to the errors occurred further in the past ($0 \ll \lambda < 1$) [11]. The cost function then becomes:

$$V(\mathbf{h}, n) = \sum_{i=0}^{n} \lambda^{n-i} \epsilon^2(i) \tag{7}$$

The resulting expression for the optimal value $\tilde{\mathbf{h}}(n)$ is:

$$\begin{aligned} \tilde{\mathbf{h}}(n) &= \left[\sum_{i=0}^{n} \lambda^{n-i} \mathbf{u}(i) \mathbf{u}^T(i) \right]^{-1} \sum_{i=0}^{n} \lambda^{n-i} \mathbf{u}(i) y(i) \\ &= \mathbf{R}_D^{-1}(n) \mathbf{p}(n) \end{aligned} \tag{8}$$

where the matrix $\mathbf{R}_D(n)$ is assumed to be nonsingular. This assumption is satisfied only if the excitation signal $u(n)$ is persistently exciting.

TABLE II. RLS ALGORITHM

INITIALIZE	$\mathbf{S}_D(-1) = \delta \mathbf{I}$, δ can be the inverse of the input signal power $\mathbf{p}_D(-1) = [0 \dots 0]$
FOR $n \geq 0$ **DO**	$\mathbf{S}_D(n) = \frac{1}{\lambda} \left[\mathbf{S}_D(n-1) - \frac{\mathbf{S}_D(n-1)\mathbf{u}(n)\mathbf{u}^T(n)\mathbf{S}_D(n-1)}{\lambda + \mathbf{u}^T(n)\mathbf{S}_D(n-1)\mathbf{u}(n)} \right]$ $\mathbf{p}_D(n) = \lambda \mathbf{p}_D(n-1) + y(n)\mathbf{u}(n)$

The algorithm, written as in eq. (8), requires the computation of the inverse of $\mathbf{R}_D(n)$ at each time step. However, this computation can be avoided by using the matrix inversion lemma [11], which allows for calculating the inverse of the matrix $\mathbf{R}_D(n)$ from the value calculated at the previous time step $\mathbf{R}_D(n-1)$. Table II shows the resulting RLS algorithm ($\mathbf{S}_D(n) = \mathbf{R}_D^{-1}(n)$).

IV. APPLICATION OF A RLS ALGORITHM FOR ESTIMATING ADMITTANCE

In this paper, the RLS algorithm is applied to estimate the time-varying dynamics of the neuromuscular system during force-related control tasks, the so-called *classical tasks* [12]. In these tasks, humans are asked either to resist (Position Task, PT) or to be compliant (Force Task, FT) with an external disturbance F_{dist} applied on the control device, see Fig. 1. To achieve best performance in PT and FT, humans need to assume minimum and maximum admittance, respectively [12]. Thus, switching between the two different classical tasks induces humans to vary their admittance between extreme values. Note that the contribution of the central nervous system can be assumed negligible in these tasks (*from CNS* $= 0$, see Fig. 1), since the cognitive action of the human is known to be limited [12].

As a first step, the RLS algorithm is applied to estimate the dynamics from the external force F_{dist} to the control device deflection δ_{cd} (dynamics of COMB in Fig. 1):

$$\tilde{\mathbf{h}}_{comb}(n) = \text{RLS}\left(\{F_{dist}(i), \delta(i)\}_{i=0,\dots,n} \right) \tag{9}$$

Note that the RLS algorithm approximates the impulse response of COMB with a Finite Impulse Response $\tilde{\mathbf{h}}_{comb}(n)$.

The Fourier Transform of $\tilde{\mathbf{h}}_{comb}(n)$ represents an estimate of the frequency response of the system COMB. Since the system COMB represents the combined dynamics of the control device and the neuromuscular admittance, the frequency response of the neuromuscular admittance can be estimated by using block diagram algebra:

$$\tilde{H}_{adm}(\jmath\omega, n) = \frac{H_{cd}(\jmath\omega)\tilde{H}_{comb}(\jmath\omega, n)}{H_{cd}(\jmath\omega) - \tilde{H}_{comb}(\jmath\omega, n)} \tag{10}$$

where $H_{cd}(\jmath\omega)$ is the known frequency response function of the control device, and $\tilde{H}_{comb}(\jmath\omega, n)$ is the Fourier Transform of $\tilde{\mathbf{h}}_{comb}(n)$ at the current time n.

To apply the RLS algorithm, an external disturbance force F_{dist} needs to be inserted into the control device. A common

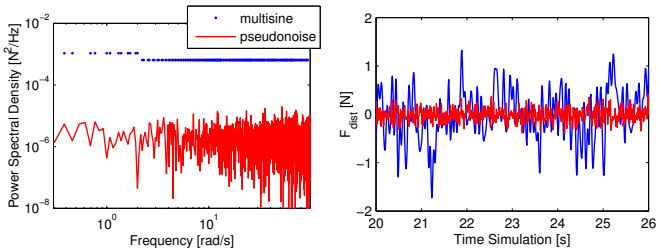

(a) Power spectral density. (b) Time realization.

Fig. 3. Power spectral density and time realization of the disturbance force F_{dist}. The multisine and pseudonoise components are shown separately.

choice for F_{dist} when estimating neuromuscular dynamics is the multisine signal [13]:

$$F_{dist}(n) = \sum_{j=1}^{N_d} D_j \sin(2\pi f_{D_j} n + \psi_{D_j}) \tag{11}$$

Each frequency f_{D_j} constitutes an integer multiple of a base frequency f_0. To capture all the neuromuscular dynamics, a frequency range was chosen between 0.07 and 95 rad/s. The amplitudes D_j were chosen according to the Reduced Power Method, which allows a full-bandwidth estimation of the admittance without influencing the human behavior at low frequencies [13]. The phases ψ_{D_j} were chosen randomly to obtain an unpredictable signal. A cresting technique was applied to avoid peaks in the time realization of the signal.

However, the RLS algorithm requires that the input must be persistently exciting, which means that the matrix $\mathbf{R}_D(n)$ in eq. (8) must be nonsingular. Unfortunately, it can be shown that the matrix $\mathbf{R}_D(n)$ associated with the multisine in eq. (11) is singular. To overcome this issue, a time realization of a Gaussian white noise was added to the multisine signal. The variance of the Gaussian noise was chosen small enough not to affect the behavior of arm admittance at low frequencies [13], while still guaranteeing the nonsingularity of the resulting matrix $\mathbf{R}_D(n)$. This additional pseudonoise signal is later treated as a deterministic excitation signal similarly to the multisine signal. Fig. 3 shows the time realization and power spectral density of the resulting signal F_{dist}.

V. Validation of the RLS algorithm in simulation

A. Method

A Monte-Carlo simulation was performed to investigate the robustness of the RLS algorithm in estimating the neuromuscular response with different levels of remnant noise N. The control task in Fig. 1 was numerically simulated in Matlab/Simulink. The dynamics of the controlled element CD were chosen as [3]:

$$H_{cd} = \frac{1}{s^2 + 50} \tag{12}$$

The human was simulated to perform different control tasks: opposing (Position Task) and being compliant (Force Task) with the force disturbance F_{dist}. These tasks induce humans to adopt minimum and maximum admittance, respectively. The parameters for the compliant admittance H^c_{adm}

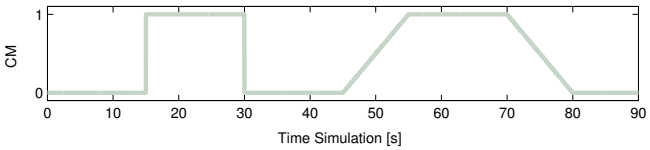

Fig. 4. Time evolution of the parameter CM, which determines the evolution of the neuromuscular dynamics. Values 0 and 1 correspond to compliant and stiff admittance, respectively.

TABLE III. Admittance parameters (**C**-Compliant, **S**-Stiff)

	m_{int}	b_{int}	k_{int}	b_{skin}	k_{skin}	k_a	k_v	k_p	τ	ω_0	β
	kg	$\frac{Ns}{m}$	$\frac{N}{m}$	$\frac{Ns}{m}$	$\frac{kN}{m}$	$\frac{Ns^2}{m}$	$\frac{Ns}{m}$	$\frac{N}{m}$	ms	$\frac{rad}{s}$	–
C	2.02	32.5	382	228	11.7	2.3	37.4	91	28.4	13.63	0.74
S	2.02	14.4	169	44	2.6	0	0	0	0	13.63	0.74

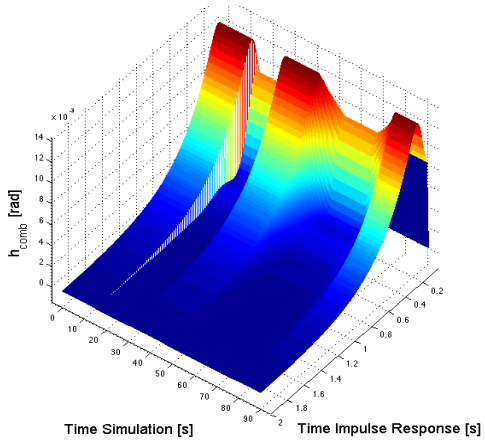

Fig. 5. Time evolution of the simulated impulse response $\mathbf{h_{comb}}$.

and the stiff admittance H^s_{adm} were chosen as estimated in a previous study, see Table III [3]. The time evolution of the neuromuscular dynamics was chosen as in a previous work [6]:

$$H_{adm} = CM(t)H^s_{adm} + (1 - CM(t))H^c_{adm} \tag{13}$$

where t represents the simulation time, and $CM(t)$ is shown in Fig. 4. Fig. 5 depicts the resulting time evolution of the impulse response $\mathbf{h}_{comb}(t)$.

As explained in Section IV, the input signal F_{dist} was chosen as a multisine signal combined with a pseudonoise, while the contribution of the central nervous system was assumed negligible (*from CNS* $= 0$). The remnant signal N was considered as Gaussian noise n_w with variance $\sigma^2_w = 1$ N^2, filtered by a third-order low pass filter H_n [14]:

$$H_n(s) = K_n \frac{\omega_n^3}{(s + \omega_n)(s^2 + 2\epsilon_n\omega_n s + \omega_n^2)} \tag{14}$$

where $\epsilon_n = 0.26$ and $\omega_n = 12.7$ rad/s. The value of K_n was gradually increased, in order to obtain three different ratios between remnant standard deviation σ_n and signal standard deviation $\sigma_{F_{hum}}$ (0%, 20% and 50%). For each value of K_n, 100 simulations were performed with different realizations of the remnant noise.

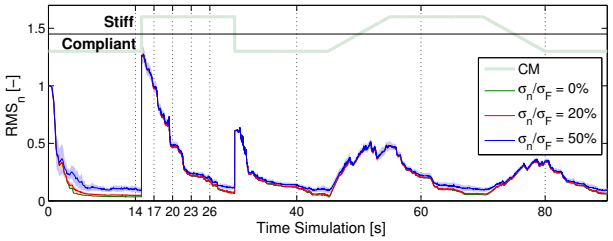

Fig. 6. Evolution of the normalized Root Mean Square error RMS_n between the simulated and the estimated impulse responses $\mathbf{h}_{comb}$. The RMS_n is shown for different ratios σ_n/σ_F between remnant and signal standard deviation.

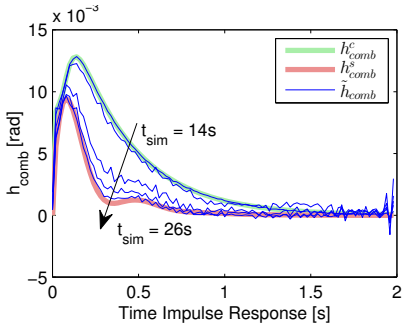

Fig. 7. Evolution of the estimate of the impulse response $\tilde{\mathbf{h}}_{\mathbf{comb}}$ for simulation times $t_{sim} = 14, 17, 20, 23, 26$ s. These values of t_{sim} are around 15 s, where $\mathbf{h}_{comb}$ instantaneously changes from $\mathbf{h}^c_{comb}$ to $\mathbf{h}^s_{comb}$. The estimates correspond to $\sigma_n/\sigma_F = 20\%$.

The simulated signals F_{hum} and δ_{cd} were sampled at $F_s = 100$ Hz and given as inputs to the RLS algorithm. Since the simulated impulse response was almost zero after $t_{imp} = 2$ s of the impulse response time (see Fig. 5), the memory of the estimated impulse response $\mathbf{h}_{comb}$ was set to $N_{imp} = F_s \cdot t_{imp} = 200$. The forgetting factor was set to $\lambda = 0.995$, in order to obtain a trade-off between noise rejection and capability of tracking the time-varying response [15].

To evaluate the reliability of the estimates given by the RLS algorithm, the normalized Root Mean Square error between the estimated and the simulated $\mathbf{h}_{comb}$ was calculated:

$$RMS_n(n) = \frac{\sum_{i=0}^{N_{imp}} \left(\tilde{\mathbf{h}}^{(i)}_{comb}(n) - \mathbf{h}^{(i)}_{comb}(n)\right)^2}{\sum_{i=0}^{N_{imp}} \left(\mathbf{h}^{(i)}_{comb}(n)\right)^2} \qquad (15)$$

where n represents the current simulation time instant $nT = n/F_s$, and $\mathbf{h}^{(i)}_{comb}(n)$ ($\tilde{\mathbf{h}}^{(i)}_{comb}(n)$) represents the i-th element of $\mathbf{h}_{comb}(n)$ ($\tilde{\mathbf{h}}_{comb}(n)$). As an indicator for the reliability of the admittance estimate in eq. (10), the relative error between the estimated and the simulated frequency response functions was calculated:

$$E(\jmath\omega) = \frac{\left|\tilde{\mathbf{H}}_{adm}(\jmath\omega, n) - \mathbf{H}_{adm}(\jmath\omega, n)\right|^2}{\left|\mathbf{H}_{adm}(\jmath\omega, n)\right|^2} \qquad (16)$$

B. Results

Fig. 6 shows the time evolution of the mean and standard deviation of $RMS_n(n)$ over the 100 simulations for different values of K_n. The time evolutions of $RMS_n(n)$ are similar for all the different values of K_n. The estimate matches the simulated dynamics with high accuracy ($RMS_n(n) < 0.3$) when the admittance parameters are constant or when they change slowly. The value of $RMS_n(n)$ increases to 1.2 when the admittance instantaneously varies from H^c_{adm} to H^s_{adm}, and the impulse response $\mathbf{h}_{comb}(n)$ consequently varies from $\mathbf{h}^c_{comb}$ to $\mathbf{h}^s_{comb}$ ($t = 15$ s).

To better investigate the behavior of the RLS algorithm during the time interval around $t = 15$ s, the evolution of the estimated $\tilde{\mathbf{h}}_{comb}(n)$ is shown in Fig. 7. The plot shows that the peak in the $RMS_n(n)$ is due to the high difference between the simulated impulse responses $\tilde{\mathbf{h}}^c_{comb}$ and $\tilde{\mathbf{h}}^s_{comb}$. In this situation, the algorithm RLS almost needs 8 s to converge to an accurate estimate.

The frequency response of the admittance was estimated by using eq. (10). Fig. 8 shows the relative error between the

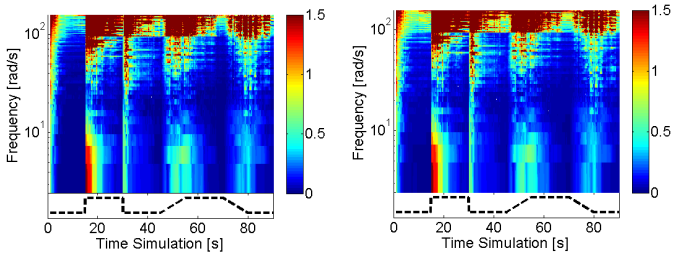

(a) $\sigma_n/\sigma_{F_{hum}} = 0\%$. (b) $\sigma_n/\sigma_{F_{hum}} = 20\%$.

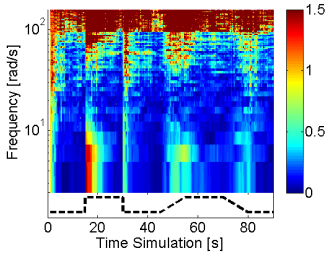

(c) $\sigma_n/\sigma_{F_{hum}} = 50\%$.

Fig. 8. Relative error between the estimated and the simulated admittance frequency responses.

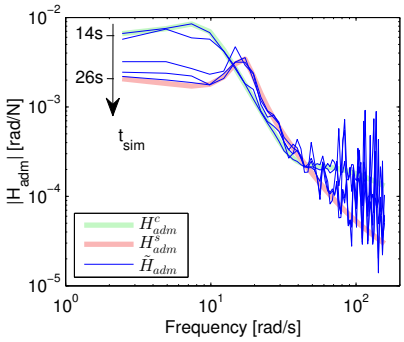

Fig. 9. Evolution of the estimate of the admittance frequency response function $\tilde{\mathbf{H}}_{adm}$ around the simulation time $t_{sim} = 15s$ when $\mathbf{H}_{adm}$ instantaneously varies from $\mathbf{H}^c_{adm}$ to $\mathbf{H}^s_{adm}$. The estimates correspond to t = 14, 17, 20, 23, 26 s. The corresponding σ_n/σ_F is 20%.

simulated and the estimated frequency responses, see eq. (16). Even with high level of remnant ($\sigma_n/\sigma_F = 50\%$), the relative error is low (blue color in Fig. 8) when the parameter are constant or change gradually. On the other hand, the estimated admittance needs more time to converge to the simulated model when the admittance parameters change instantaneously ($t = 15$ s). Fig. 9 shows the corresponding time evolution of the estimated admittance response during the time interval around $t = 15$ s for $\sigma_n/\sigma_F = 20\%$.

VI. Discussion

The main goal of the paper was to evaluate the reliability of an RLS-based method in estimating time-varying neuromuscular system dynamics in a set of Monte-Carlo simulations. This method uses a RLS algorithm to estimate the impulse response of the combined system of admittance and control device. Then, the admittance is calculated by using block diagram algebra. To the best of our knowledge, this is the first study to apply an RLS algorithm to estimate time-varying neuromuscular system dynamics.

Low relative errors between simulated and estimated admittance indicate that the RLS-based method is able to track slow changes in admittance dynamics. This is also valid for high levels of remnant noise. On the other hand, the RLS-based method needed about 8 s to provide reliable estimates when the admittance changed instantaneously.

The convergence time and the robustness of the RLS-based method are related to the chosen value of the forgetting factor λ. As shown in a previous work [11], the convergence time of a RLS algorithm is inversely proportional to $(1-\lambda)$. Therefore, choosing lower values of λ would reduce the convergence time. However, lower values of λ affect the robustness of the RLS algorithm to the remnant noise and could lead to instability problems [16]. Therefore, the value of λ is a compromise between convergence time and robustness to the remnant noise.

In our opinion, the selected value of λ could be employed to identify changes in neuromuscular system dynamics during a human-in-the-loop experiment. The chosen λ would allow slow changes in pilot behavior to be identified, e.g. changes due to fatigue. On the other hand, fast transient changes could not be detected.

VII. Conclusions

This paper has presented a method to online estimate a time-varying neuromuscular response. The method is based on a Recursive Least Square algorithm and assumes that the neuromuscular response can be approximated with a Finite Impulse Response filter. A set of Monte-Carlo simulations showed that the method provided accurate estimates in the time- and frequency-domain when the neuromuscular response was constant or changed gradually. In case of instantaneous admittance changes, the method converged to the new admittance dynamics after about 8 s.

Future work will focus on testing the developed algorithm with data measured during human-in-the-loop experiments and on extending the RLS algorithm to estimate the admittance during control tasks (with or without haptic aids).

Acknowledgment

Heinrich H. Bülthoff was supported by the Brain Korea 21 PLUS Program through the National Research Foundation of Korea funded by the Ministry of Education. Correspondence should be directed to Heinrich H. Bülthoff.

References

[1] D. A. Abbink, M. Mulder, and E. R. Boer, "Haptic Shared Control: Smoothly Shifting Control Authority?" *Cognition, Technology & Work*, vol. 14, no. 1, pp. 19–28, 2012.

[2] D. A. Abbink, M. Mulder, F. C. T. van der Helm, M. Mulder, and E. R. Boer, "Measuring Neuromuscular Control Dynamics During Car Following with Continuous Haptic Feedback," *IEEE Trans. Syst., Man, Cybern. B*, vol. 41, no. 5, pp. 1239–1249, 2011.

[3] A. C. Schouten, E. de Vlugt, J. J. B. van Hilten, and F. C. T. Van der Helm, "Quantifying Proprioceptive Reflexes During Position Control of the Human Arm," *IEEE Trans. Biomed. Eng.*, vol. 55, no. 1, pp. 311–321, Jan 2008.

[4] M. Olivari, F. M. Nieuwenhuizen, J. Venrooij, H. H. Bülthoff, and L. Pollini, "Multi-loop Pilot Behaviour Identification in Response to Simultaneous Visual and Haptic Stimuli," in *Proc. AIAA Model. and Simul. Technol. Conf.*, no. AIAA 2012-4795, Minneapolis, Minnesota, Aug. 2012, pp. 1–23.

[5] M. M. van Paassen, "Biophysics in Aircraft Control, a Model of the Neuromuscular System of the Pilot's Arm," Ph.D. dissertation, Delft Univ. of Technol., Delft, The Netherlands, 1994.

[6] M. Mulder, T. Verspecht, D. A. Abbink, M. M. Van Paassen, D. C. Balderas S, A. Schouten, E. de Vlugt, and M. Mulder, "Identification of Time Variant Neuromuscular Admittance Using Wavelets," in *Proc. IEEE SMC 2011*, 2011, pp. 1474–1480.

[7] J. MacNeil, R. Kearney, and I. Hunter, "Identification of Time-Varying Biological Systems from Ensemble Data (Joint Dynamics Application)," *IEEE Trans. Biomed. Eng.*, vol. 39, no. 12, pp. 1213–1225, Dec. 1992.

[8] M. Lortie and D. R. E. Kearney, "Identification of Physiological Systems: Estimation of Linear Timevarying Dynamics with non-White Inputs and Noisy Outputs," *Med. Biol. Eng. Comput.*, vol. 39, no. 3, pp. 381–390, May 2001.

[9] D. Ludvig and E. Perreault, "Interpretation of Non-Parametric Estimates of Time-Varying Systems," in *American Control Conference (ACC)*, Chicago, IL, Jun. 2012, pp. 2701–2706.

[10] D. C. Balderas Silva, F. C. T. Van der Helm, and A. C. Van der Schouten, "Time-Varying Identification of Human Properties Using the Wavelet Analysis," Ph.D. dissertation, Delft Univ. of Technol., Delft, The Netherlands, Dec. 2009.

[11] P. S. R. Diniz, *Adaptive Filtering: Algorithms and Practical Implementation*, ser. Kluwer International Series in Engineering and Computer Science. Springer, 2008.

[12] J. Venrooij, D. A. Abbink, M. Mulder, and M. M. van Paassen, "A Method to Measure the Relationship Between Biodynamic Feedthrough and Neuromuscular Admittance," *IEEE Trans. Syst., Man, Cybern. B*, vol. 41, no. 4, pp. 1158 –1169, Aug. 2011.

[13] W. Mugge, D. A. Abbink, and F. C. T. van der Helm, "Reduced Power Method: How to Evoke Low-Bandwidth Behaviour while Estimating Full-Bandwidth Dynamics," in *Proc. IEEE 10th ICORR*, Noordwijk, The Netherlands, Jun. 2007, pp. 575–581.

[14] P. M. T. Zaal, D. M. Pool, Q. P. Chu, M. M. van Paassen, M. Mulder, and J. A. Mulder, "Modeling Human Multimodal Perception and Control Using Genetic Maximum Likelihood Estimation," *J. of Guidance, Control, and Dynamics*, vol. 32, no. 4, pp. 1089–1099, 2009.

[15] A. Vahidi, A. Stefanopoulou, and H. Peng, "Recursive Least Squares with Forgetting for Online Estimation of Vehicle Mass and Road Grade: Theory and Experiments," *Vehicle System Dynamics*, vol. 43, no. 1, pp. 31–55, 2005.

[16] C. Paleologu, J. Benesty, and S. Ciochina, "A Robust Variable Forgetting Factor Recursive Least-Squares Algorithm for System Identification," *IEEE Signal Process. Lett.*, vol. 15, pp. 597–600, 2008.

4. Haptic feedback in compensatory tracking

This study was published and presented at KogWis 2014:

E.-R. Symeonidou, M. Olivari, H. H. Bülthoff and L. L. Chuang (2014) **The role of direct haptic feedback in a compensatory tracking task** *12th Biannual Conference of the German Cognitive Science Society (KogWis 2014), Tübingen, Germany*, Cognitive Processing, 15(Supplement 1) S71.

The role of direct haptic feedback in a compensatory tracking task

Evangelia-Regkina Symeonidou, Mario Olivari, Heinrich H. Bülthoff, Lewis L. Chuang
Max Planck Institute for Biological Cybernetics, Tübingen, Germany

Haptic feedback systems can be designed to assist vehicular steering by sharing manual control with the human operator. For example, direct haptic feedback (DHF) forces, that are applied over the control device, can guide the operator towards an optimized trajectory, which he can either augment, comply with or resist according to his preferences. DHF has been shown to improve performance (Olivari et al. submitted) and increase safety (Tsoi et al. 2010). Nonetheless, the human operator may not always benefit from the haptic support system. Depending on the amount of the haptic feedback, the operator might demonstrate an over- reliance or an opposition to this haptic assistance (Forsyth and MacLean 2006). Thus, it is worthwhile to investigate how different levels of haptic assistance influence shared control performance.

The current study investigates how different gain levels of DHF influence performance in a compensatory tracking task. For this purpose, 6 participants were evenly divided into two groups according to their previous tracking experience. During the task, they had to compensate for externally induced disturbances that were visualized as the difference between a moving line and a horizontal reference standard. Briefly, participants observed how an unstable air- craft symbol, located in the middle of the screen, deviated in the roll axis from a stable artificial horizon. In order to compensate for the roll angle, participants were instructed to use the control joystick. Meanwhile, different DHF forces were presented over the control joystick for gain levels of 0, 12.5, 25, 50 and 100 %. The maximal DHF level was chosen according to the procedure described in (Olivari et al. 2014) and represents the best stable performance of skilled human operators. The participants' performance was defined as the reciprocal of the median of the root mean square error (RMSE) in each condition.

Figure 1a shows that performance improved with in- creasing DHF gain, regardless of experience levels. To evaluate the operator's contribution, relative to the DHF contribution, we calculated the ratio of overall performance to estimated DHF performance without human input. Figure 1b shows that the subject's contribution in both groups de- creased with increasing DHF up to the 50 % condition. The contribution of experienced subjects plateaued between the 50 and 100 % DHF levels. Thus, the increase in performance for the 100 % condition can mainly be attributed to the higher DHF forces alone. In contrast, the inexperienced subjects seemed to completely rely on the DHF during the 50 % condition, since the operator's contribution approximated 1. However, this changed for the 100 % DHF level. Here, the participants started to actively contribute to the task (operator's contribution >1). This change in behavior resulted in performance values similar to those of the experienced group Our findings suggest that the increase of haptic support with our DHF system does not necessarily result in over-reliance and can improve performance for both experienced and inexperienced subjects.

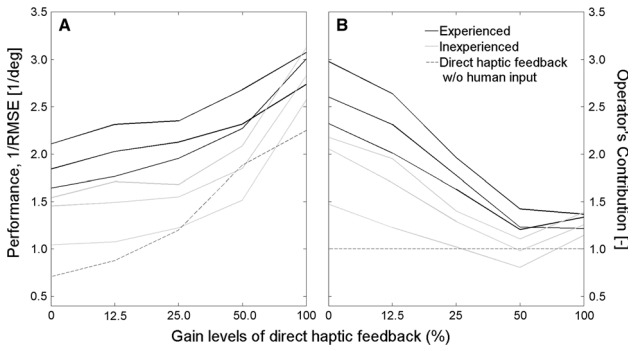

Fig. 1 **a** Performance of the experienced and in experienced participants as well as the baseline of direct haptic feedback (DHF) assistance without human input for increasing haptic gain. **b** The ratio of overall system performance to DHF performance without human input for increasing haptic gain

References

Forsyth BAC, MacLean KE (2006) Predictive haptic guidance: intelligent user assistance for the control of dynamic tasks. IEEE Trans Visual Comput Graph 12(1):103–13

Olivari M, Nieuwenhuizen FM, Bülthoff HH, Pollini L (2014) An experimental comparison of haptic and automated pilot support systems. In: AIAA modeling and simulation technologies conference, pp 1–11

Olivari M, Nieuwenhuizen F, Bülthoff H, Pollini L (submitted) Pilot adaptation to different classes of haptic aids in tracking tasks. J Guidance Control Dyn

Tsoi KK, Mulder M, Abbink DA (2010) Balancing safety and support: changing lanes with a haptic lane-keeping support system. In: 2010 IEEE international conference on systems, man and cybernetics, pp 1236–1243

5. Physiological workload measurements

This study was published and presented at the HCI International 2014 conference:

N. Flad, F. M. Nieuwenhuizen, H. H. Bülthoff and L. L. Chuang (2014) **System Delay in Flight Simulators Impairs Performance and Increases Physiological Workload** *11th HCI International 2014, Engineering Psychology and Cognitive Ergonomics, Springer International Publishing*, 3-11.

Abstract

Delays between user input and the system's reaction in control tasks have been shown to have a detrimental effect on performance. This is often accompanied by increases in self-reported workload. In the current work, we sought to identify physiological measures that correlate with pilot workload in a conceptual aerial vehicle that suffered from varying time delays between control input and vehicle response. For this purpose, we measured the skin conductance and heart rate variability of 8 participants during flight maneuvers in a fixed-base simulator. Participants were instructed to land a vehicle while compensating for roll disturbances under different conditions of system delay. We found that control error and the self-reported workload increased with increasing time delay. Skin conductance and input behavior also reflect corresponding changes. Our results show that physiological measures are sufficiently robust for evaluating the adverse influence of system delays in a conceptual vehicle model.

System Delay in Flight Simulators Impairs Performance and Increases Physiological Workload

Nina Flad[1], Frank M. Nieuwenhuizen[1], Heinrich H. Bülthoff[1,2], and Lewis L. Chuang[1,⋆]

[1] Department of Perception, Cognition and Action, Max Planck Institute for Biological Cybernetics, Tübingen
[2] Department of Cognitive and Brain Engineering, Korea University
{nina.flad,frank.nieuwenhuizen,heinrich.buelthoff, lewis.chuang}@tuebingen.mpg.de

Abstract. Delays between user input and the system's reaction in control tasks have been shown to have a detrimental effect on performance. This is often accompanied by increases in self-reported workload. In the current work, we sought to identify physiological measures that correlate with pilot workload in a conceptual aerial vehicle that suffered from varying time delays between control input and vehicle response. For this purpose, we measured the skin conductance and heart rate variability of 8 participants during flight maneuvers in a fixed-base simulator. Participants were instructed to land a vehicle while compensating for roll disturbances under different conditions of system delay. We found that control error and the self-reported workload increased with increasing time delay. Skin conductance and input behavior also reflect corresponding changes. Our results show that physiological measures are sufficiently robust for evaluating the adverse influence of system delays in a conceptual vehicle model.

1 Introduction

Delays between input and feedback in a closed-loop control task can result in both perceptual and control instabilities. For example, in head-slaved visualization systems (i.e., head-mounted virtual reality displays), temporal discrepancies between head movements and display updating can result in oscillopsia (also referred to as simulator sickness) in which the human operator perceives an unstable virtual environment that "swims around" his head [1]. In vehicle simulators, time delays between manual inputs and visual feedback can lead to notable increases in performance errors as well as perceived workload [2–4]. The latter can induce stress that induces physiological reactions in the autonomic nervous system.

⋆ The work in this paper was supported by the myCopter project, funded by the European Commission under the 7th Framework Program.

D. Harris (Ed.): EPCE 2014, LNAI 8532, pp. 3–11, 2014.

Previous studies of flight performance have shown that visual feedback delays can decrease performance and increase workload. For example, participants who performed a low-level flight task under visual lag conditions produced larger altitude errors and responded with higher workload scores on a questionnaire [5]. In a different study, increasing system delays decreased piloting performance as well as the subjective handling qualities of the aircraft, when pilots were required to perform a side-step maneuver in a helicopter simulation as well as actual test flight [4].

This decrease in performance can be more specifically attributed to the influence of visual feedback delays on closed-loop control performance. Trying to compensate for a time-delayed error has been shown to result in pilot-induced oscillations, wherein the control inputs from the pilot actually adds to the overall system disturbance instead of subtracting from it [2]. This is especially detrimental to the performance of precision tasks, such as hovering or landing. If the pilot is trained on such maneuvers in a simulator that suffers from time delays, more time is necessary to acquire the targeted skill and the transfer of training to real flight could be problematic, since a real aircraft with no system delays can be expected to respond differently [6]. Moreover, training with system delays has also been shown to increase the workload that is subjectively experienced by the pilot [5].

Many studies employ questionnaires to assess the participants' workload. Although this approach is well established, it has known weaknesses; the measurement is obtrusive and cannot be conducted during the task itself. Therefore, self-assessment of workload relies on the participant's recollection of the task, which could be subjectively altered.

An increase in workload can induce stress, which in turn leads to psychophysiological reactions of the autonomic nervous system. For example, induced workload can increase the heart rate as well as disrupt the regular fluctuations of inter-heartbeat-intervals [7]. In addition, it can widen the perspiratory glands and affect skin conductance [8]. Both heart activity and skin conductance can be measured using skin electrodes, thus providing an online metric for stress and workload during control activity itself.

In the current work, we investigate the influence of system delays on the control of a personal aerial vehicle (PAV) concept model [9]. We introduced delays of 0, 200, 400 or 600 ms and the influence of these delays was assessed in terms of our participants' control performance, control inputs, physiological responses and questionnaire results.

The remainder of this paper is organized as follows. Section 2 describes the flight task as well as the simulator and the aircraft model, followed by a description of data acquisition and analysis. Section 3 presents the results and possible interpretations. In section 4 we summarize our findings and discuss the implications for flight simulator studies.

Table 1. The parameters for the disturbance in the roll axis of the vehicle

i	a_i	ψ_i	f_i
1	0.5	0	0.0159
2	0.3	1	0.0796
3	0.2	0	0.0477
4	−0.2	1	0.0159

2 Methods

2.1 Participants

Eight male participants took part in our study. Their ages ranged between 22 and 34 years. All were researchers at the Max Planck Institute for Biological Cybernetics and had normal or corrected-to-normal vision.

2.2 Apparatus and Flight Model

We evaluated the effect of system delay of a dynamic PAV concept model in a fixed-base flight simulator. The simulator consisted of a display wall of nine screens taking a field-of-view of 105° by 100°. The participants used generic helicopter controls consisting of foot pedals, collective stick and cyclic stick.

The outside visualization was provided by Flightgear, an open-source flight simulator [10], while the control model was implemented in Matlab/Simulink and running at 256 Hz. The control model simulated the vehicle's dynamics and calculated the position and orientation of the aircraft based on the current control inputs. The outputs were then transformed into world coordinates and sent to the Flightgear computers that rendered the scene, namely San Francisco International Airport. The landing zone measured approximately 55 by 260 meters and was at the end of a runway (see Figure 1).

The PAV model represents an augmented helicopter with uncoupled cyclic, collective and pedal controls. Its rotational dynamics were of the Attitude Command-Attitude Hold (ACAH) type, such that a constant deflection of the cyclic stick resulted in a constant rotational attitude. Participants directly controlled a rate in the heave axis with the collective stick. A constant input on the pedals resulted in a specific rotational rate around the yaw axis. Subjects had full control over all the vehicle's degrees of freedom during each trial. In our experiment, a time delay of 0, 200, 400 or 600 msec was introduced between the control input and vehicle dynamics. These values were chosen based on a pilot study.

In addition, a disturbance was introduced in the roll axis during flight. Thus, our participants had to compensate for this disturbance even whilst performing the primary task of landing the PAV. The forcing function was a summation of four sinusoidal functions

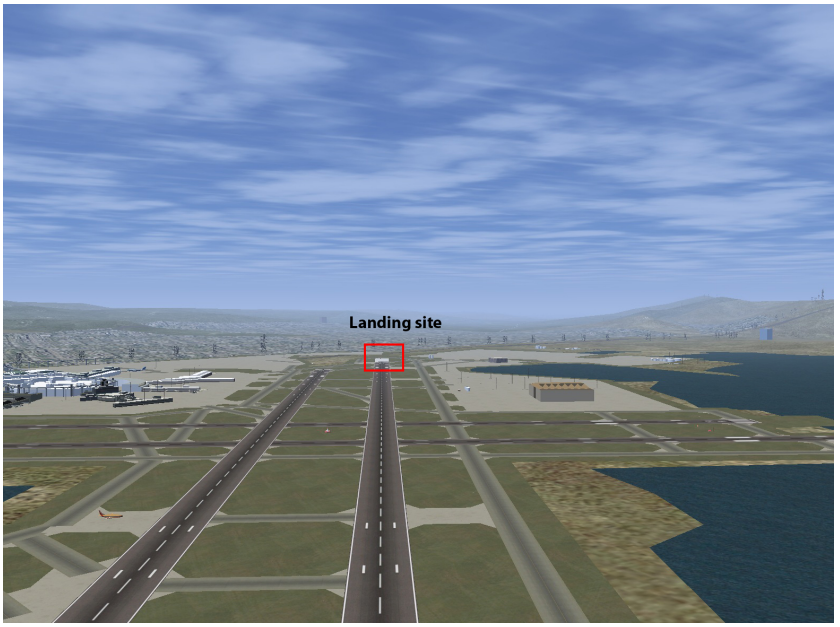

Fig. 1. Landing site as seen from the participants upon trial initiation

$$d(t) = \sum_{i=1}^{n} a_i * \sin(\psi_i * \frac{\pi}{2} + 2\pi * f_i * t) \tag{1}$$

with the parameters a_i, ψ_i and f_i given in Table 1.

2.3 Procedure

Our participants were instructed to fly the PAV from their initial position at the start of the trial towards the visible airport, follow the runway and land in a designated area at the end of the runway. In addition, they were required to maintain PAV stability and to compensate for disturbances in roll axis. Upon a successful landing, they were required to press a button to end the trial. Alternatively, each trial ended automatically if the maneuver was not successfully completed within eight minutes.

Prior to data collection, every participant had at least five one-hour training sessions with the simulator and the PAV model. During the first two training sessions, there were neither disturbance nor system delay to facilitate user familiarization with the control devices and the vehicle's dynamics. In addition, participants had to learn to navigate by relying on visual landmarks near the landing site. In the next two sessions, the roll disturbance was introduced, but without any time delay. Each training session always consisted of five flight sessions, separated by a thirty second break.

After the first four training sessions, the participants experienced at least one additional session under actual experimental conditions. The sessions for data collection consisted of four trials that varied in roll disturbance and time delay (0 ms, 200 ms, 400 ms and 600 ms) separated by a break of five minutes. In this break, participants were asked to rate workload with a digital version of the NASA-TLX questionnaire on a separate laptop. We collected ECG and skin conductance values during flight as well as during the breaks.

2.4 Data Collection and Analysis

Subjective workload was assessed using a computerized NASA Task Load Index (NASA-TLX). This rating scale consists of six independent scales, defined as follows [11]:

- Mental Demand (e.g. thinking, deciding, remembering, looking, etc.)
- Physical Demand (e.g. pushing, pulling, activating, etc.)
- Temporal Demand (e.g. time pressure)
- Performance
- Effort (required to achieve the level of performance)
- Frustration Level

This questionnaire was administered after every condition. It provides an overall workload score as well as scores for each individual scale and the composition of the overall score by the individual scales.

To measure performance, we calculated the root mean square error in compensating for the roll disturbances as well as control input activity. When participants experience a subjective loss of control or are performing badly, they tend to alter their input behavior or control effort. Therefore, we analyzed changes in the stick input activity. The stick input was collected at 256 Hz and analyzed in the frequency domain. We evaluated spectral densities in the frequencies higher than 0.1 Hz, since the disturbances took place in frequencies lower than 0.08 Hz. Thus, any changes in bandwidth above 0.1 Hz could be attributed to the pilot and not our disturbance function.

The first physiological measure is the skin conductance, which can be measured with a constant potential. The human skin possesses a natural electrical resistance, but contains sweat glands serving as conductive channels. Higher activity in the sweat glands results in lower resistance and better conductance [12]. The sweat glands are innervated by sympathetic activity only and, therefore, the skin conductance can serve as an indicator for stress and anxiety [8]. For the analysis, we normalized the mean conductance of each trial to a baseline measurement taken before the first test trial.

The second physiological measure is based on ECG measurements. The mean heart rate changes constant in response to changing environmental demands. These changes occur periodically and depend on the mental and physical state of the human. They are evoked by activity in the (para)sympathetic nervous system and have been found to be sensitive to work conditions, such as before and after

a driving task [7], or different phases of a monitoring and detection experiment [13]. We collected ECG data at 256 Hz and filtered it offline. The heart-beats in this signal were detected and the instantaneous heart-rate for every inter-beat-interval was calculated. We analyzed the spectral densities of the resampled time series in the 0.07–0.14 Hz band as well as the 0.15–0.4 Hz band. The power in the low frequencies is related to sympathetic activity, whereas the high frequency band is almost completely influenced by the parasympathetic nervous system in addition to respiration [14]. The low band is therefore widely regarded as the better measure for workload and stress.

3 Results and Discussion

All data was submitted to a one-way repeated measures analysis of variance (ANOVA) for the factor of time delay.

The questionnaire data showed an effect of system delay. The overall workload follows a linear trend ($F(3,21)=22.44$, $p<0.01$), indicating that increases in system delay induced higher subjective workload in our participants. The same linear trend can be found for the independent scales of the NASA-TLX. Interestingly, even though the self-rated performance decreased and the frustration increased, the participants did not "give up" on the task but increased their effort accordingly. In addition, the overall composition of the workload stayed the same (see figure 2). This suggests that the experimental manipulation of system delay increased subjective workload without changing the nature of the task itself.

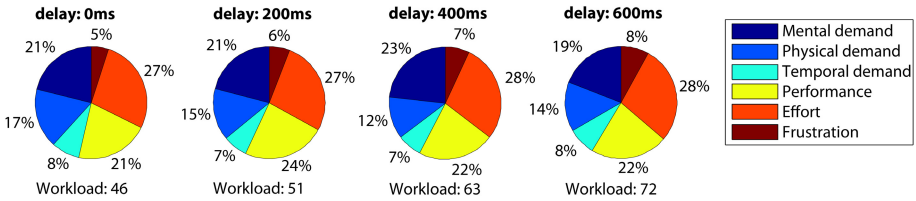

Fig. 2. Subjective workload increases with system delays but does not vary in its composition

As is the case with the self-rated performance, the objective error in compensating for the disturbance increased with increasing system delay ($F(3,21)=12.65$, $p<0.01$). Therefore, it follows that time delays have a deteriorating effect on the control task.

This deterioration in performance with increasing system delays evoked corrective inputs from the participants who tried to keep the vehicle stable. This is indicated by a linear increase in the power of the stick activity between 0.1 to 0.5 Hz ($F(3,21)=36.32$, $p<0.01$; see Figure 3). Since these disturbances take

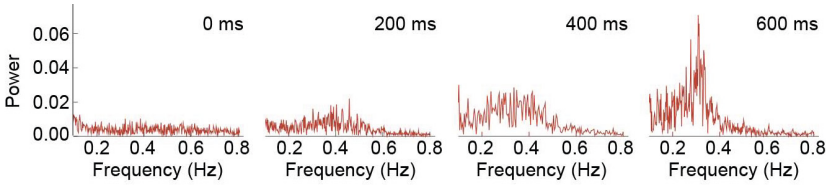

Fig. 3. Increasing input activity at frequencies higher than the disturbance. This can lead to pilot induced oscillations.

place at lower frequencies than these inputs, this behavior can destabilize the vehicle even more, resulting in pilot induced oscillations.

In correspondence with subjective workload measurements, an increase in system delays also resulted in higher skin conductance ($F(3,21)=5.72$, $p=0.01$, see figure 4). This indicates that participants experienced stress and arousal.

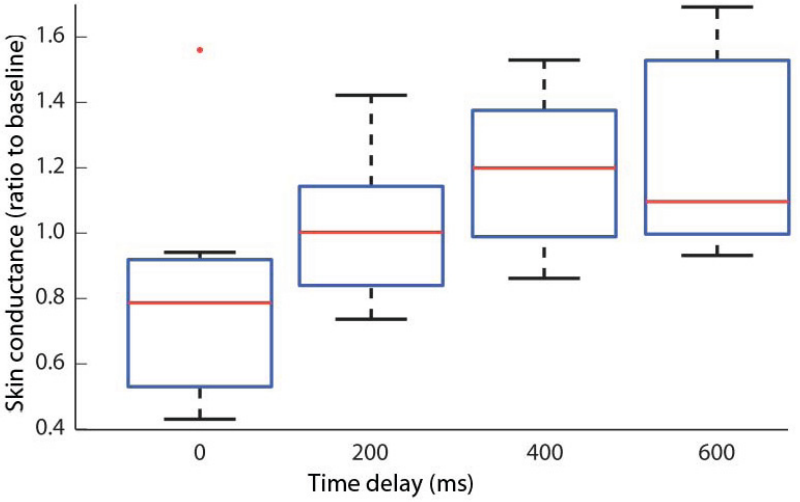

Fig. 4. The skin conductance increases linearly with increasing time delay

Nonetheless, the ECG measures for heart-rate and heart-rate variability did not show any significant changes to the manipulation of system delays. In addition, we did not find any changes between the test trials and breaks. Therefore, ECG based measures are not a reliable metric for stress and arousal in the current control task.

4 Conclusions

Overall, our findings show that delays between the control input and system response can impair control performance, elicit pilot-induced oscillations and increase workload, both in terms of self-reported and physiological measures. This is an important point to note in the design of virtual simulation systems, such as driving and flight simulators, that are intended for the purpose of training closed-loop control.

A system that is slow in responding to the human operator's input could induce the human operator to submit a larger response than is required for precise maneuvers. This results in a larger than intended vehicle response that needs to be corrected for subsequently. It could, thus, result in more errors than necessary and even instill counter-productive behavior that will have to be unlearned in the real world.

Our findings indicate that this loss of control has an impact on the operator's perceived and physiological workload. Therefore, system delays have a genuine influence on the operator's conscious sense of well-being as well as his physiological system.

In this work, we demonstrated that skin conductance activity can offer a complementary approach to the use of questionnaires. Changes in heart-based measurements might be too slow to indicate the changes in stress levels experienced by the human operator in our current experimental task. In contrast to a questionnaire, an unobtrusive measure such as this can be employed to assess multiple maneuvers in a complex mission. In addition to the traditional assessment of novel controller systems for their handling qualities, skin conductance measurements can allow the same systems to be evaluated for their physiological comfort.

To conclude, we demonstrate that system delays can detrimentally affect control performance due to pilot-induced oscillations. This has an adverse effect on the perceived workload of the operator as well as on his physiological system. The approach described here is a viable protocol for the evaluation of novel controller systems and simulators intended for closed-loop control.

References

1. Allison, R., Harris, L., Jenkin, M., Jasiobedzka, U., Zacher, J.: Tolerance of temporal delay in virtual environments. In: Proceedings IEEE Virtual Reality 2001, pp. 247–254 (2001)
2. Middendorf, M., Lusk, S., Whitley, J.: Power spectral analysis to investigate the effects of simulator time delay on flight control activity. In: AIAA Flight Simulation Technologies Conference, pp. 46–52 (1990)
3. Wildzunas, R.M., Barron, T.L., Wiley, R.W.: Visual display delay effects on pilot performance. Aviation, Space, and Environmental Medicine 67, 214–221 (1996)
4. Jennings, S., Reid, L.D., Craig, G., Kruk, R.V.: Time Delays In Visually Coupled Systems During Flight Test and Simulation. Journal of Aircraft 41, 1327–1335 (2004)

5. Middendorf, M., Fiorita, A., McMillan, G.: The effects of simulator transport delay on performance, workload, and control activity during low-level flight. In: AIAA Flight Simulation Technologies Conference (1991)
6. Riccio, G., Cress, J., Johnson, W.: The effects of simulator delays on the acquisition of flight control skills: Control of heading and altitude. In: Proceedings of the Human Factors and Ergonomics Society Annual Meeting, pp. 1186–1290 (1987)
7. Zhao, C., Zhao, M., Liu, J., Zheng, C.: Electroencephalogram and electrocardiograph assessment of mental fatigue in a driving simulator. Accident; Analysis and Prevention 45, 83–90 (2012)
8. Chattopadhyay, P., Bond, A., Lader, M.: Characteristics of galvanic skin response in anxiety states. Journal of Psychiatric Research 12, 265–270 (1975)
9. Perfect, P., Jump, M., White, M.D.: Development of handling qualities requirements for a personal aerial vehicle. In: Proceedings of the 38th European Rotorcraft Forum, Amsterdam, Netherlands (2012)
10. Perry, A.R.: The Flightgear flight simulator. In: 2004 USENIX Annual Technical Conference, Boston, MA (2004)
11. Hart, S., Staveland, L.: NASA Task Load Index (TLX) v1. 0 users manual (1986)
12. Montagu, J., Coles, E.: Mechanism and measurement of the galvanic skin response. Psychological Bulletin 65, 261–279 (1966)
13. Tattersall, A., Hockey, G.: Level of operator control and changes in heart rate variability during simulated flight maintenance. The Journal of the Human Factors 37, 682–698 (1995)
14. Camm, A., Malik, M.: Heart Rate Variability: Standards of Measurement. European Heart Journal of the Physiological Interpretation and Clinical Use (1996)

6. Influence of visualization on control performance

This study was published and presented at the HCI International 2014 conference:

M. Scheer, F. M. Nieuwenhuizen, H. H. Bülthoff and L. L. Chuang (2014) **The Influence of Visualization on Control Performance in a Flight Simulator** *11th HCI International 2014, Engineering Psychology and Cognitive Ergonomics, Springer International Publishing*, 202-211.

Abstract

Flight simulators are often assessed in terms of how well they imitate the physical reality that they endeavor to recreate. Given that vehicle simulators are primarily used for training purposes, it is equally important to consider the implications of visualization in terms of its influence on the user's control performance. In this paper, we report that a complex and realistic visual world environment can result in larger performance errors compared to a simplified, yet equivalent, visualization of the same control task. This is accompanied by an increase in subjective workload. A detailed analysis of control performance indicates that this is because the error perception is more variable in a real world environment.

The Influence of Visualization on Control Performance in a Flight Simulator

Menja Scheer[1], Frank M. Nieuwenhuizen[1], Heinrich H. Bülthoff[1,2], and Lewis L. Chuang[1,⋆]

[1] Department of Perception, Cognition and Action, Max Planck Institute for Biological Cybernetics, Tübingen
[2] Department of Cognitive and Brain Engineering, Korea University
{menja.scheer,frank.nieuwenhuizen,heinrich.buelthoff, lewis.chuang}@tuebingen.mpg.de

Abstract. Flight simulators are often assessed in terms of how well they imitate the physical reality that they endeavor to recreate. Given that vehicle simulators are primarily used for training purposes, it is equally important to consider the implications of visualization in terms of its influence on the user's control performance. In this paper, we report that a complex and realistic visual world environment can result in larger performance errors compared to a simplified, yet equivalent, visualization of the same control task. This is accompanied by an increase in subjective workload. A detailed analysis of control performance indicates that this is because the error perception is more variable in a real world environment.

1 Introduction

We rely on visual feedback to ensure stable motion and collision avoidance during self-motion. Visual feedback informs the human operator of the immediate difference between his desired goal and the consequences of his action. Thus, subsequent actions can be planned to minimize this difference. For that reason, it is important to ask how error feedback should be visualized to support good control performance in the human operator.

The real world is a rich source of visual information for supporting the control of self-motion. For example, the rate and the focus of expansion in retinal image changes (i.e., optic flow) can respectively help us discern our velocity and heading direction [1,2]. Given this, it is not surprising that virtual environments often strive to achieve high visual realism. This is especially true for flight simulators that are designed to train control performance, the success of which is subsequently vital for safety in a real vehicle. Several studies support this ambition. It has been shown in a flight simulator study that increasing the realism of ground terrain results in more accurate judgments in altitude as well as improved aiming [3]. Similarly, the altitude perception in pilots improved with higher object density in the visual environment [4].

⋆ The work in this paper was supported by the myCopter project, funded by the European Commission under the 7th Framework Program.

D. Harris (Ed.): EPCE 2014, LNAI 8532, pp. 202–211, 2014.

Nonetheless, this strive towards high visual fidelity may not always be necessary nor helpful. For example, it has been shown in a disturbance tracking task that a simple instrument can better support the control performance of human operator than optic flow alone [5]. Similarly, a driving simulator study demonstrated that control performance is independent of whether a realistic view of the road or just the lane itself is presented [6]. Given these findings, it stands to reason that if all information necessary to complete a task could be condensed in a simple instrument, it might be possible to achieve similar performance as in a real-world environment. In fact, one might even expect better performance from a simple visualization that exclusively presents only the information that is necessary for performing a given task. This relieves the operator from parsing the environment for task relevant information.

To investigate whether or not control performance is dependent on the realism of the visualization, the present study evaluated human participants on a closed-loop control task in a high-fidelity, fixed-base flight simulator. The structure of the task is depicted in Figure 1. The reference signal $f_t(t)$ represents the target to be followed. This reference signal was an unpredictable change in the roll angle of the simulated vehicle. This was not directly shown to the *Human Operator*. Instead, only the difference $e(t)$ between the desired roll angle $f_t(t)$ and the output of the system $\varphi(t)$ was displayed. In performing this task, the *Human Operator* has to continuously perceive his deviation from the target and to manually operate a control device to minimize this perceived error.

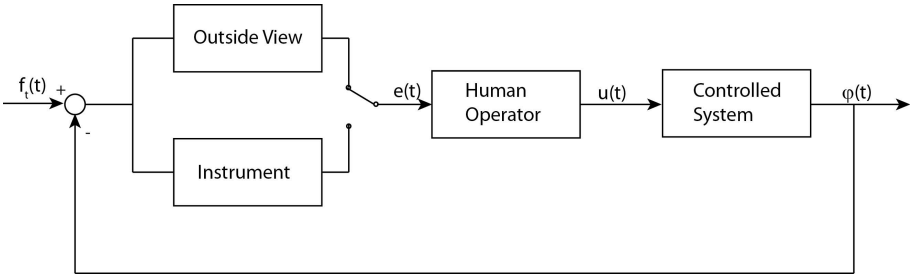

Fig. 1. Closed-loop control task of the presented study. The difference $e(t)$ between the output of the system $\varphi(t)$ and the unpredictable reference input $f_t(t)$ was presented in two different ways. Either using a simplified instrumental view (*Instrument*) or a complex visualization showing the outside view of an helicopter (*Outside View*). The human operators' task was to compensate for the disturbance introduced through the reference signal.

In our implementation of this control scheme, the *Human Operator* moved a control stick to continuously compensate for the displayed error. Moving the stick to the left or right resulted in stick deflections that were proportional to the roll rate $\dot{\varphi}(t)$ of the simulated aircraft. Thus, stick manipulations served as a direct input $u(t)$ to a *Controlled System* with single-integrator dynamics. The

output of the system was fed back and subtracted from the reference signal $f_t(t)$, resulting in the error $e(t)$ that was shown to the *Human Operator*.

As mentioned, there were the two possible visualizations for presenting this error feedback $e(t)$ to the *Human Operator*. This allowed us to investigate the influence of visualization complexity and was the only experimental manipulation in the current study. It is worth mentioning again that the reference signal $f_t(t)$ was the same regardless of the visualization. In other words, the task difficulty was the same regardless of the visualization shown. The *Instrument* visualization was comparable to an attitude indicator (commonly referred to as an artificial horizon), which is an aviation instrument that displays the aircraft's angular position with respect to the horizon (Figure 2). For the *Outside View* visualization, participants were presented with a view of a simulated real-world environment from an aircraft cockpit (Figure 3).

In the current study, we were interested in how the visualization of error feedback affected control performance. In addition, we were also motivated to know whether this influence of visualization would be accompanied by changes in subjective workload. To measure control performance, the output of the joystick $u(t)$ as well as the error $e(t)$ were recorded. $e(t)$ was the amount of error that remained in the system after the *Human Operator* resolved the continuous disturbance $f_t(t)$ to the system. Therefore, this value served as a basis for evaluating control performance. $u(t)$ was the amount of control input that the *Human Operator* submitted to the *Controlled System*. This was treated as a measure for control effort. To assess subjective workload, we requested participants to complete a computerized version of the NASA Task Load Index (NASA-TLX) questionnaire [7] after each given visualization.

2 Methods

2.1 Participants

Twelve participants (eight male), were recruited from the participant database of the Max-Planck Institute. They were aged between 21–37 years (mean: 29.1 years) and had normal or corrected-to-normal vision. All were right handed. They gave their written consent before the experiment and were paid 12 Euros per hour.

2.2 Apparatus and Flight Model

The current study was conducted in a fixed-based flight simulator that consisted of a main PC and display cluster. The main PC controlled the experiment and data collection with a customized software based on Matlab Simulink (Mathworks). This PC was connected to a cluster of nine independent visualization PCs, via a local area network and commanded the timing and presentation of the visualization using UDP triggers.

The visualization PCs were connected to a large display that consisted of nine panels (total field-of-view: 105° x 100°). In the *Instrument* condition, two

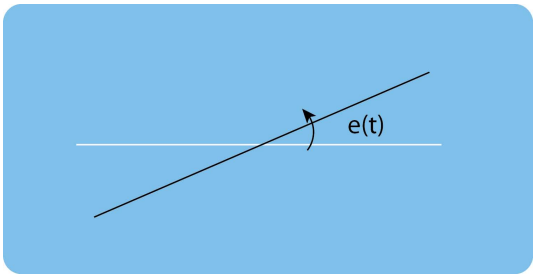

Fig. 2. *Instrument* condition, showing an artificial horizon. The error $e(t)$ is calculated from the reference signal $f_t(t)$ and the roll angle $\varphi(t)$.

lines were rendered on a blue background with Matlab Psychtoolbox, a black line that represented $e(t)$ and a white horizontal line that represented zero error [8,9] (Figure2). The *Outside View* condition used flight simulation software (i.e., FlightGear; [10]) to present a cockpit view of a straight-ahead flight path, through the hinterlands of San Francisco, wherein $e(t)$ resulted in rotations of the cockpit's view frustum and, hence, the entire scene (see Figure 3).

Inputs to the *Controlled System* were submitted via a joystick (Extreme 3D Pro, Logitech) that sampled at 256Hz. This only affected the roll angle of the visualization. The other degrees of freedom of the *Controlled System* were fixed.

A computerized NASA-TLX questionnaire was presented to the participants for the self-reporting of subjective workload via a laptop computer. This rating scale consists of six sub-scales (Mental Demand, Physical Demand, Temporal Demand, Performance, Effort, Frustration) [7].

2.3 Compensatory Tracking Task

In a compensatory tracking task, the participants needs to minimize the error between a target signal and the output of the system. In the current study, a disturbance $f_t(t)$ is continuously introduced into the system, which exclusively perturbs the roll angle of the *Controlled System*. Here, $f_t(t)$ was designed as quasi-random reference signal that consisted of a sum of 10 sine waves. These comprising sine waves were non-harmonically related. The disturbance function had a variance of 1.7 deg^2. More specifically we used the following function [11]:

$$f_t(t) = \sum_{j=1}^{N} A(j) sin(\omega(j) \cdot t + \phi(j)) \quad (1)$$

The amplitude, frequency and phase of the sinusoids are given in Table 1.

2.4 Procedure

Two sessions comprised the full experiment and were conducted on separate days. Two blocks were performed in each session and each block presented one

Fig. 3. Fixed-base flight simulator, consisting of nine panels and a field-of-view of 105° x 100°. Here the *Outside View* is shown. During the experiment, visual disturbances were experienced in the roll-axis around the horizon, that our participants were instructed to compensate for with the provided joystick.

Table 1. Values of the ten non-harmonically related sine waves of the target signal $f_t(t)$. With number of the sine wave j, the amplitude of the j_{th} sine wave equals A_j, the frequency is ω_j and the phase is ϕ_j .

j	A_j in deg	ω_j in rad/s	ϕ_j in rad
1	1.351	0.377	0.145
2	1.007	0.859	0.902
3	0.509	1.759	4.306
4	0.260	2.827	6.127
5	0.157	3.917	5.339
6	0.095	5.466	6.155
7	0.060	7.749	1.503
8	0.043	10.514	1.506
9	0.036	13.132	2.368
10	0.030	17.363	2.086

of the two possible visualizations (*Instrument*, *Outside View*). Three 5 mins trials were presented per block, with 5 mins breaks between them. The order of the blocks was counter-balanced for the visualization condition across sessions and participants.

Each session began with the participant reading and signing a consent form that provided experimental instructions. The computerized NASA-TLX questionnaire was administered after the completion of each block of trials for the

given visualization condition. Altogether, the experiment took 3.5 hours for every participant over the two sessions.

2.5 Data Collection and Analysis

To evaluate the performance, the normalized root mean squared value of the error signal $e(t)$ (nRMSerror) was calculated, as well as the root mean squared value of the control input $u(t)$ (RMSinput). The nRMSerror was normalized with the disturbance that was experimentally introduced to the system. Thus, a nRMSerror that is smaller than a value of 1 would indicate that our participants reduced the disturbance in the system, while a value that was larger than 1 would indicate that the participant introduced additional disturbances to the system. The nRMSerror can be further divided into the mean and variable error as follows:

$$nRMSerror = \sqrt{MeanError^2 + VariableError^2} \tag{2}$$

whereby $MeanError$ is simply defined over all measured time points i as,

$$MeanError = \frac{\sum_{i=1}^{N} e_i}{N} \tag{3}$$

and $VariableError$ as,

$$VariableError = \sqrt{\frac{\sum_{i=1}^{N} (MeanError - e_i)^2}{N}} \tag{4}$$

The mean error represents the distance of the mean of the error distribution from zero (i.e. the target) and the variable error represents the spread of the error distribution [12].

The RMSinput represents the control effort of the participants. A higher RMSinput indicates that the participants submitted more joystick input into the *Controlled System*.

These measures for control performance, control effort and subjective workload were submitted to a paired-sample t-test to test for statistical differences. An alpha-level of 0.05 was adopted as the criterion for significance.

3 Results and Discussion

Figure 4A shows that the *Outside View* visualization resulted in a larger nRMSerror than the *Instrument* visualization ($t(11)=-6.54$, $p < 0.05$). In fact, all of our participants had nRMSerror values that were larger than 1 when the *Outside View* visualization was presented. This means that their efforts to minimize error actually led to additional disturbances in the control system. It is necessary to point out that this was not due to the difficulty of the compensatory

control task per se. When presented with the *Instrument* visualization, all participants were able to achieve nRMSerror values that were lower than 1. This result highlights the critical influence of visualization on control performance.

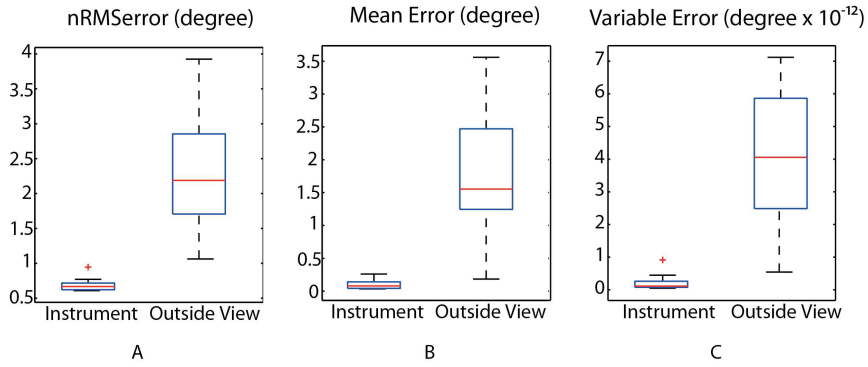

Fig. 4. Box-plots for the measures of nRMSerror (A), mean error (B) and variable error (C) across the condition of Visualization. Each box-plot shows the median, the interquartile range and data range. Outliers are represented as red crosses.

There are several explanations for this large difference in nRMSerror. First, our participants have failed to accurately estimate the desired goal from the *Outside View* visualization. Namely, the ideal attitude. If so, we would expect our participants' error distribution to be shifted away from the zero value, resulting in a bigger bias (e.g. mean error). Next, our participants could have been unable to accurately estimate the error from the *Outside View* visualization. If this was true, we would expect a high variable error. Figures 4B and 4C show that the mean error and the variable error were both larger for the *Outside View* compared to the *Instrument* condition (Mean Error: $t(11)=-5.77$, $p < 0.05$; Variable Error: $t(11)=-6.02$, $p < 0.05$). Therefore, our participants were less certain about the ideal state and were less precise in their control when they were presented with an *Outside View* visualization.

A time trace of the control error for both conditions (Figure 5) shows these two differences between the conditions. In the simple *Instrument* condition (light gray), the control error varied around the target with smaller mean and variable error. In the *Outside View* condition (black) the mean error is shifted over time with larger fluctuations around it.

In addition, the *Instrument* condition resulted in more input activity than the *Outside View* condition ($t(11)=5.59$, $p < 0.05$; see Figure 6). This indicates that the *Instrument* visualization induced our participants to invest more control effort into the task than for the *Outside View* visualization. This could be because error was better perceived from the *Instrument* visualization, resulting in more and better targeted control input. Conversely, participants could have submitted less control input in the *Outside View* visualization because they did not perceive the need for it.

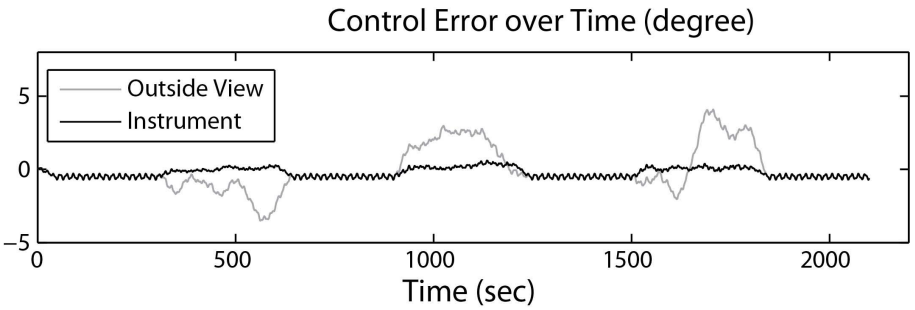

Fig. 5. Control error over time for the *Outside View* (light gray) and *Instrument* (black) condition. The data was filtered using a moving average filter with a window size of 40 seconds. In the *Instrument* condition the error varied around the target while in the *Outside View* condition, the mean of the error distribution is shifted over time.

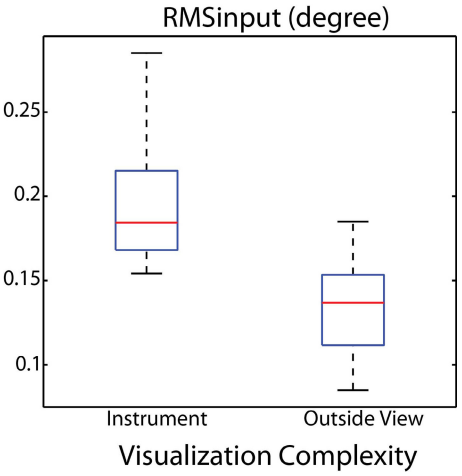

Fig. 6. Box-plots for RMSinput across the condition of Visualization. Each box-plot shows the median, the interquartile range and data range.

Subjective workload, as measured by the NASA-TLX scores, did not differ across the visualization condition ($t(11)=2.07$, $p = 0.07$). This supports our earlier conclusion. Although the participants did not perceive a difference in the difficulty of the same task across the different visualizations, the difference in their ability to accurately perceive their error resulted in very different control performance. The NASA-TLX scores indicate that mental demand (23%), performance (29%) and effort (23%) comprised more than 70% of the perceived workload in our task.

These findings show that control performance is better supported by a visualization that explicitly present the information that is required for the control task. In the current experiment, an explicit representation of the error supported the *Human Operator* in submitted the appropriate control inputs, without increasing his perceived workload. Unfortunately, competence in a complex control task such as piloting an aircraft with many degrees of freedom for a large repertoire of possible maneuvers often depend on multiple sources of information. It may not be feasible to create dedicated instruments for every relevant information channel. In this regard, the outside world might represent a more general and effective source of information than spreading one's visual attention across multiple instruments. This warrants further investigation.

In conclusion, the visualization of the error feedback can result in different levels of performance for two experimental conditions that are equivalent in terms of their difficulty and perceived workload. A simple visualization might lack the qualities of physical realism, but explicitly represents the primary property that is of interest to the human operator. This has the advantage of preventing the occurrence of unintended biases in error perception.

References

1. Browning, A.N., Grossberg, S., Mingolla, E.: A neural model of how the brain computes heading from optic flow in realistic scenes. Cognitive Psychology 59(4), 320–356 (2009)
2. Larish, J.F., Flach, J.M.: Sources of optical information useful for perception of speed of rectilinear self-motion. Journal of Experimental Psychology: Human Perception and Performance 16(2), 295 (1990)
3. Barfield, W., Rosenberg, C., Kraft, C.: The Effects of Visual Cues to Realism and Perceived Impact Point during Final Approach. In: Proceedings of the Human Factors and Ergonomics Society Annual Meeting, vol. 33(2), pp. 115–119 (October 1989)
4. De Maio, J., Rinalducci, E.J., Brooks, R., Brunderman, J.: Visual Cueing Effectiveness: Comparison of Perception and Flying Performance. In: Proceedings of the Human Factors and Ergonomics Society Annual Meeting, vol. 27(11), pp. 928–932 (1983)
5. Zaal, P.M.T., Nieuwenhuizen, F.M., van Paassen, M.M., Mulder, M.: Modeling Human Control of Self-Motion Direction With Optic Flow and Vestibular Motion. IEEE Transactions on Systems, Man, and Cybernetics. Part B, Cybernetics 43(2), 544–556 (2012)
6. Reed, M.P., Green, P.A.: Comparison of driving performance on-road and in a low-cost simulator using a concurrent telephone dialling task. Ergonomics 42(8), 1015–1037 (1999)
7. Hart, S.G., Staveland, L.E.: Development of NASA-TLX (Task Load Index). Results of Empirical and Theoretical Research (1988)
8. Brainard, D.H.: The Psychophysics Toolbox. Spatial Vision 10, 433–436 (1997)
9. Pelli, D.G.: The VideoToolbox software for visual psychophysics: transforming numbers into movies. Spatial Vision 10, 437–442 (1997)

10. Perry, A.: The flightgear flight simulator. In: USENIX Annual Technical Conference, Boston, M.A. (2004)
11. Nieuwenhuizen, F.M., Mulder, M., van Paassen, M.M., Bülthoff, H.H.: Influences of Simulator Motion System Characteristics on Pilot Control Behavior. Journal of Guidance, Control, and Dynamics 36(3), 667–676 (2013)
12. Jagacinski, R.J., Flach, J.M.: Control Theory for Humans - Quantitative Approaches to Modeling Performance, ch. 10, pp. 104–109. CRC Press, Mahwah (2002)

7. Novelty-P3 for indexing mental workload

This study was published and presented at KogWis 2014:

M. Scheer, H. H. Bülthoff and L. L. Chuang (2014) **Is the novelty-P3 suitable for indexing mental workload in steering tasks?** *12th Biannual Conference of the German Cognitive Science Society (KogWis 2014), Tübingen, Germany*, Cognitive Processing, 15(Supplement 1) S135-S136.

Is the novelty-P3 suitable for indexing mental workload in steering tasks?

Menja Scheer, Heinrich H. Bülthoff, Lewis L. Chuang
Max Planck Institute for Biological Cybernetics, Tübingen, Germany

Difficulties experienced in steering a vehicle can be expected to place a demand on one's mental resources (O'Donnell, Eggemeier 1986). While the extent of this mental workload (MWL) can be estimated by self-reports (e.g., NASA-TLX; Hart, Staveland 1988), it can also be physiologically evaluated in terms of how a primary task taxes a common and limited pool of mental re- sources, to the extent that it reduces the electroencephalographic (EEG) responses to a secondary task (e.g. an auditory oddball task). For example, the participant could be primarily required to control a cursor to track a target while attending to a series of auditory stimuli, which would infrequently present target tones that should be responded to with a button-press (e.g., Wickens, Kramer, Vanasse and Donchin 1983). Infrequently presented targets, termed oddballs, are known to elicit a large positive potential after approximately 300 ms of their presentation (i.e.,P3). Indeed, increasing tracking difficulty either by decreasing the predictability of the tracked target or by changing the complexity of the controller dynamics has been shown to attenuate P3 responses in the secondary auditory monitoring task (Wickens et al. 1983; Wickens, Kramer and Donchin 1984).

In contrast, increasing tracking difficulty—by introducing more frequent direction changes of the tracked target (i.e. including higher frequencies in the function that describes the motion trajectory of the target)—has been shown to bear little influence on the secondary task's P3 response (Wickens, Israel and Donchin 1977; Isreal, Chesney, Wickens and Donchin 1980). Overall, the added requirement of a steering task consistently results in a lower P3 amplitude, relative to performing auditory monitoring alone (Wickens et al. 1983; Wickens et al. 1977; Isreal et al. 1980).

Using a dual-task paradigm for indexing workload is not ideal. First, it requires participants to perform a secondary task. This prevents it from being applied in real-world scenarios; users cannot be expected to perform an unnecessary task that could compromise their critical work performance. Second, it can only be expected to work if the performance of the secondary task relies on the same mental resources as those of the primary task (Wickens, Yeh 1983), requiring a deliberate choice of the secondary task. Thus, it is fortunate that more recent studies have demonstrated that P3 amplitudes can be sensitive to MWL, even if the auditory oddball is ignored (Ullsperger, Freude and Erdmann 2001; Allison, Polich 2008). This effect is said to induce a momentary and involuntary shift in general attention, especially if recognizable sounds (e.g. a dog bark, opposed to a pure sound) are used (Miller, Rietschel, McDonald and Hatfield 2011).

The current work, containing two experiments, investigates the conditions that would allow 'novelty-P3', the P3 elicited by the ignored, recognizable oddball, to be an effective index for the MWL of compensatory tracking. Compensatory tracking is a basic steering task that can be generalized to most implementations of vehicular control. In both experiments participants were required to use a joystick to counteract disturbances of a horizontal plane. To evaluate the generalizability of this paradigm, we depicted this horizontal plane as either a line in a simplified visualization or as the horizon in a real-world environment. In the latter, participants experienced a large field-of-view perspective of the outside world from the cockpit of an aircraft that rotated erratically about its heading axis. The task was the same regardless of the visualization. In both experiments, we employed a full factorial design for the visualization (instrument, world) and 3 oddball paradigms (in experiment 1) or 4 levels of task difficulty (in experiment 2) respectively. Two sessions were conducted on separate days for the different visualizations, which were counter-balanced for order. Three trials were presented per oddball paradigm (experiment 1) or level of task difficulty (experiment 2) in blocks, which were randomized for order. Overall, we found that steering performance was worse when the visualization was provided by a realistic world environment in experiments 1 (F (1, 11) = 42.8, $p < 0.01$) and 2 (F (1, 13) = 35.0, $p < 0.01$). Nonetheless, this manipulation of visualization had no consequence on our participants' MWL as evaluated by a post-experimental questionnaire (i.e., NASA-TLX) and EEG responses. This suggests that MWL was unaffected by our choice of visualization.

The first experiment, with 12 participants, was designed to identify the optimal presentation paradigm of the auditory oddball. For the EEG analysis, two participants had to be excluded, due to noisy electrophysiological recordings (more than 50 % of rejected epochs). Whilst performing the tracking task, participants were presented with a sequence of auditory stimuli that they were instructed to ignore. This sequence would, in the 1-stimulus paradigm, only contain the infrequent odd- ball stimulus (i.e., the familiar sound of a dog's bark (Fabiani, Kazmerski, Cycowicz and Friedmann 1996)). In the 2-stimulus paradigm this infrequently presented oddball (0.1) is accompanied by a more frequently presented pure tone (0.9) and in

the 3-stimulus paradigm the infrequently presented oddball (0.1) is accompanied by a more frequently presented pure tone (0.8) and an infrequently presented pure tone (0.1). These three paradigms are widely used in P3 research (Katayama, Polich 1996). It should be noted, however, that the target to target interval is 20 s regardless of the paradigm. To obtain the ERPs the epochs from 100 ms before to 900 ms after the onset of the recognizable oddball stimulus, were averaged. Mean amplitude measurements were obtained in a 60 ms window, centered at the group- mean peak latency for the largest positive maximum component between 250 and 400 ms for the oddball P3, for each of the three mid-line electrode channels of interest (i.e., Fz, Cz, Pz). In agreement with previous work, the novelty-P3 response is smaller when participants had to perform the tracking task compared to when they were only presented with the task-irrelevant auditory stimuli, without the tracking task (F (1, 9) = 10.9, $p < 0.01$). However, the amplitude of the novelty-P3 differed significantly across the presentation paradigms (F (2, 18) = 5.3, $p < 0.05$), whereby the largest response to our task-irrelevant stimuli was elicited by the 1- stimulus oddball paradigm. This suggests that the 1-stimulus oddball paradigm is most likely to elicit novelty-P3 s that are sensitive to changes in MWL. Finally, the attenuation of novelty-P3 amplitudes by the tracking task varied across the three mid-line electrodes (F (2, 18) = 28.0, $p < 0.001$). Pairwise comparison, Bonferroni corrected for multiple comparisons, revealed P3 amplitude to be largest at Cz, followed by Fz and smallest at Pz (all $p < 0.05$). This stands in contrast with previous work that found control difficulty to attenuate P3 responses in parietal electrodes (cf., Isreal et al. 1980; Wickens et al. 1983). Thus, the current paradigm that uses a recognizable, ignored sound is likely to reflect an underlying process that is different from previous studies, which could be more sensitive to the MWL demands of a tracking task.

Given the result of experiment 1, the second experiment with 14 participants, investigated whether the 1-stimulus oddball paradigm would be sufficiently sensitive in indexing tracking difficulty as defined by the bandwidth of frequencies that contributed to the disturbance of the horizontal plane (cf., Isreal et al. 1980). Three different bandwidth profiles (*easy*, *medium*, *hard*) defined the linear increase in the amount of disturbance that had to be compensated for. This manipulation was effective in increasing subjective MWL, according to the results of a post- experimental NASA-TLX questionnaire (F (2, 26) = 14.9, $p < 0.001$) and demonstrated the expected linear trend (F (1, 13) = 23.2, $p < 0.001$). This increase in control effort was also reflected in the amount of joystick activity, which grew linearly across the difficulty conditions (F (1, 13) = 42.2, $p < 0.001$). For the EEG analysis two participants had to be excluded due to noisy electrophysiological recordings (more than 50 % of rejected epochs). A planned contrast revealed that the novelty- P3 was significantly lower in the most difficult condition compared to the baseline viewing condition, where no tracking was done (F (1, 11) = 5.2, $p < 0.05$; see Fig. 1a). Nonetheless, novelty-P3 did not differ significantly between the difficulty conditions (F (2, 22) = 0.13, $p = 0.88$), nor did it show the expected linear trend (F (1, 11) = 0.02, $p = 0.91$). Like (Isreal et al. 1980), we find that EEG-responses do not discriminate for MWL that is associated with controlling increased disturbances. It remains to be investigated, whether the novelty-P3 is sensitive for the complexity of controller dynamics, like it has been shown for the P3.

The power spectral density of the EEG data around 10 Hz (i.e., alpha) has been suggested by (Smith, Gevins 2005) to index MWL. A post hoc analysis of our current data, at electrode Pz, revealed that alpha power was significantly lower for the medium and hard conditions, relative to the view-only condition (F (1, 11) = 6.081, $p < 0.05$; (F (1, 11) = 6.282, $p < 0.05$). Nonetheless, the expected linear trend across tracking difficulty was not significant (Fig. 1b).

To conclude, the current results suggest that a 1-stimulus oddball task ought to be preferred when measuring general MWL with the

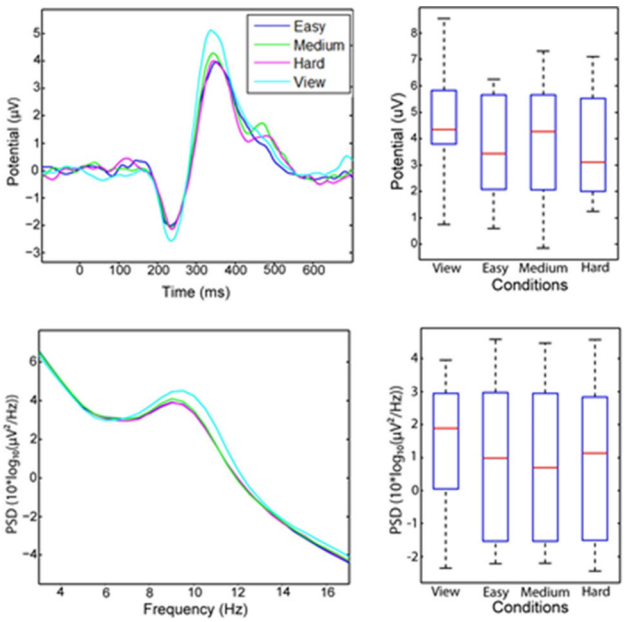

Fig. 1 **a** *left* Grand average ERP data of Experiment 2 averaged over Fz, Cz, Pz; *right* averaged amplitude of P3 as function of tracking difficulty. **b** *left* Averaged power spectral density (PSD) at Pz; *right* averaged PSD as a function of tracking difficulty

novelty-P3. Although changes in novelty-P3 can identify the control effort required in our compensatory tracking task, it is not sufficiently sensitive to provide a graded response across different levels of disturbances. In this regard, it may not be as effective as self-reports and joystick activity in denoting control effort. Nonetheless, further research can improve upon the sensitivity of EEG metrics to MWL by investigating other aspects that better correlate to the specific demands of a steering task.

Acknowledgments
The work in this paper was supported by the myCopter project, funded by the European Commission under the 7th Framework Program.

References

Allison BZ, Polich J (2008) Workload assessment of computer gaming using a single-stimulus event-related potential paradigm. Biol Psychol 77 (3):277–283

Fabiani M, Kazmerski V, Cycowicz Y, Friedmann, D. (1996) Naming norms for brief environmental sounds. Psychol Rev 33:462–475

Hart SG, Staveland LE (1988) Development of NASA-TLX (Task Load Index). Results of empirical and theoretical research

Isreal JB, Chesney GL, Wickens CD, Donchin E (1980) P300 and tracking difficulty: evidence for multiple resources in dual-task performance. Psychophysiology 17 (3):259–273

Katayama J, Polich J (1996) P300 from one-, two-, and three-stimulus auditory paradigms. Int J Psychophysiol 23, 33–40

Miller MW, Rietschel JC, McDonald CG, Hatfield BD (2011) A novel approach to the physiological measurement of mental workload. Int J Psychophysiol 80 (1):75–78

O'Donnell RC, Eggemeier TF (1986) Workload assessment methodology. Handbook of Perception and Human Performance, 2:1–49

Smith ME, Gevins A (2005) Neurophysiologic monitoring of mental workload and fatigue during operation of a flight simulator. Defense and Security (International Society for Optics and Photonics) 116–126

Ullsperger P, Freude G, Erdmann U (2001). Auditory probe sensitivity to mental workload changes—an event-related potential study. Int J Psychophysiol 40 (3):201–209

Wickens CD, Kramer AF, Vanasse L, Donchin E (1983) Performance of concurrent tasks: a psychophysiological analysis of the reciprocity of information-processing resources. Science 221 (4615):1080–1082

Wickens CD, Israel J, Donchin E (1977) The event related potential as an index of task workload. Proceedings of the Human Factors Society Annual Meeting 21, 282–286

Wickens CD, Kramer AF, Donchin E (1984). The event- related potential as an index of the processing demands of a complex target acquisition task. Annals of the New York Academy of Sciences 425 (955610):295–299

Wickens CD, Yeh Y-Y (1983) The dissociation between subjective workload and performance: A multiple resource approach. In: Proceedings of the human factors and ergonomics society annual meeting, 27(3):244–248

8. Looming auditory warnings

This study was published and presented at KogWis 2014:

C. Glatz, H. H. Bülthoff and L. L. Chuang (2014) **Looming auditory warnings initiate earlier eventrelated potentials in a manual steering task** *12th Biannual Conference of the German Cognitive Science Society (KogWis 2014), Tübingen, Germany*, Cognitive Processing, 15(Supplement 1) S38.

Looming auditory warnings initiate earlier event-related potentials in a manual steering task

Christiane Glatz, Heinrich H. Bülthoff, Lewis L.Chuang
Max Planck Institute for Biological Cybernetics, Tübingen, Germany

Automated collision avoidance systems promise to reduce accidents and relieve the driver from the demands of constant vigilance. Such systems direct the operator's attention to potentially critical regions of the environment without compromising steering performance. This raises the question: What is an effective warning cue?

Sounds with rising intensities are claimed to be especially salient. By evoking the percept of an approaching object, they engage a neural network that supports auditory space perception and attention (Bach et al. 2008). Indeed, we are aroused by and faster to respond to 'looming' auditory tones, which increase heart rate and skin conductance activity (Bach et al. 2009).

Looming sounds can differ in terms of their rising intensity profiles. While it can be approximated by a sound whose amplitude increases linearly with time, an approaching object that emits a constant tone is better described as having an amplitude that increases exponentially with time. In a driving simulator study, warning cues that had a veridical looming profile induced earlier braking responses than ramped profiles with linearly increasing loudness (Gray 2011).

In the current work, we investigated how looming sounds might serve, during a primary steering task, to alert participants to the appearance of visual targets. Nine volunteers performed a primary steering task whilst occasionally discriminating visual targets. Their primary task was to minimize the vertical distance between an erratically moving cursor and the horizontal mid-line, by steering a joystick towards the latter. Occasionally, diagonally oriented Gabor patches (10° tilt; 1° diameter; 3.1 cycles/deg; 70 ms duration) would appear on either the left or right of the cursor. Participants were instructed to respond with a button-press whenever a pre-defined target appeared. Seventy percent of the time, these visual stimuli were preceded by a 1,500 ms warning tone, 1,000 ms before they appeared. Overall, warning cues resulted in significantly faster and more sensitive detections of the visual target stimuli ($F_{1,8} = 7.72$, $p < 0.05$; $F_{1,8} = 9.63$, $p < 0.05$).

Each trial would present one of three possible warning cues. Thus, a warning cue (2,000 Hz) could either have a constant intensity of 65 dB, a ramped tone with linearly increasing intensity from 60 dB to approximately 75 dB or a comparable looming tone with an exponentially increasing intensity profile. The different warning cues did not vary in their influence of the response times to the visual targets and recognition sensitivity ($F_{2,16} = 3.32$, $p = 0.06$; $F_{2,16} = 0.10$, $p = 0.90$). However, this might be due to our small sample size. It is noteworthy that the different warning tones did not adversely affect steering performance ($F_{2,16} = 1.65$, $p < 0.22$). Nonetheless, electroencephalographic potentials to the offset of the warning cues were significantly earlier for the looming tone, compared to both the constant and ramped tone. More specifically, the positive component of the event- related potential was significantly earlier for the looming tone by about 200 ms, relative to the constant and ramped tone, and sustained for a longer duration (see Fig. 1).

The current findings highlight the behavioral benefits of auditory warning cues. More importantly, we find that a veridical looming tone induces earlier event-related potentials than one with a linearly increasing intensity. Future work will investigate how this benefit might diminish with increasing time between the warning tone and the event that is cued for.

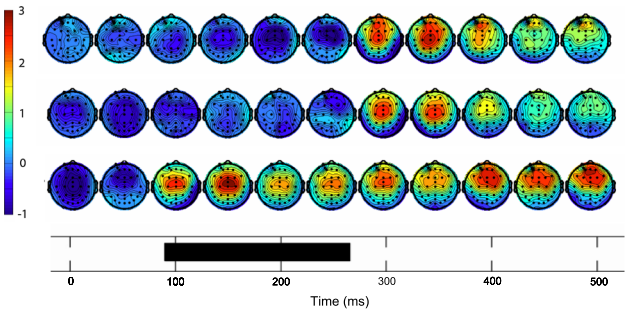

Fig. 1 The topographical plot shows the 500 ms after sound offset, with scalp maps plotted every 50 ms, for the constant (*row* 1), the ramped (*row* 2), and the looming tone (*row* 3). The looming cues evoked a strong positive deflection about 200 ms earlier than the other sounds. The *black bar* at the bottom of the figure indicates where the significance level of 0.01 was exceeded using a parametric test on the combined Fz, FCz, Cz, and Pz activity

References

Bach DR, Schchinger H, Neuhoff JG, Esposito F, Salle FD, Lehmann C, Herdener M, Scheffler K, Seifritz E (2008) Rising sound intensity: an intrinsic warning cue activating the amygdala. Cerebral Cortex 18(1):145–150

Bach DR, Neuhoff JG, Perrig W, Seifritz E (2009) Looming sounds as warning signals: the function of motion cues. Int J Psychophysiol 74(1):28–33

Gray R (2011) Looming auditory collision warnings for driving. Human Factors 53(1):63–74

9. Helicopter system identification

This paper was published and presented at the American Helicopter Society conference:

S. Geluardi, F. M. Nieuwenhuizen, L. Pollini and H. H. Bülthoff (2014) **Frequency Domain System Identification of a Light Helicopter in Hover** *70th American Helicopter Society International Annual Forum (AHS 2014)*, Curran, Red Hook, NY, USA, 1721-1731.

Abstract

This paper presents the implementation of a Multi-Input Single-Output fully coupled transfer function model of a civil light helicopter in hover. A frequency domain identification method is implemented. It is discussed that the chosen frequency range of excitation allows to capture some important rotor dynamic modes. Therefore, studies that require coupled rotor/body models are possible. The pitch-rate response with respect to the longitudinal cyclic is considered in detail throughout the paper. Different transfer functions are evaluated to compare the capability to capture the main helicopter dynamic modes. It is concluded that models with order less than 6 are not able to model the lead-lag dynamics in the pitch axis. Nevertheless, a transfer function model of the 4th order can provide acceptable results for handling qualities evaluations. The identified transfer function models are validated in the time domain with different input signals than those used during the identification and show good predictive capabilities. From the results it is possible to conclude that the identified transfer function models are able to capture the main dynamic characteristics of the considered light helicopter in hover.

FREQUENCY DOMAIN SYSTEM IDENTIFICATION OF A LIGHT HELICOPTER IN HOVER

Stefano Geluardi[a,b], **Frank M. Nieuwenhuizen**[a], **Lorenzo Pollini**[b] **and Heinrich H. Bülthoff**[a]
[a]Max Planck Institute for Biological Cybernetics, Tübingen, Germany
{stefano.geluardi, frank.nieuwenhuizen, heinrich.buelthoff}@tuebingen.mpg.de
[b]University of Pisa, Pisa, Italy
lorenzo.pollini@dsea.unipi.it

ABSTRACT

This paper presents the implementation of a Multi-Input Single-Output fully coupled transfer function model of a civil light helicopter in hover. A frequency domain identification method is implemented. It is discussed that the chosen frequency range of excitation allows to capture some important rotor dynamic modes. Therefore, studies that require coupled rotor/body models are possible. The pitch-rate response with respect to the longitudinal cyclic is considered in detail throughout the paper. Different transfer functions are evaluated to compare the capability to capture the main helicopter dynamic modes. It is concluded that models with order less than 6 are not able to model the lead-lag dynamics in the pitch axis. Nevertheless, a transfer function model of the 4^{th} order can provide acceptable results for handling qualities evaluations. The identified transfer function models are validated in the time domain with different input signals than those used during the identification and show good predictive capabilities. From the results it is possible to conclude that the identified transfer function models are able to capture the main dynamic characteristics of the considered light helicopter in hover.

INTRODUCTION

At the Max Planck Institute for Biological Cybernetics the interaction is investigated between a pilot with limited flying skills and augmented vehicles that will be part of a new concept of personal air transport systems (Ref. 1). This study will provide contributions to create a vehicle that is as easy to fly as it is to drive a car. This project is focused on light helicopters as these best reflect the properties of a vehicle that could be used in a personal air transport system. The flight state of interest throughout the project is hover, since it is commonly considered one of the most difficult to perform for a non-expert pilot. The goal of the project is to study which augmented system features allow a pilot with limited flying skills to reach similar performance as a highly-trained pilot. The project is composed of three main phases. The first phase is the identification of a rigid body dynamic model of a light helicopter. The second phase represents the realization of augmented systems for the model identified. The third phase consists of handling qualities and human performance evaluations in piloted closed loop control tasks, with and without the augmented systems. For the three phases the MPI CyberMotion Simulator (CMS) will be used, see Fig. 1. The 8 Degrees Of Freedom (DOF) robotic arm has a large motion envelope and is well suited to simulate the identified helicopter model in order to study the effects of augmentation techniques on non-expert pilots control performance.

This paper focuses on the first phase of the project, particularly on the implementation of a MISO (Multi Input Single Output) fully coupled transfer function model of a light helicopter in hover. Such helicopter model could be used for different possible applications, such as developing control-systems, making pilot handling-qualities evaluations in simulations, evaluating the fidelity of visual- and motion-systems of simulators and training pilots (Ref. 2). The implementation of a system identification model was preferred to a non-linear full-flight-envelope model. This choice relies on studies which demonstrated the deficiencies of a complex non-linear model in predicting some fundamental dynamics (Ref. 3). Indeed, dynamics like primary roll, vertical response

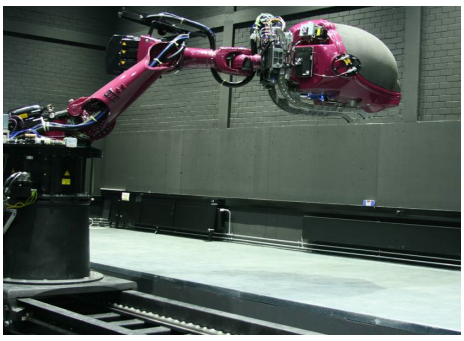

Fig. 1 The 8 DoF MPI CyberMotion Simulator (http://www.cyberneum.de/).

Presented at the AHS 70th Annual Forum, Montréal, Québec, Canada, May 20–22, 2014.

or pitch/roll cross-coupling may not be correctly captured if the model is implemented to be valid over the full-flight-envelope. Data collected for a specific condition can provide system identification models which have been proven to give better results. However, so far system identification for civil purposes has not been common in the helicopter field because of, e.g., expensive instrumentation usually used for military purposes, unavailability of multiple hours of flight tests and lack of interest from some civil companies in system identification studies. Therefore, identifying a civil helicopter model represents one of the main challenges of the project. The identification method implemented in this study is based on the frequency domain techniques developed in the last few decades and applied in many rotorcraft works (Refs. 4, 5).

An important aspect analyzed in this paper is the choice of the model dynamic complexity. A 6 DOF model is generally adequate for handling qualities evaluations. However, higher order model structures are necessary for applications like simulation validation or flight control system design (Ref. 6). Many works demonstrated that high bandwidth control systems for helicopter need to include rotor degrees of freedom (Ref. 7). Tischler investigated high order mathematical models and proved that for a hingeless single-rotor helicopter the coupled body/rotor-flapping mode limits the gain on attitude control feedback, while the lead-lag mode limits the gain on attitude-rate control feedback (Ref. 8). A variable-stability CH47 helicopter was used in (Ref. 9) to demonstrate how rotor dynamics and control system lags can influence the feedback gain limits. Recent studies by DLR in Germany have shown the importance of suppressing the air resonance due to the regressive lead-lag mode and particularly visible for high feedback gains in closed-loop controllers (Ref. 10). These studies suggest that considering rotor's DOF can be necessary to implement augmented control systems and to analyze their differences, which is one of the main goals of the current project. For this reason, model complexity analysis will be done to assess whether the identified transfer function models can capture body/rotor couplings. Furthermore, model reliability will be evaluated for handling qualities studies and for control system design.

This paper will present results on:

- implementing a SISO non-parametric model of a civil light helicopter in hover;
- conditioning the responses to consider the effect of secondary inputs and applying the composite windowing method;
- implementing a MISO parametric model;
- analyzing the model complexity;
- validating the identified MISO parametric models in the time domain with different input signals than those used during the identification.

DATA COLLECTION FOR IDENTIFICATION

The data for system identification were collected during two test flights, each with a duration of one hour. A Robinson R44 Raven II was used, which is a light helicopter with a single engine, a semi-rigid two-bladed main rotor and a two-bladed tail rotor. Several piloted frequency sweeps were recorded for each control axis to ensure the identification of the parametric transfer function models. Doublets and steps were also recorded to allow the validation of the identified models in the time domain with different input maneuvers. A preliminary training phase was necessary before and during flight to ensure that the pilot could safely and correctly perform the maneuvers of interest.

Two Global Positioning System antennas and an Inertial Measurement Unit were used that consisted of Fiber Optic Gyros and Micro Electrical Mechanical System accelerometers. These instruments allowed collecting the signals defined as the outputs of the model to be identified: the position of the helicopter with respect to the inertial frame, the attitude, the angular rates and the linear accelerations. Four optical sensors were chosen to measure the input signals from the pilot (two for the cyclic stick deflections, one for the collective lever, and one for the pedals). A sample rate of 100 Hz was chosen for all signals. A frequency range of excitation between 0.3 and 17 rad/s was considered during the piloted sweeps. The details of the flight tests are presented in (Ref. 11)

In Fig. 2 the time data of two concatenated frequency sweeps are shown for the longitudinal axis. Each frequency sweep has a duration of about 100 seconds. The sweep maneuvers start in hover with a few seconds of trim and end with the same initial trim condition. The longest period of the sweeps is of about 20 s which corresponds to a frequency of about 0.05 Hz. Then the pilot slowly increases the frequency of the sweep till the period of 0.4 s is reached ($\approx$ 2.5 Hz). In the figure the primary helicopter responses to the longitudinal stick deflection are also shown. It can be seen how the variation of the pitch rate reaches a maximum of about 20 deg/sec. This size of excitation ensures the identification of models which are also accurate for maneuvers with large excursions. The high frequency content visible in the pitch rate (q) is not present in the longitudinal translational velocity (u) and in the pitch angle (θ) where only low frequencies are generally involved. This high frequency content is important for the model complexity analysis involving body/rotor couplings. For this reason, the pitch rate response q/δ_{long} will be considered in detail throughout the paper. Concatenating two or more frequency sweeps as seen in Fig. 2 allows to obtain a rich spectral content over the frequency range of interest. Therefore the same procedure was applied to the other control axes.

IDENTIFICATION

In the past few decades system identification in the rotorcraft field has grown considerably. This is probably due to a better

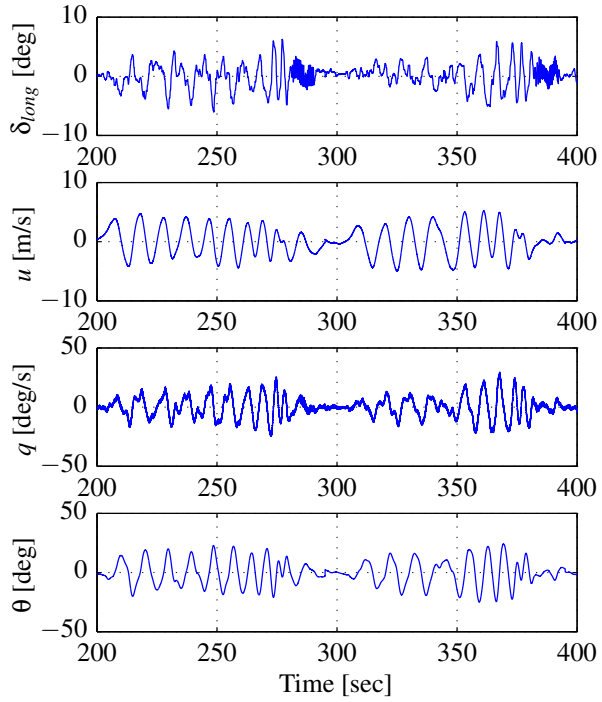

Fig. 2 A frequency sweep in the longitudinal axis in hover. δ_{long} = cyclic longitudinal deflection, u = longitudinal translational velocity, θ = pitch angle, q = pitch rate.

understanding of system identification theories and to novel applications of identified helicopter models such as control system design (Ref. 12). Among the different system identification methods the one proposed by Tischler in (Ref. 13) has been applied for many helicopter studies. Very good results were obtained that confirmed and validated the reliability of this method. The benefits derived from applying this method are mainly due to the fact that it is frequency based. This means that a non-parametric system identification phase can be implemented which allows to get some preliminary information about the model structure. Moreover, frequency responses conditioned by multiple partially correlated inputs can be computed. Finally, procedures like composite windowing and tools like the coherence function can be used to improve and analyze the results. For these reasons, this method was considered well suited for the purpose of the current study. Many system identification works based on this method were implemented by using the Comprehensive Identification from FrEquency Responses (CIFER®) software package. However, the results presented in this paper were obtained by implementing the method with the numerical computation environment MATLAB®. An important step of the identification process is to determine the complexity of the model and, therefore, which dynamics need to be included. This generally depends on the frequency range of interest and on the number of dynamical states measured during the flight tests (Ref. 14). For the present project the collection of data did not include any direct measurement of rotor-state dynamics. Nevertheless, it will be shown how the frequency range exited during the test flights allows to capture some rotor dynamic modes. Therefore, the implementation of higher order rotor/body models is possible.

Non-parametric SISO and MISO identification

The first step of the considered system identification method is the generation of a frequency response database containing the entire set of nonparametric single-input single-output frequency responses. These responses are obtained by concatenating two or three frequency-sweep time histories collected during the flight tests, as shown in Fig. 2. Then, the Fast Fourier Transform is applied by using overlapped-windowed spectral averaging. An example is shown in Fig. 3 with the bode plot of the pitch rate response estimation to the longitudinal stick deflection (q/δ_{long}). Here a window of 20 seconds was used. The figure shows also the coherence function which is an important tool at this stage since it permits assessing the goodness of the collected data (Ref. 15). This function can assume values between zero and one and indicates the fraction of the output spectrum linearly related to the input spectrum. A decrease in the coherence function can be due to process noise, nonlinearities, lack of input excitation or lack of rotorcraft response. Generally, coherence values of 0.6 and above are considered acceptable (Ref. 16). In Fig. 3 it can be seen that the q/δ_{long} frequency response shows a good level of coherence within the considered frequency range of excitation (0.3-17 rad/s).

However, using only one window increases the accuracy over a limited range of frequencies. This can be noticed in Fig. 3 where at high frequencies there is an increase in the random error that is reflected in the magnitude and the phase oscillations, even though the coherence function remains above the boundary of 0.6. Choosing a smaller window would reduce the random error but introduces a loss of accuracy at lower frequencies. To overcome this issue a procedure called composite windowing can be used during the nonparametric identification. In this procedure the conditioned frequency responses are computed with windows of different size. Then, a weighted nonlinear Least-Squares minimization method is implemented that provides the composite-conditioned frequency responses. The new responses calculated in this way are characterized by a good coherence and low random error over the entire frequency range of interest. Usually, the choice of the windows is done by considering the minimum and the maximum frequency desired for the identification (Ref. 17). For the present study a window of 40 seconds and one of 7 seconds were selected respectively as the largest and the smallest one. Three more windows were evenly distributed between these two for a total of five different window sizes.

Helicopter system identification studies requires that input-output couplings and multiple partially correlated inputs effects are taken into account in order to compute the actual SISO frequency responses. The multi-input identification technique allows to consider these effects by means of the

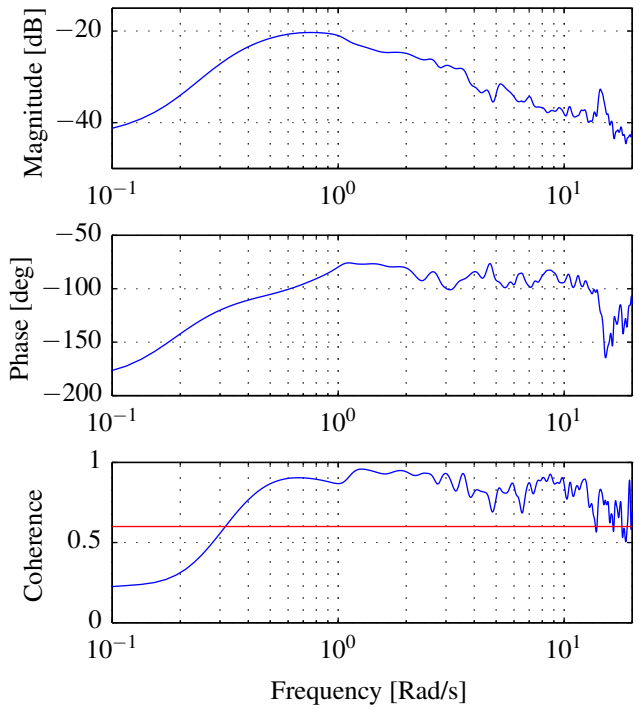

Fig. 3 Pitch axis SISO frequency response q/δ_{long}.

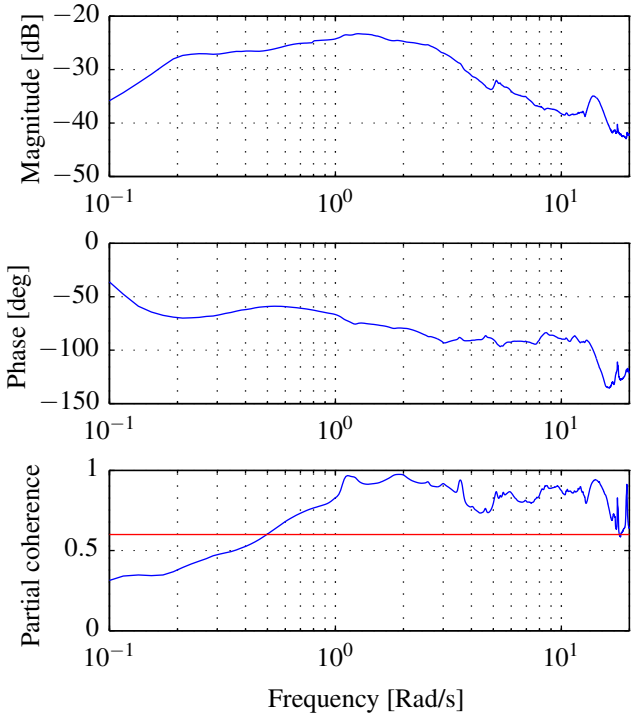

Fig. 4 Pitch axis MISO conditioned frequency response q/δ_{long} with composite windowing method applied.

so-called conditioned auto- and cross-spectra (Ref. 15). These allow to compute the conditioned frequency responses and the related partial coherences. The application of the conditioned-spectra and the composite method generated a set of 36 input-output conditioned frequency responses and the associated partial coherence functions. This result represent the final step of the non-parametric system identification process. An example of conditioned frequency response obtained by applying the composite windowing method is shown in Fig. 4 for the pitch-rate response q/δ_{long}. It is possible to notice how the response has a different shape with respect to the one in Fig. 3 due to the subtraction of the partially correlated inputs effects. Furthermore, the accuracy increases at higher frequencies due to the composite windowing procedure. The application of these methods makes much easier to recognize some important dynamical characteristics. At about 0.7 rad/sec the influence of the unstable phugoid mode appears while the resonance at about 14 rad/sec is due to the lightly damped regressive lead-lag mode. Similar analysis were considered for the other on- and off-axis conditioned frequency responses in which the effects of some rotor dynamic modes appeared as well as for the pitch response. From these evaluations it was possible to conclude that the considered frequency range of excitation is large enough to capture some important rotor dynamic modes.

Transfer function modeling identification

Once all the input-output conditioned frequency responses have been computed, two possible parametric system identification methods can be considered: the transfer function and the state-space modeling identification. In this paper the transfer function modeling procedure is implemented since it provides useful information on the fundamental dynamic characteristics and allows many key applications, such as handling qualities analysis and flight dynamic modeling for control system design (Ref. 18). Furthermore, comparing the matching quality of transfer-function models that differ in complexity can give information concerning the order of the system, the level of couplings and initial reasonable values for some parameters that could later be used for building a state-space identification model (Ref. 17). Transfer function models are obtained by fitting individual input-output frequency responses through the minimization of magnitude and phase errors. A detailed description of this approach is given in (Ref. 13). Different models were selected to fit the data response of each input-output axis over the selected frequency range (0.3-17 rad/s). The choice of the models was done in order to ensure a physical meaning and to avoid any over-parameterization that could lead to poor predictive capabilities.

The pitch-rate response to longitudinal stick input q/δ_{long} will be now considered in detail. Different models were selected to fit the frequency response and to adequately capture the main pitch dynamic modes. The first transfer function model considered is a coupled body/rotor 6^{th} order model used to represent the effects of the phugoid, the short period and the regressive lead-lag modes. The transfer function model and the relative fit cost is presented in Table 1. It can be noticed that a cost function is obtained well below 100, com-

monly considered in literature as a limit to ensure satisfactory accuracy.

Table 1 Pitch response transfer function models

Model	Transfer function[a]	Fit cost
6^{th} order	$\frac{0.11(3.928)[-1,0.327][0.213,14.265]e^{-0.019s}}{[-1,0.683][0.93,2.065][0.1,14.336]}$	6.17
4^{th} order	$\frac{0.14(1.317)[-1,0.361]e^{-0.023s}}{[-1,0.733][0.947,1.33]}$	37.94

[a]Shorthand notation: [ξ,ω] indicates $s^2+2\xi\omega s+\omega^2$, ξ damping ratio, ω natural frequency (rad/sec); (1/T) indicates $s+(1/T)$, rad/sec

This result is reflected in the bode plot in Fig. 5 where it can be seen how the transfer function response follows the measured data with good accuracy. In this transfer function model each dominant dynamic mode is represented with a pair of complex conjugate poles. For the unstable phugoid mode the complex poles are located at 0.683 rad/sec as it was expected from the non-parametric MISO identification. Another pair of highly damped complex poles at 2.065 rad/sec allows to model the short period. Its effect is visible in Fig. 5 with a decrease of the magnitude and the phase. The rotor lead-lag mode effects are modeled with two complex poles at 14.336 rad/sec as also predicted in the non-parametric MISO phase. The effect of this mode is recognizable in the magnitude plot with a relevant peak and in the phase plot with a roll off. Finally, a residual equivalent time delay of 0.019 seconds is added to represent the effective delays related to sensor filtering, linkage dynamics between the stick and the rotor and additional non-modeled high frequency rotor dynamics. The error function plot shown in Fig. 6, is computed as difference in magnitude (dB) and phase (deg) between the real frequency response and the estimated response. The error is compared with the mismatch boundaries defined in the MIL-STD-1797 (Ref. 13). These boundaries represent the Maximum Unnoticeable Added Dynamics (MUAD) limits. When they are exceeded a pilot can detect a divergence in the modeled aircraft response characteristics (Ref. 19). They have been considered to evaluate the effects of unnoticeable dynamics in many helicopter identification studies (Refs. 6, 20). As can be seen in Fig. 6, the error is well within the boundaries for the entire frequency range of interest, which means that a pilot would consider the model responses almost indistinguishable from the actual flight response. This is generally considered a good starting point for handling-qualities analyses. Furthermore, it can be also concluded that this model is well suited for augmented control system design due to its ability to capture rotor DOFs relevant for this purpose.

A second 4^{th} order transfer function model was considered for comparisons to the 6^{th} order model. The 4^{th} order model transfer function shown in Table 1 is based on the theory presented in (Ref. 21) where the classic fuselage longitudinal modes (phugoid and short period) are modeled with

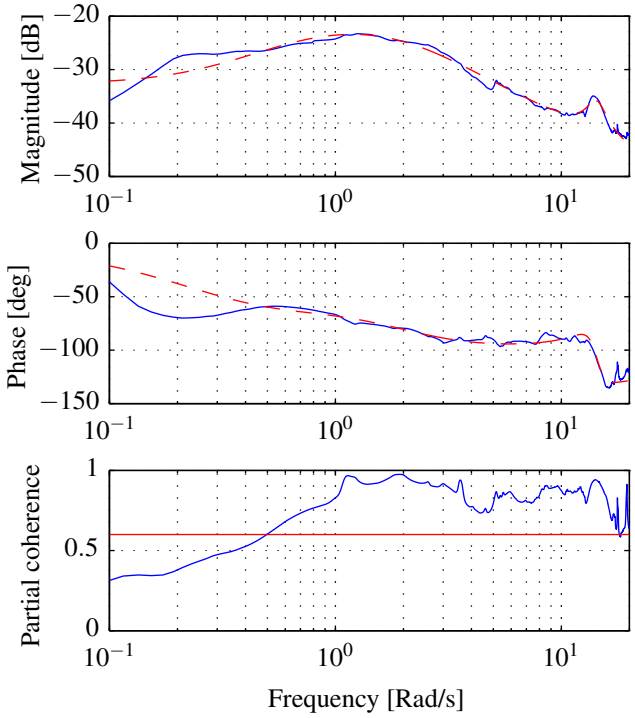

Fig. 5 Bode plot of the transfer function 6^{th} order model for the pitch response q/δ_{long}. Flight data in continuous line. Model data in dashed line.

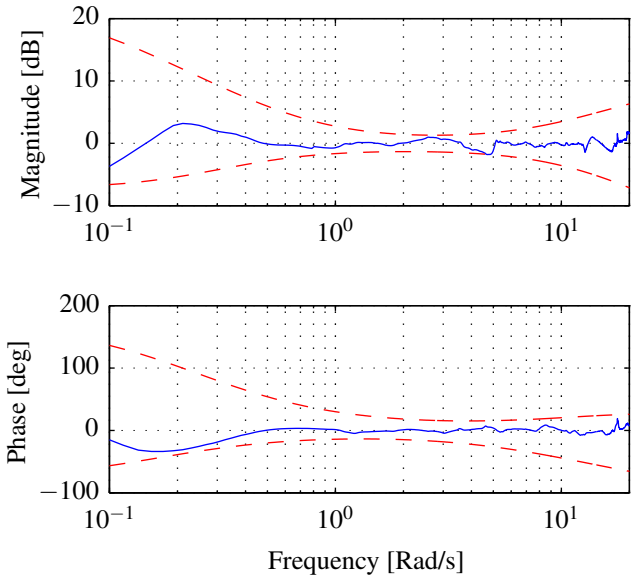

Fig. 6 Error transfer function of the q/δ_{long} response for the 6^{th} order model with MUAD boundaries.

two pairs of complex poles whereas the rotor mode effects are included as equivalent time delay. The phugoid mode is represented with a pair of complex poles at 0.733 rad/sec which again confirms the effect of this mode at around 0.7 rad/sec as expected from the non-parametric MISO identification. The fuselage short period mode is modeled with another pair of

complex poles at 1.33 rad/sec. Furthermore, a larger equivalent time delay is necessary than the one used for the 6^{th} order model to account for residual high frequency rotor dynamics. As can be seen in Fig. 7 the reduced order model still presents good accuracy over the entire frequency range but it is not able to adequately capture the high frequency lead-lag mode effects. For this reason the associated cost function shown in Table 1 is higher than for the 6^{th} order model but still within the guideline boundary. In Fig. 8 it can be also noticed how

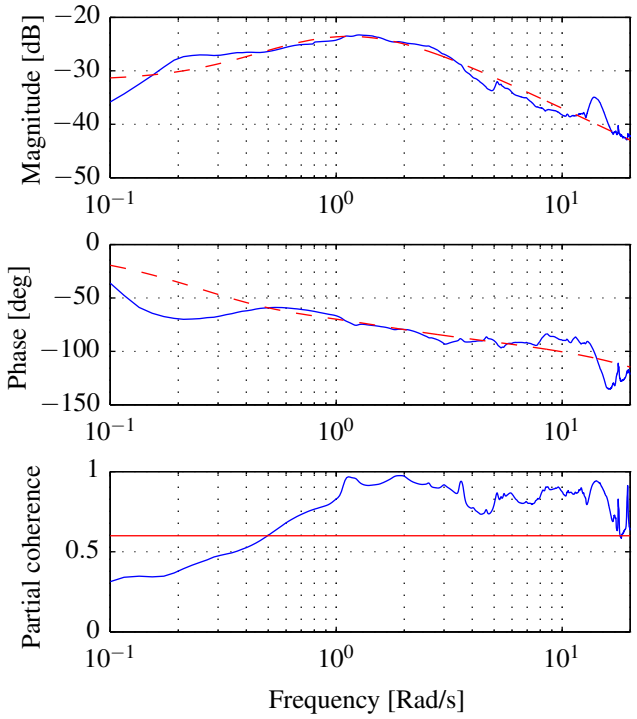

Fig. 7 Bode plot of the transfer function 4^{th} order model for the pitch response q/δ_{long}. Flight data in continuous line. Model data in dashed line.

the error increases at higher frequencies due to the fact that the rotor dynamic modes are not modeled. Nevertheless, it remains within the MUAD mismatch boundaries. Therefore, it is possible to conclude that the 4^{th} order transfer function model is well suited for handling-qualities analyses, but its incapability to capture high frequency rotor modes makes it inadequate for control system design. Other lower order models were considered to fit the pitch response but none of them were capable to represent the main dynamic modes of the longitudinal response since cost functions were well above the guideline limit of 100 and error functions were outside the MUAD limits.

Further transfer function models that are associated with responses considered relevant for hover and low-speed flight are presented in APPENDIX A. These include the dominant angular-rate responses to the cyclic and pedal control inputs (q/δ_{long}, p/δ_{lat}, r/δ_{ped}) and the vertical axis acceleration to the collective input (a_z/δ_{col}). The described transfer function

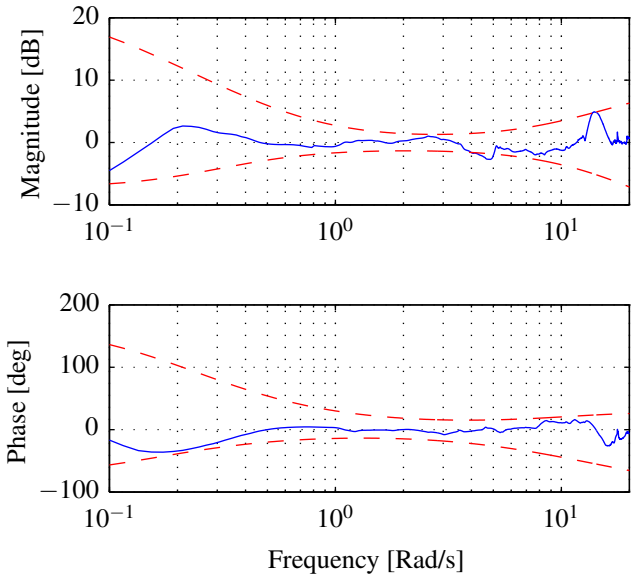

Fig. 8 Error transfer function of the q/δ_{long} response for the 4^{th} order model with MUAD boundaries.

models are capable of capturing the rotor modes important for control system design. For these identified models, cost function values less than 100 were obtained, which means that they adequately represent the dynamics of the chosen helicopter in the considered hover condition. This is a favorable result considering that only two hours of test flights with a non-experienced test pilot were sufficient to collect reliable data for system identification studies.

MISO model time-domain validation

The final step of the MISO system identification presented in this paper involves the time domain validation of the identified parametric models. This method is implemented by using different maneuvers (doublets or steps) from those used during the identification process (frequency sweeps). The method is based on the theory proposed by Tischler in (Ref. 13). Again the pitch axis is considered in detail. As the transfer function models contained an unstable phugoid mode at around 0.7 rad/sec, the simulations used for validation can easily diverge from the measured helicopter response. Therefore, a time record of a few seconds is considered to evaluate the identified pitch model. Obviously, the maneuver performed by the pilot involved the use of all the controls to maintain the helicopter stability. Therefore, also the small contribution of the other inputs is taken into account for the validation. Fig. 9 shows the result for the q/δ_{long} response. The 6^{th} and the 4^{th} order models responses are indistinguishable. The main control input δ_{long} is shown over time and the model responses are compared with the measured one. The fit error of both models was approximately 1.4 and the Theil Inequality Coefficient (TIC) approximately 0.06 and these metrics are considered in literature to evaluate the goodness of the model prediction (Ref. 22). A fit error less than 2.0 usually represents

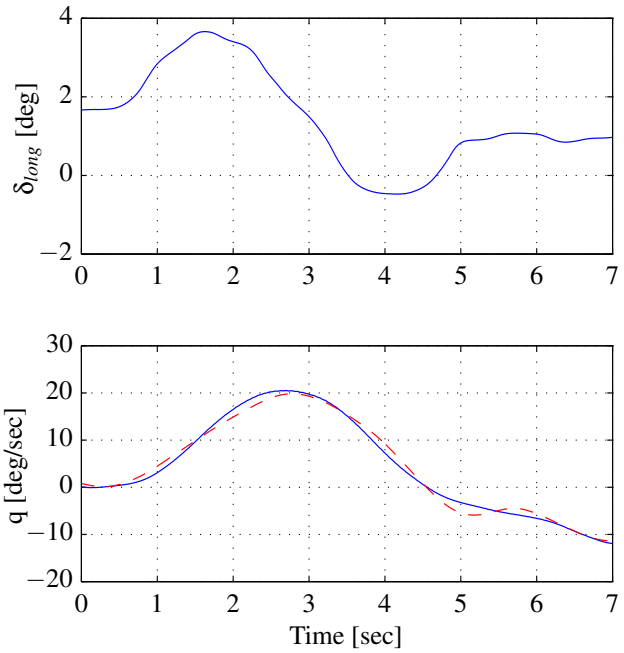

Fig. 9 Time domain 6th and 4th order model verification for longitudinal response q/δ_{long}. Flight data in continuous line. Model data in dashed line.

acceptable level of accuracy. The TIC is instead a normalized criterion. A TIC equal to zero means perfect predictive capability while a TIC equal to one means no predictive capability. Similar results are also obtained from the other responses which are detailed in APPENDIX B.

CONCLUSIONS

This paper has presented results on the implementation of a fully coupled transfer function model for a civil light helicopter in hover. From the obtained frequency responses, it was deduced that the chosen frequency range of excitation allows to capture some important rotor dynamic modes. Therefore, studies can be done that require coupled rotor/body models like control system design. The pitch-rate response with respect to the longitudinal cyclic was considered in detail and it was concluded that transfer function models with order lower than 4 cannot satisfactorily fit the main longitudinal helicopter modes since cost functions and Maximum Unnoticeable Added Dynamics boundaries are exceeded. Furthermore, it was concluded that a 6th order transfer function model is necessary to properly capture the rotor high frequency lead-lag mode needed to implement control system design studies. However, a 4th order transfer function model can already provide acceptable results for handling qualities studies. Finally, the identified transfer function models were validated in the time domain with different input signals than those used during the identification. Both models provided good predictive capability as expected from the results obtained in the frequency domain.

The results presented in this paper represent a starting point for the development of a state-space identification model. After that, the fully coupled state-space model will be used to implement different augmented control systems. The last step of the project consists of the validation of the augmented systems through handling qualities and human performance evaluations in piloted closed loop control tasks performed with the MPI CyberMotion Simulator.

APPENDIX A

In this appendix, the transfer function models for the dominant angular-rate responses to the cyclic and pedal control inputs (q/δ_{long}, p/δ_{lat}, r/δ_{ped}) and the vertical axis acceleration to the collective input (a_z/δ_{col}) are presented. The bode plot of the transfer functions fitted on the conditioned frequency responses and the relative error functions are shown in Figs 10-15. The obtained models and the cost functions are indicated in Table 2. For each response the dominant modes are

Table 2 Transfer function models main hover responses

Model	Transfer function[a]	Fit cost
p/δ_{lat}	$\frac{0.338(0.98)[0.21,16.6][0.37,12.1]e^{-0.001s}}{[0.1,14.336][0.97,1.76][0.8,13.9]}$	34.16
r/δ_{ped}	$\frac{0.02[1,7.85]}{[1,2.52]}$	95.23
a_z/δ_{col}	$\frac{0.05(0)(10.34)e^{-0.028s}}{(0.24)}$	15.98

[a]Shorthand notation: [ξ,ω] indicates $s^2+2\xi\omega s+\omega^2$, ξ damping ratio, ω natural frequency (rad/sec); (1/T) indicates s+(1/T), rad/sec

chosen based on the models considered in literature. In Fig.10 the p/δ_{lat} lateral response shows a similar lead-lag mode to the q/δ_{long} longitudinal response and the same pair of complex poles at 14.336 rad/sec is considered. Furthermore, the dutch-roll and the lateral-flapping modes are modeled with two pairs of complex poles at 1.76 and 13.9 rad/sec respectively. In Fig. 12 the a_z/δ_{col} frequency response shows the coning inflow effect with a high frequency peak in the magnitude plot. This phenomenon is particularly visible in hover when the collective position rapidly changes. The coning inflow effect is approximated by adding a zero at 10.34 rad/sec and a time delay ($e^{-0.028s}$) to the 1st order model used to represent the heave mode. Finally, the r/δ_{ped} frequency response is presented in Fig.14. Here, the yaw damping mode is modeled with a second order system. The error function plots in Figs. 11, 13 and 15 show good results for the p/δ_{lat} and the a_z/δ_{col} responses but for the considered r/δ_{ped} model the error function exceeds the boundaries for frequencies below 2 rad/sec.

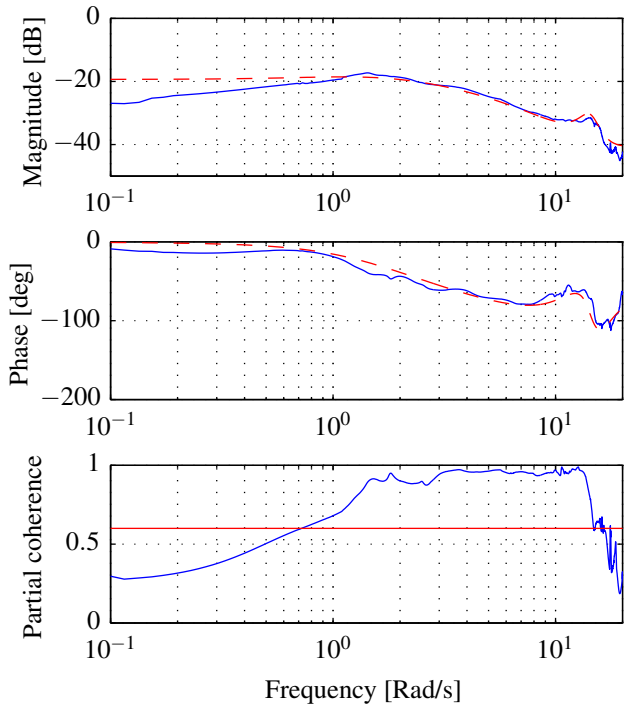

Fig. 10 Transfer function bode plot roll response p/δ_{lat}. Flight data in continuous line. Model data in dashed line.

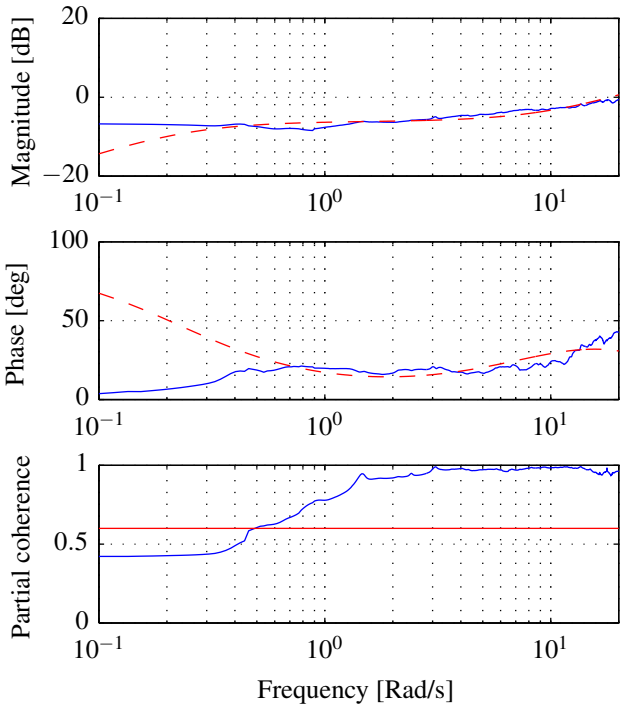

Fig. 12 Transfer function bode plot heave response a_z/δ_{col}. Flight data in continuous line. Model data in dashed line.

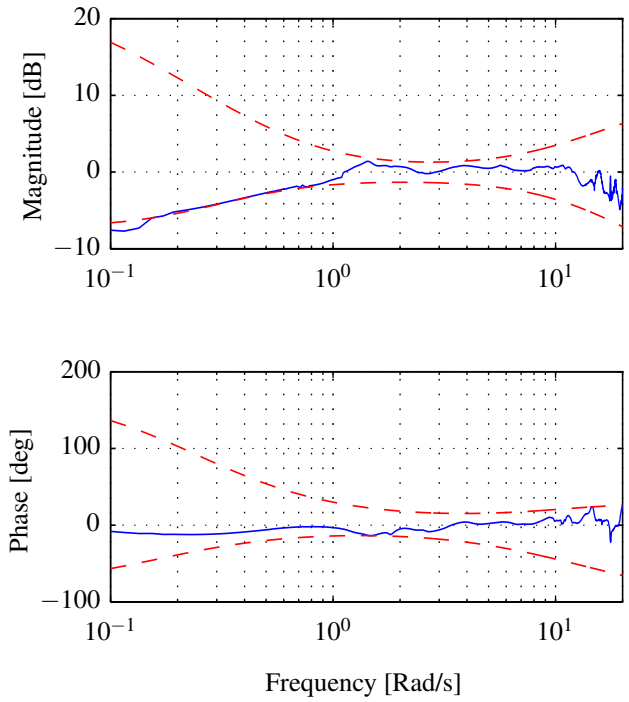

Fig. 11 Error transfer function of the p/δ_{lat} response with MUAD boundaries.

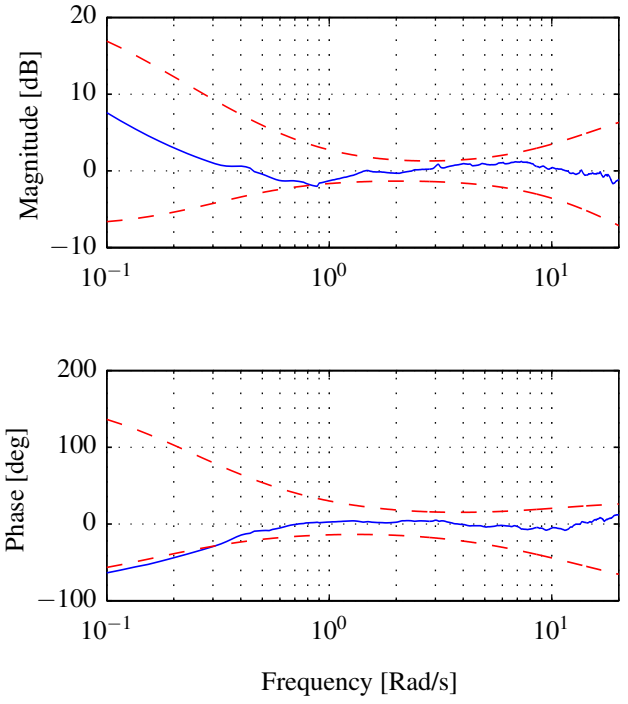

Fig. 13 Error transfer function of the a_z/δ_{col} response with MUAD boundaries.

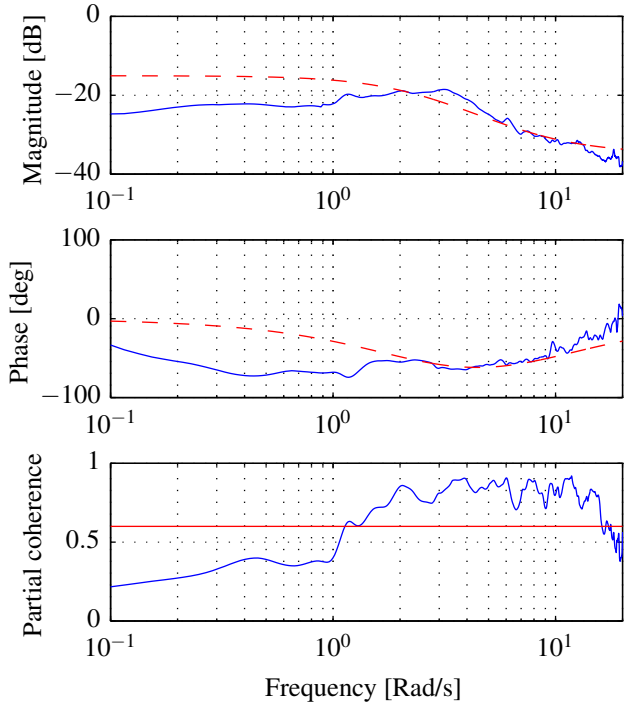

Fig. 14 Transfer function bode plot yaw response r/δ_{ped}. Flight data in continuous line. Model data in dashed line.

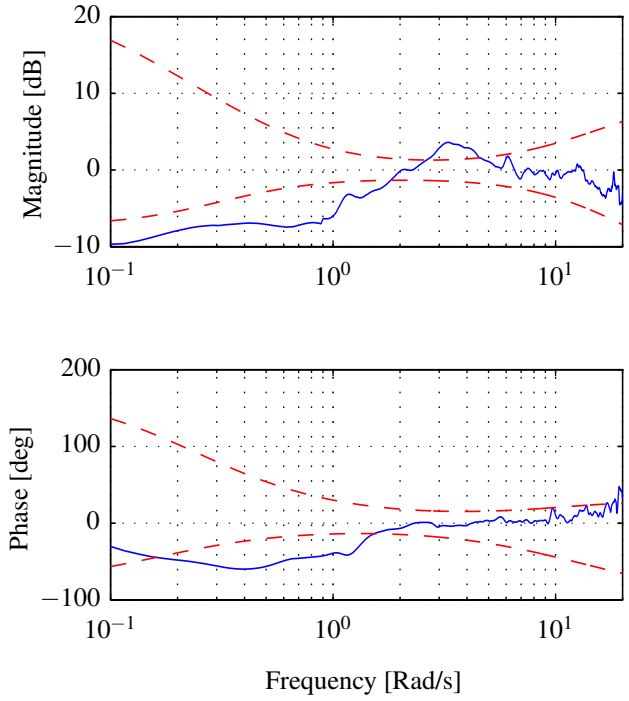

Fig. 15 Error transfer function of the r/δ_{ped} response with MUAD boundaries.

APPENDIX B

The time domain validation results for the main on-axis responses in hover (lateral response p/δ_{lat}, heave response a_z/δ_{col} and yaw response r/δ_{ped}) are shown in Figs 16-18. For the heave a_z/δ_{col} response validation a high frequency pole is added to the transfer function model in Table 2 to ensure physical causality. Different kinds of maneuvers (doublets, steps) are considered from those used during the system identification process (frequency sweeps). As can be noticed in the figures, good level of accuracy is achieved for all the responses.

For the p/δ_{lat} response in Fig. 16 a fit error function is obtained of 0.04 and a Theil Inequality Coefficient (TIC) of 0.045. For the a_z/δ_{col} response in Fig. 17 a fit error function is obtained of 0.05 and a Theil Inequality Coefficient (TIC) of 0.07. For the r/δ_{ped} response in Fig. 18 a fit error function is obtained of 1.8 and a Theil Inequality Coefficient (TIC) of 0.063. These metrics indicate a good level of accuracy.

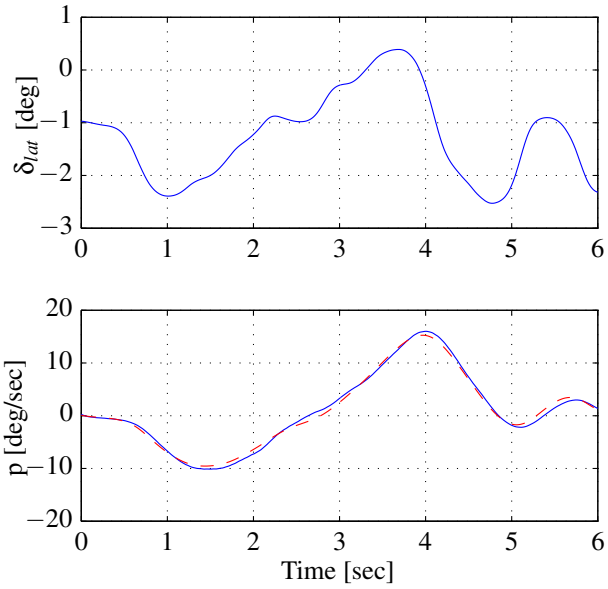

Fig. 16 Time domain verification of the lateral response p/δ_{lat}. Flight data in continuous line. Model data in dashed line.

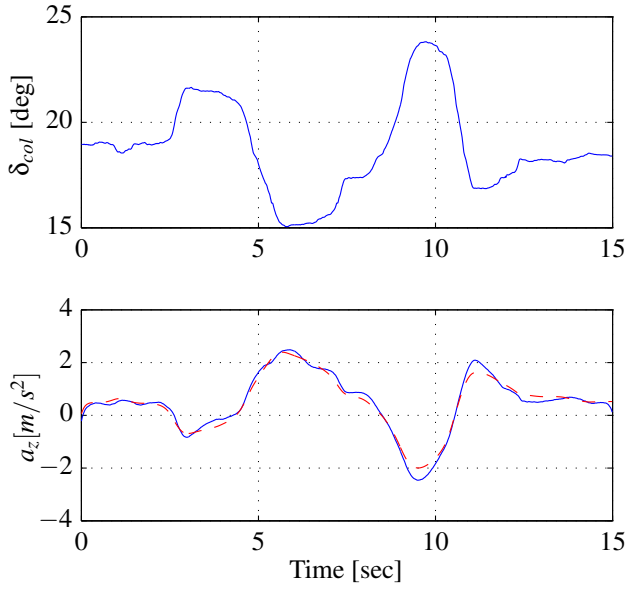

Fig. 17 Time domain verification of the heave response a_z/δ_{col}. Flight data in continuous line. Model data in dashed line.

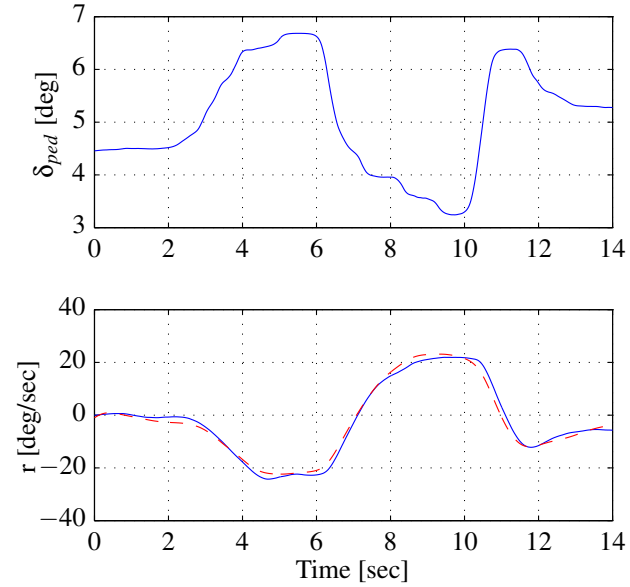

Fig. 18 Time domain verification of the yaw response r/δ_{ped}. Flight data in continuous line. Model data in dashed line.

ACKNOWLEDGMENTS

The work in this paper was partially supported by the myCopter project, funded by the European Commission under the 7th Framework Program.

REFERENCES

[1]Nieuwenhuizen, F. M., Jump, M., Perfect, P., White, M., Padfield, G., Floreano, D., Schill, F., Zufferey, J., Fua, P., Bouabdallah, S., Siegwart, R., Meyer, S., Schippl, J., Decker, M., Gursky, B., Höfinger, M., and Bülthoff, H. H., "myCopter: Enabling Technologies for Personal Aerial Transportation Systems," Proceedings of the 3rd International HELI World Conference, Frankfurt/Main, 2011.

[2]Schroeder, J. A., Tischler, M. B., Watson, D. C., and Eshow, M. M., "Identification and Simulation Evaluation of a Combat Helicopter in Hover," *Journal of Guidance, Control, and Dynamics*, Vol. 18, (1), January-February 1995, pp. 31–38.

[3]Fletcher, J. W., "Identification of UH-60 Stability Derivative Models in Hover from Flight Test Data," *Journal of the American Helicopter Society*, Vol. 40, (1), 1995, pp. 32–46.

[4]"AGARD Lecture Series 178, Rotorcraft System Identification," Technical report, AGARD Advisory Group for Aerospace Research & Development, 7 Rue Ancelle, 92200 Neuilly Sur Seine, France, 1995.

[5]Williams, J. N., Ham, J. A., and Tischler, M. B., "Flight Test Manual, Rotorcraft Frequency Domain Flight Testing," Technical report, US Army Aviation Technical Test Center, Edwards AFB, CA, AQTD Project, No. 93-14, 1995.

[6]Hamel, P. G. and Kaletka, J., "Advances in rotorcraft system identification," *Progress in Aerospace Sciences*, Vol. 33, March-April 1997, pp. 259–284.

[7]Ivler, C. and Tischler, M., "Case Studies of System Identification Modeling for Flight Control Design," *Journal of the American Helicopter Society*, Vol. 58, (1), January 2013, pp. 1–16.

[8]Tischler, M. B., "System Identification Requirements for High-Bandwidth Rotorcraft Flight Control System Design," Procceding of the American Control Conference, 1991.

[9]Chen, R. T. N. and Hindson, W. S., "Influence of Higher-Order Dynamics on Helicopter Flight Control System Band-width," *Journal of Guidance, Control, and Dynamics*, Vol. 9, (2), 1986, pp. 190–197.

[10]Greiser, S. and Lantzsch, R., "Equivalent Modelling and Suppression of Air Resonance for the ACT/FHS in Flight," Proceedings of the 39th European Rotorcraft Forum 2013, Moscow, 2013.

[11]Geluardi, S., Nieuwenhuizen, F. M., Pollini, L., and Bülthoff, H. H., "Data collection for developing a dynamic model of a light helicopter," Proceedings of the 39th European Rotorcraft Forum 2013, Moscow, 2013.

[12]Hamel, P. G. and Jategaonkar, R. V., "Evolution of Flight Vehicle System Identification," *Journal of Aircraft*, Vol. 33, (1), January-February 1996, pp. 9–28.

[13]Tischler, M. B. and Remple, R. K., *Aircraft and Rotorcraft System Identification Engineering Methods with Flight Test Examples*, AIAA Education Series, 2012.

[14]Fletcher, J. W., "A Model Structure for Identification of Linear Models of the UH-60 Helicopter in Hover and Forward Flight," Technical report 95-a-008, NASA Technical Memorandum 110362 USAATCOM, 1995.

[15]Bendat, J. S. and Piersol, A. G., *Random Data: Analysis and Measurement Procedures, Fourth Edition*, John Wiley & Sons, 2010.

[16]Sahai, R., Cicolani, L., Tischler, M., Blanken, C., Sullivan, C., Wei, M., Ng, Y.-S., and Pierce, L., "Flight-time identification of helicopter-slung load frequency response characteristics using CIFER," Proceedings of the 24th Atmospheric Flight Mechanics Conference, August 1999.

[17]Tischler, M. B. and Cauffman, M. G., "Frequency Response Method for Rotorcraft System Identification: Flight Applications to BO 105 Coupled Rotor/Fuselage Dynamics," *Journal of the American Helicopter Society*, Vol. 37, (3), July 1992, pp. 3–17.

[18]Ham, J. A., Gardner, C. K., and Tischler, M. B., "Flight Testing and Frequency Domain Analysis for Rotorcraft Handling Qualities," *Journal of the American Helicopter Society*, Vol. 40, (2), April 1995, pp. 28–38.

[19]Tischler, M. B., "System Identification Methods for Aircraft Flight Control Development and Validation," Technical Report NASA-TM-110369, Aeroflightdynamics Directorate, U.S. Army ATCOM, Ames Research Center, Moffett Field, CA 94035-10008, October 1995.

[20]Cicolani, L., McCoy, A. H., Sahai, R., Tyson, P. H., Tischler, M. B., Rosen, A., and Tucker, G. E., "Flight Test Identification and Simulation of a UH60A Helicopter and Slung Load," *Journal of the American Helicopter Society*, Vol. 46, (2), April 2001, pp. 140–160.

[21]Heffley, R. K., "A Compilation and Analysis of Helicopter Handling Quality Data," Technical Report NASA-CR-314, National Aeronautics and Space Administration, Scientific and Technical Information Branch, 1979.

[22]Jategaonkar, R. V., Fischenberg, D., and Gruenhagen, W., "Aerodynamic Modeling and System Identification from Flight Data-Recent Applications at DLR," *Journal of Aircraft*, Vol. 41, (4), 2004, pp. 681–691.

10. Non-linear helicopter model

This paper was published and presented at the European Rotorcraft Forum:

C. A. Gerboni, S. Geluardi, M. Olivari, F. M. Nieuwenhuizen, H. H. Bülthoff and L. Pollini (2014) **Development of a 6 DoF nonlinear helicopter model for the MPI Cybermotion Simulator** *40th European Rotorcraft Forum (ERF 2014)*, 1-12.

Abstract

This paper describes the different phases of realizing and validating a helicopter model for the MPI CyberMotion Simulator (CMS). The considered helicopter is a UH-60 Black Hawk. The helicopter model was developed based on equations and parameters available in literature. First, the validity of the model was assessed by performing tests based on ADS-33E-PRF criteria using closed loop controllers and with a non-expert pilot. Results on simulated data were similar to results obtained with the real helicopter. Second, the validity of the model was assessed with a helicopter pilot in-the-loop in both a fixed-base simulator and the CMS. The pilot performed a vertical remask maneuver defined in ADS-33E-PRF. Most metrics for performance were reached adequately with both simulators. The motion cues in the CMS allowed for improvements in some of the metrics. The pilot was also asked to give a subjective evaluation of the model by answering the Israel Aircraft Industries Pilot Rating Scale (IAI PRS). Similarly to results of ADS-33E-PRF, pilot responses confirmed that the motion cues provided more realistic flight experience.

DEVELOPMENT OF A 6 DOF NONLINEAR HELICOPTER MODEL FOR THE MPI CYBERMOTION SIMULATOR

Carlo A. Gerboni, [1,2] Stefano Geluardi, [1,2] Mario Olivari, [1,2] Frank M. Nieuwenhuizen, [1]
Heinrich H. Bülthoff, [1] and Lorenzo Pollini [2]

[1] *Max Planck Institute for Biological Cybernetics*
Spemannstrasse 38, 72076 Tübingen
Germany
[2] *University of Pisa*
Via Diotisalvi 2, 56122 Pisa
Italy
Email: {carlo.gerboni; stefano.geluardi; mario.olivari}@tuebingen.mpg.de
{frank.nieuwenhuizen; heinrich.buelthoff}@tuebingen.mpg.de
lpollini@dsea.unipi.it

Abstract

This paper describes the different phases of realizing and validating a helicopter model for the MPI CyberMotion Simulator (CMS). The considered helicopter is a UH-60 Black Hawk. The helicopter model was developed based on equations and parameters available in literature. First, the validity of the model was assessed by performing tests based on ADS-33E-PRF criteria using closed loop controllers and with a non-expert pilot. Results on simulated data were similar to results obtained with the real helicopter. Second, the validity of the model was assessed with a helicopter pilot in-the-loop in both a fixed-base simulator and the CMS. The pilot performed a vertical remask maneuver defined in ADS-33E-PRF. Most metrics for performance were reached adequately with both simulators. The motion cues in the CMS allowed for improvements in some of the metrics. The pilot was also asked to give a subjective evaluation of the model by answering the Israel Aircraft Industries Pilot Rating Scale (IAI PRS). Similarly to results of ADS-33E-PRF, pilot responses confirmed that the motion cues provided more realistic flight experience.

NOTATION

a_0	main rotor blade lift curve slope $(1/rad)$
s	rotor solidity (-)
u, v, w	translational velocity components of helicopter along fuselage *x-,y-,z-*axes (m/s)
p, q, r	angular velocity components of helicopter along fuselage *x-,y-,z-*axes (rad/s)
p_w, q_w, r_w	angular velocity components of helicopter in hub axes (rad/s). With a bar they are normalized by Ω
k_1, k_2, k_3, k_4	augmentation system parameters (-)
C_T	rotor thrust coefficient (-)
I_{xx}, I_{yy}, I_{zz}	moments of inertia of the helicopter about the x-,y-,z-axes $(kg\ m^2)$
M_a	helicopter mass (kg)
R	main rotor radius (m)
S_E	area of the empennage components (fin or tail plane) or of the fuselage (m^2)

T	main rotor thrust (N)
V	forward velocity (m/s)
V_E	total velocity incident on empennage components (on fin or on tail plane) or on fuselage (m/s)
θ, ϕ, ψ	Euler angles defining the orientation of the aircraft relative to the Earth (rad)
$\beta_0, \beta_{1c}, \beta_{1s}$	rotor blade coning, longitudinal and lateral flapping angles (rad)
β_{1cw}, β_{1sw}	longitudinal and lateral pitch angle in hub axes (rad)
$\lambda_0, \lambda_{1c}, \lambda_{1s}$	rotor uniform and first harmonic inflow velocities (normalized by ΩR)
θ_0	collective pitch angle (rad)
θ_{1c}, θ_{1s}	lateral and longitudinal pitch angle (rad)
$\theta_{1cw}, \theta_{1sw}$	lateral and longitudinal pitch angle in hub axes (rad)
θ_{0T}	tail rotor collective pitch angle (rad)
θ_{tw}	main rotor blade linear twist (rad)
$\eta_0, \eta_{1c}, \eta_{1s}$	collective lever and cyclic stick position (normalized by the stick deflection range)
γ	Lock number $(-)$
ρ	air density (kg/m^3)
μ	advance ratio (V/(ΩR))
μ_z	velocity of the rotor hub in hub/shaft axes (normalized by ΩR)
Ω	main rotor speed (rad/s)

1. INTRODUCTION

An investigation on how to make a Personal Air Vehicle (PAV) as easy to fly as driving a car is currently conducted at the Max Planck Institute for Biological Cybernetics, under the myCopter EU funded research program.[1] In these studies, rotorcraft vehicles are considered as the main reference since their dynamics and kinematics best reflect those of a PAV. A key facility that is essential for these studies is the MPI's Cybermotion Simulator (CMS) shown in Figure 1. The CMS is an anthropomorphic robot with eight degrees of freedom and a cabin as end-effector capable of hosting a person. The cabin is equipped with a stereo projection system. A 10 meters linear track allows to increase the workspace of the robot. Different vehicle dynamics models can be simulated in its large motion envelope.

So far, experiments related to helicopter models were already performed on the CMS but only with simplified dynamics.[2] However, recent studies at the MPI led to considering implementing a more complex and realistic helicopter model. These studies consist of the development of new human-machine interface technologies, [3] investigation of pilots behavior, training of non-expert pilots, implementation of new control systems to be tested in simulation with human in-the-loop and training of pilots for performing specific maneuvers for system identification purposes.[4] Therefore, it was decided to implement a full-flight nonlinear dynamic helicopter model to be used in the CMS.

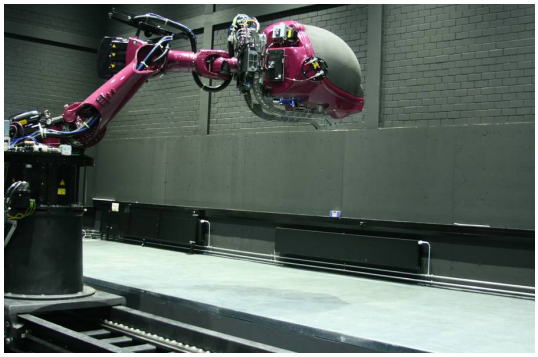

Figure 1: The 8 DoF MPI CyberMotion Simulator (http://www.cyberneum.de/).

Nonlinear models for unmanned small-size helicopters have been investigated and tested in literature.[5] On the contrary, nonlinear models for full-size helicopters are not very common, due to the difficulty of accurately implementing the components of the vehicle and obtaining reliable aerodynamic parameters. Few nonlinear helicopter models have been developed and tested in motion simulators but they are not readily available.[6, 7]

This paper presents the main steps considered for developing a mathematical helicopter model for use in the CMS. The complexity of the implemented model and the large motion envelope of the simulator should allow for simulating highly realistic flight scenarios. As first step, the model was implemented and validated by performing several test maneuvers with the help of closed-loop controllers. After that, a helicopter pilot

was asked to evaluate the model in a fixed-base simulator. Finally, the same pilot evaluated the model in the CMS.

The paper is organized as follows: Section 2 describes the development of the model. Section 3 presents the results of the time and frequency domain analysis done on the model. Section 4 is dedicated to the experiments with the helicopter pilot in the fixed-base simulator and in the CMS. Finally, future steps are summarized.

2. MODEL DEVELOPMENT

A 6 Degrees of Freedom (DoF) nonlinear mathematical model was built based on generic helicopter dynamics equations.[8] As shown in Figure 2, the helicopter model is composed of five subsystems that represent the main helicopter components: the main rotor, the tail rotor, the fuselage, the empennage and the transfer functions from the pilot input to the blades of the two rotors (flight control system). The main rotor speed was assumed constant. In addition, the reaction of the ground was modeled as a mass-spring-damper system.

The outputs of every subsystem are forces and torques in body frame of reference, from which linear and rotational accelerations are obtained. Then, the Euler angles are calculated to define the attitude of the helicopter.

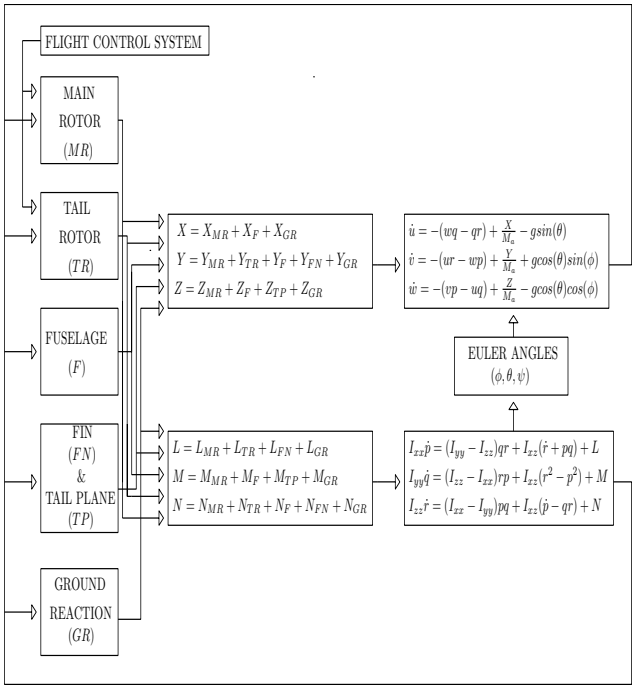

Figure 2: Block diagram of the helicopter model and reaction of the ground

The resulting dynamic system has the form

$$\dot{\mathbf{x}} = \mathbf{F}\{\mathbf{x}, \mathbf{u}, t\} \tag{1}$$

where the state vector **x** has the following elements:

$$\mathbf{x} = \{\mathbf{x}_f, \mathbf{x}_r, \mathbf{x}_b\} \tag{2}$$

in which the subscripts *f, r, b* refer to the fuselage, the rotors and the blades, respectively. The components of the states $\mathbf{x}_f$, $\mathbf{x}_r$ and $\mathbf{x}_c$ are:

$$\mathbf{x}_f = \{u, v, w, p, q, r, \phi, \theta, \psi\} \tag{3}$$
$$\mathbf{x}_r = \{\beta_0, \beta_{1c}, \beta_{1s}, \lambda_0, \lambda_{1c}, \lambda_{1s}\} \tag{4}$$
$$\mathbf{x}_c = \{\theta_0, \theta_{1c}, \theta_{1s}, \theta_{0T}\} \tag{5}$$

with all the components defined in the nomenclature. The vector **u** represents the pilot inputs:

$$\mathbf{u} = \{\eta_0, \eta_{1s}, \eta_{1c}, \eta_{0T}\} \tag{6}$$

where η_0 is the *collective* lever displacement, η_{1s} the *longitudinal cyclic* stick, η_{1c} is the *lateral cyclic* stick and η_{0T} is the displacement of the *pedals*.
The helicopter chosen for this work is the UH-60 Black Hawk because it is one of the most described in literature. The mechanical, dynamic and aerodynamic parameters were mainly taken from two sources.[9, 10] The dynamic equations of the model are not repeated here as they are described in detail in literature.[8] Only several aspects of the model implementation that received particular attention are detailed in the following sections.

2.1. Rotors

Two main parameters of the main and the tail rotor are the *thrust coefficient* C_T and the *total inflow* λ_0 passing through the blades. We employed a rather complete model that, although valid only at steady state, can model several aerodynamic effects. The thrust coefficient and the total inflow equations are:

$$\begin{aligned} C_T &= \frac{a_0 s}{2}\left(\theta_0\left(\frac{1}{3} + \frac{\mu^2}{2}\right)\right) \\ &+ \frac{a_0 s}{2}\left(\frac{\mu}{2}\left(\theta_{1sw} + \frac{\bar{p}_w}{2}\right)\right) \\ &+ \frac{a_0 s}{2}\left(\frac{\mu_z - \lambda_0}{2}\right) + \frac{a_0 s}{2}\left(\frac{1}{4}(1+\mu^2)\theta_{tw}\right) \end{aligned} \tag{7}$$

$$\lambda_0 = \frac{C_T}{2\sqrt{[\mu^2 + (\lambda_0 - \mu_z)^2]}} \tag{8}$$

The two parameters C_T and λ_0 depend on each other; this makes computing the flight condition complex. Different approaches have been proposed to calculate the solution of equations 7 and 8. For instance, a closed-form solution for C_T and λ_0 can be found for each specific flight condition (take off, hover, forward flight and landing).[8] However, this approach implies switching between different sets of equations when simulating the model in different steady states. Hence, an iterative solution based on a Newton-Rhapson method was applied to arrive at a model that is valid in all flight conditions.
Another issue we encountered during the development was the relation between the blade pitch angles and the displacement of the swashplate. Different models [8, 12, 13] were tested in order to find the relationship that better approximate the response of the real helicopter.[14] Best accuracy was obtained with a method that reduce much the effect of the blade linear twist θ_{tw}, that in helicopter like the UH-60 has an important influence due to its big value:[13]

$$\beta_0 = \gamma \left[\frac{\theta_0}{8}(1+\mu^2) + \frac{\theta_{tw}}{10}(1+\frac{5}{6}\mu^2) + \frac{\mu}{6}\theta_{1sw} - \frac{\lambda_0}{6} \right] \quad (9)$$

$$\beta_{1sw} = \theta_{1cw} + \frac{(-\frac{4}{3}\mu\beta_0)}{(1+\frac{1}{2}\mu^2)} \quad (10)$$

$$\beta_{1cw} = -\theta_{1sw} + \frac{-\frac{8}{3}\mu[\theta_0 - \frac{3}{4}\lambda_0 + \frac{3}{4}\mu\theta_{1sw} + \frac{3}{4}\theta_{tw}]}{1-\frac{1}{2}\mu^2} \quad (11)$$

2.2. Aerodynamics of fuselage and empennage

Aerodynamic equations for fuselage and empennage generally change between different steady states and different helicopters. Data from wind tunnel tests in each steady state are necessary for describing the evolution of these equations. Our approach consisted of implementing generic equations that could also be used for other helicopters than the UH-60 considered in this paper. The generic equations for drag is given as:

$$\frac{1}{2}\rho V_E^2 S_E C_{E_{friction}} \quad (E \in \{fin, tailplane, fuselage\}) \quad (12)$$

The *friction coefficient* $C_{E_{friction}}$ is defined differently for the fuselage and for the empennage. For the fuselage it is derived from table look-up functions made with generalized aerodynamic coefficients.[8] For the empennage it is defined as

$$C_{E_{friction}} = \begin{cases} ksin(\alpha) & : |C_{friction}| < \delta \\ -\delta * sgn(sin(\alpha)) & : |C_{friction}| > \delta \end{cases} \quad (13)$$

in which α is the angle of incidence of the air with the tail plane and with the fin. In this model, the limit factor δ and the scaling factor *k* are taken by approximated wind tunnel equations of the empennage.[9, 10] This was done for this helicopter because a detailed report is present in literature.[10] However, these variables can also be tuned manually or with the help of an experienced pilot.

2.3. Stability Augmentation System

The model input vector is composed of the four controls (collective, lateral and longitudinal cyclic and pedals). The pilot changes the blade pitch described in (5) by moving the controls.

The UH-60 features a *Stability Augmentation System* (SAS) that is used to aid the pilot. We only considered such a system for the cyclic controls, as these are considered most difficult to use. The transfer functions that connect the cyclic input of the pilot with the main rotor blade pitch are

$$\theta_{1c} = \frac{(a_1\eta_{1c} + b_1) + k_1 p + k_2 \phi}{1+\tau s} \quad (14)$$

$$\theta_{1s} = \frac{(a_2\eta_{1s} + b_2) + k_3 q + k_4 \theta}{1+\tau s} \quad (15)$$

In which (a_1, a_2) and (b_1, b_2) define the angular ranges for θ_{1c} and θ_{1s}. (k_1, k_2, k_3, k_4) are the parameters of the SAS. The SAS parameters are tuned to obtain frequency responses similar to the real helicopter as it was active during all the tests.[15] At the same time the contribution of the SAS is saturated in such a way that physical limits of the blades are not exceeded.

3. VALIDATION WITH CLOSED-LOOP CONTROLLERS

This section presents validation tests performed with closed-loop controllers such that the tests can be performed without an experienced pilot. Different analyses were performed that cover different aspects of a helicopter model. Two tests will be presented that were performed in the time and frequency domain. The results were compared with flight test data from literature. All simulations were done with MATLAB/Simulink and a basic virtual environment

developed in Unity3D.

By definition the *Aeronautical Design Standard* (ADS-33E-PRF) defines the *desired Handling Qualities for military helicopters*.[16] The ADS-33E-PRF tests can be divided in two groups: quantitative tests and MTEs (*Mission Task Elements*). The quantitative tests requires giving a specific input (i.e. steps and sweeping sinusoids) and evaluating the responses of the rotorcraft in the time and frequency domain. MTEs are composed of specific maneuvers that a pilot needs to accomplish while respecting some performance metrics. This section describes the quantitative tests while the MTEs are detailed in Section 4.

3.1. Helicopter in hover with controllers

To control the helicopter in hover condition, controllers were designed as *Proportional*, *Integral*, *Derivative* (PID) regulators. These controllers regulated the actual speed of the rotorcraft to a reference value by controlling the blade pitch angles. For the hover condition, all the reference velocities were set to zero. Table 1 presents the blade pitch of the model compared with results from flight tests.[14] The comparison shows that the collective and the longitudinal pitch are almost the same while the lateral pitch has a little difference. From this first simulation, it was shown that trimming the model in hover resulted in similar responses of the blades compared to a flight test.

Table 1: Blade pitch angles in hover (angles are given in degrees)

	Flight test[14]	Model
θ_0	$\simeq 8$	$\simeq 8$
θ_{1c}	$\simeq 3.5$	$\simeq 1.5$
θ_{1s}	$\simeq -3.5$	$\simeq -3$

3.2. Attitude quickness test

The first quantitative test is the *attitude quickness response*. The aim of this test is to study the quickness of the rotorcraft at changing its attitude in response to a step input. The evaluated metrics are

$$roll\ attitude\ quickness = \frac{p_{pk}}{\Delta_\phi} \tag{16}$$

$$pitch\ attitude\ quickness = \frac{q_{pk}}{\Delta_\theta} \tag{17}$$

The parameters $p_{pk}, q_{pk}, \Delta_\phi$ and Δ_θ are highlighted in Figure 3.

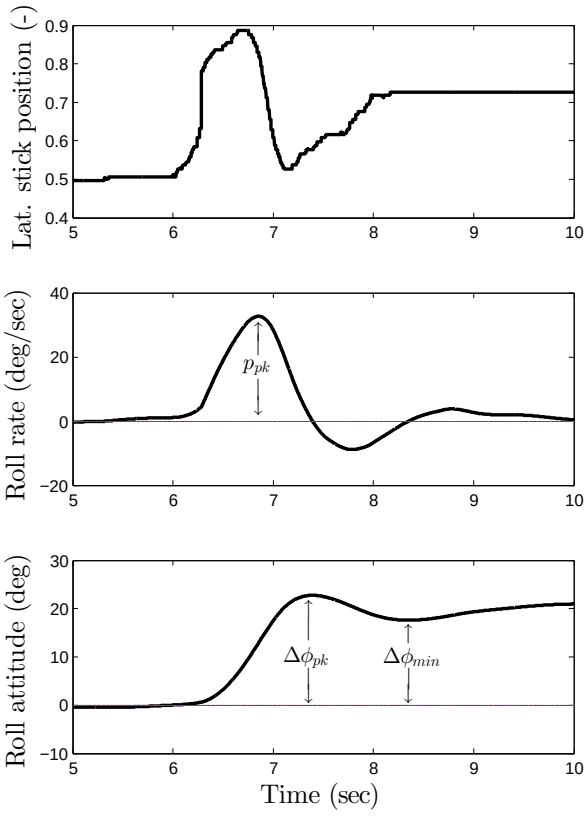

Figure 3: Lateral cyclic input for roll attitude quickness. Parameters involved in the test are highlighted. The range of the cyclic stick is between 0 and 1

To compare results of our model with those obtained with a real helicopter, we replicated the same pilot input [15] with a joystick to have a left and right roll, and a forward and backward pitch while controlling the other axes in hover with the PID controllers. The small duration of the input and the use of the PID controllers for the other axes allowed performing this task without an experienced pilot.

Figure 4 and 5 show the results of the attitude quickness test compared with real data.[15] The quickness of the model with respect to the data of a flight test is almost identical. This shows that the model reaches Level 1 Handling Qualities.

3.3. Frequency response analysis

The second analysis performed is based on the frequency response of the system. The main parameters of interest are the bandwidth of the system and the phase delay. The first parameter is defined by the frequency at which the phase is 135° while the phase delay is

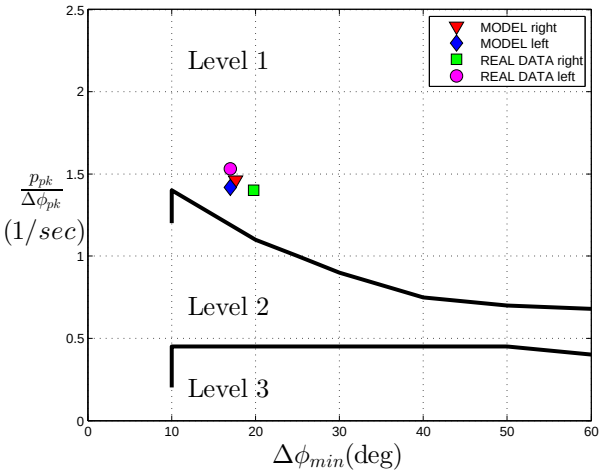

Figure 4: Roll attitude quickness test

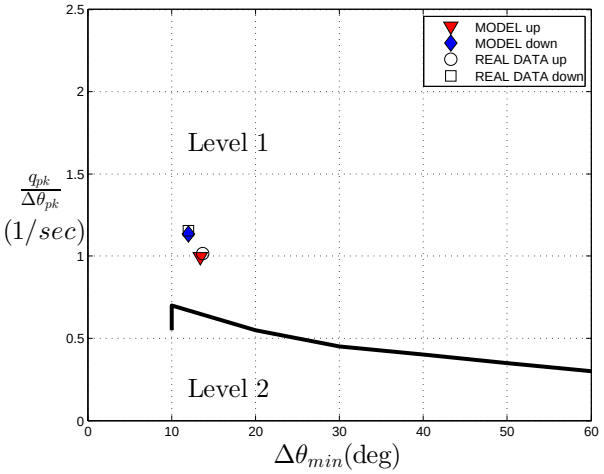

Figure 5: Pitch attitude quickness test

(18) $$\tau_p = \frac{\Delta\Phi_{2\omega_{180}}}{57.3 \times 2\omega_{180}}$$

in which $2\omega_{180}$ indicates two times the frequency at which the phase is 180° while $\Delta\Phi_{2\omega_{180}}$ is the phase difference between ω_{180} and $2\omega_{180}$.[8] At the Max Planck Institute for Biological Cybernetics studies of rotorcraft identification are conducted [17] based on a method developed in literature.[18] Using this work, the frequency responses of the model were obtained for the roll, pitch and yaw degrees of freedom with the helicopter in hover. A small amplitude sweeping sinusoid signal was given as input for the DoF of interest and the corresponding Euler angle was considered as output. The Bode diagrams for roll, pitch and yaw are shown in Figure 6, in Figure 7 and in Figure 8, respectively and the parameters required for equation 18 are highlighted.

The phase delay results are given in Figures 9, 10 and 11. Two different observations can be made from

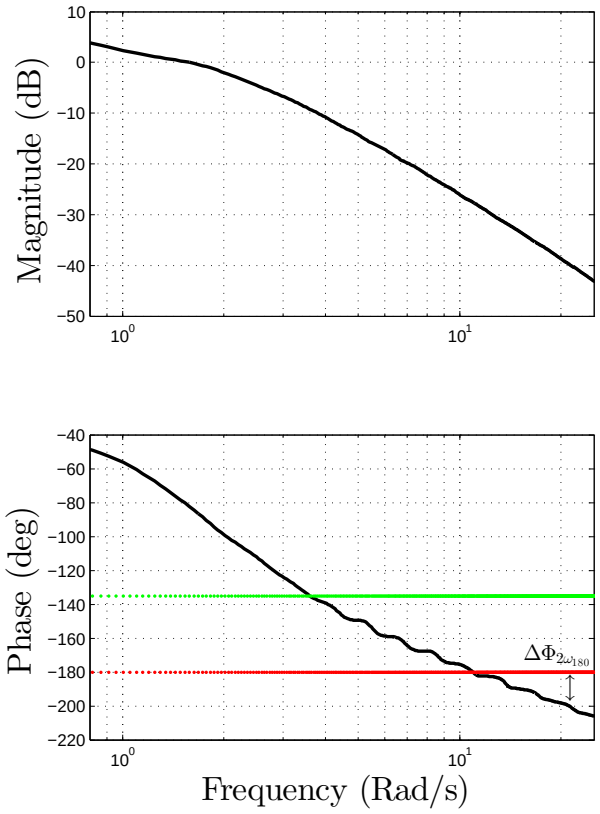

Figure 6: Bode diagram for the roll channel

the results: the bandwidth of the identified system is almost the same of the real vehicle for all three channels. However, the roll and pitch responses show a different phase delay caused by a smaller $\Delta\Phi_{2\omega_{180}}$ of the model compared with the real system at high frequencies. The causes for this effect are currently under investigation.

4. VALIDATION WITH A HELICOPTER PILOT

The tests described in the previous section showed the similarity of the model with the real helicopter. In the second step, the model was tested with a helicopter pilot. The tests were done in fixed-base simulator and a motion simulator. The same maneuver was performed in both simulators. The pilot was instructed maintain the performance levels defined in the ADS-33E-PRF criteria as best as possible during the maneuver task.

4.1. Experimental setups

The first evaluation with the pilot was executed in a fixed-base simulator. The simulation was executed with a real-time pc. A complex virtual environment

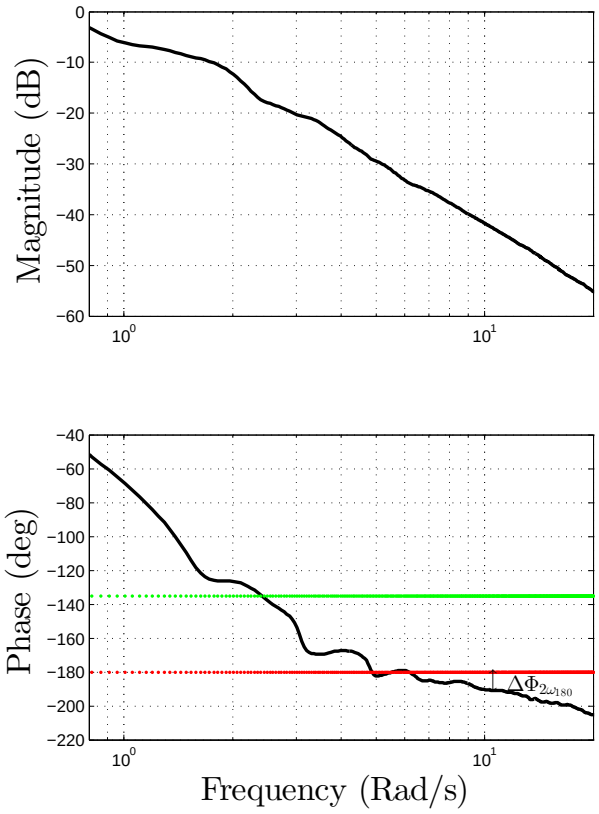

Figure 7: Bode diagram for the pitch channel

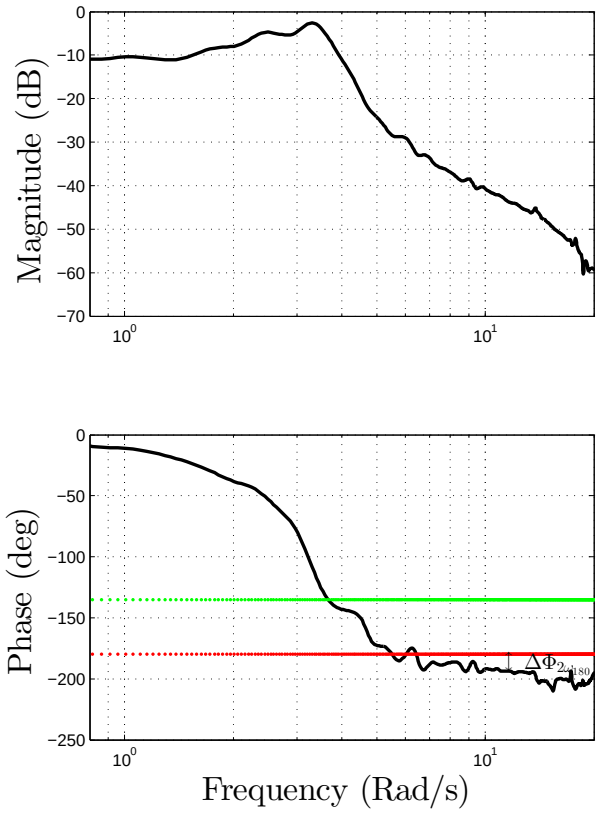

Figure 8: Bode diagram for the yaw channel

was developed in Unity3D, which was composed of an airport with markers that were required to execute the maneuver. A control-loaded cyclic stick, collective level and pedals were used (Wittenstein GmbH, Germany), see Figure 12.

The experiment was performed with a screen with a field of view of 230 deg horizontal and 125 deg vertical, see Figure 13.

The second evaluation was performed in the MPI CyberMotion Simulator (CMS), see Figure 1. This simulator is a 8 DoF serial anthropomorphic robot with an enclosed cabin. The same control-loaded input devices were used as in the fixed-base simulator and the same virtual environment was shown to the pilot. The linear accelerations and rotational velocities from the model were scaled by multiplication with factors between 0.01 and 0.9. Washout filters are not used. The scaling was relatively strong as the main purpose of this test was to validate the model, and not to optimize the motion cues presented to the pilot.

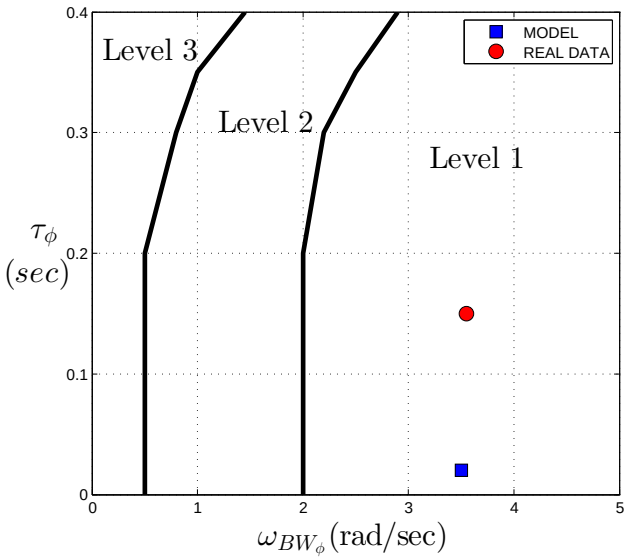

Figure 9: Roll frequency response analysis

4.2. Description of the task

The evaluation was divided in two sequential parts. The first part was executed only in the Panolab while the second was executed in both simulators. In the first part the pilot tested four different flight conditions to rate the responses of the model. In the second part he performed a specific ADS-33E-PRF MTE.

The virtual environment used for both parts is shown in Figure 14. Three squares in the ground, a bar

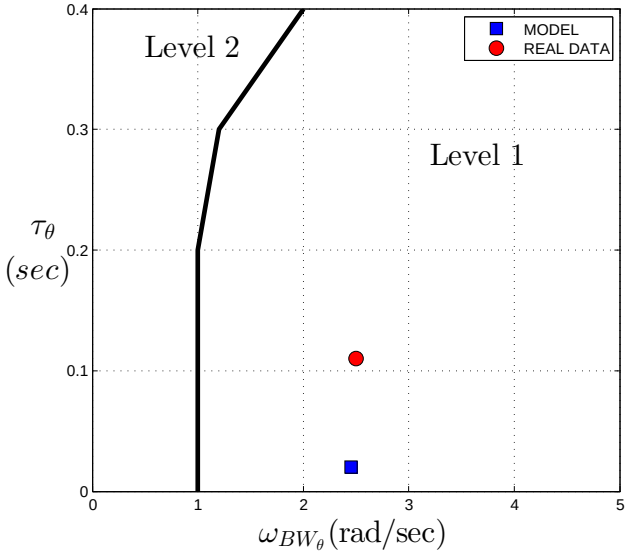

Figure 10: Pitch frequency response analysis

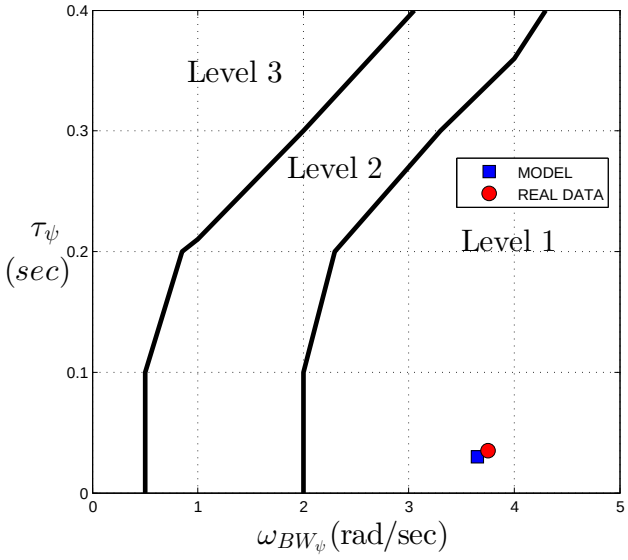

Figure 11: Yaw frequency response analysis

with two spheres in the starting position and different markers between the squares are present in the environment. These elements are collocated in such a way different MTEs can be executed and the markers limit the displacements allowed to consider the required performances reached.

The goal of the first part was to check all the 6 DoF of the rotorcraft using all the four inputs. This means that in this phase no attention was paid in execution time and to distance from the markers position.

In details the four maneuvers were:

1. Take-off along the bar shown in Figure 14 and hover in front of the higher sphere. Subsequently a vertical descent and a new hover in front of the lower sphere.
2. A right lateral displacement from the starting square on the ground to the second square and

Figure 12: Control loaded cyclic stick, collective lever and pedals used in the experiments

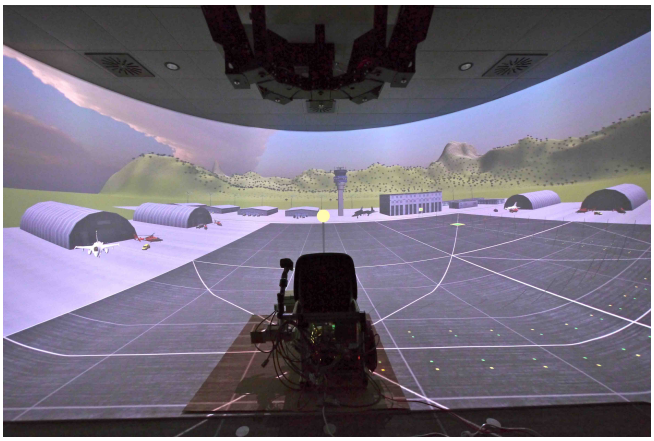

Figure 13: Experimental setup (http://www.cyberneum.de/research-facilities/panolab)

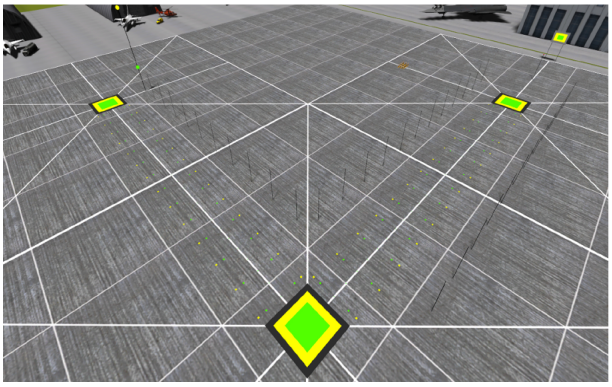

Figure 14: Unity3D visualization used for the simulator evaluations. The starting position is on the leftmost.

back again.

3. Forward flight from the second square to the third and back again.
4. A 360° turn around the bar.

After each maneuver, the pilot rating scale (PRS) was used by the pilot to assess the model. This PRS asks the pilot to evaluate the primary response and the secondary response of each executed maneuver. As an example, for the maneuver 1, the primary response is given by the use of the collective for the vertical movement, while the secondary response is the compensatory action that the pilot does with the pedals to counteract the yaw motion. In addition he is asked to rate the difficulties in executing the maneuver in relation to the response of the model and with the visualization.

The second part is the execution of a specific MTE.[16] The maneuver chosen is the vertical remask. This maneuver is composed of three parts:

1. The maneuver starts with a vertical remask from a stabilized hover at 75 ft to an altitude of 35 ft (slightly modified from the original maneuver [16])
2. Lateral displacement of 300 ft
3. Stabilize in a new hover position

This maneuver was chosen for several reasons. First of all it covers different flight conditions: the initial take off to reach the first hover position where the maneuver starts, the vertical descent and the fast lateral displacement. Second with this maneuver it is possible to use all the inputs of the system: the pedals are used to counteract turns during the displacement, the lateral cyclic for the lateral displacement, the longitudinal cyclic for maintaining the longitudinal position and the collective to maintain altitude. Third, with the lateral displacement is possible to exploit the linear track of the CMS for a more realistic reproduction of lateral accelerations. The markers placed in the environment indicate the adequate or desired performance as defined in ADS-33E-PRF for both conditions.

The pilot that performed the test has experience with real helicopters and with simulators. He has about 110 flight hours with around 700 take offs and landings. For the simulators he flew a Bell UH-1D in different sessions.

4.3. Dependent measures

As the nonlinear dynamic helicopter model described in this paper is intended to be used to investigate pilots behavior, to record data for system identification purposes and to test new control systems to use with human in-the-loop, it is necessary to show that the model can be used to perform complex tasks. Therefore, more attention was given to some of the metrics as defined in ADS-33E-PRF [16] because they are independent from possible visualization difficulties. These metrics are

1. Maintain altitude after remask and during displacement within +10 ft and -15 ft ($\pm$ 10 ft to be desired)
2. Maintain heading within $\pm$ 15 deg (10 deg to be desired)
3. Achieve the final stabilized hover within 25 sec of initiating the maneuver (15 sec to be desired)

4.4. Results

The *Israel Aircraft Industries Pilot Rating Scale* (IAI PRS),[18] rates the primary and the secondary helicopter responses with a scale from 0 to 6. In this scale 0 means that the response cannot be evaluated while 6 means an exact match of the model response with the real helicopter. The difficulty of execution scale, which includes the stability characteristics dissimilarities and the simulation difficulties, ranges from 0 to 5 where again 0 means that is not possible to evaluate and 5 that there is an exact matching. Table 2 shows the ratings given by the pilot.

Table 2: Pilot evaluation

	Prim. res.	Sec. res.	Difficulty of exec.
$Man.1$	3.6	3.5	3.5
$Man.2$	3	3.5	2.5
$Man.3$	3.8	3.8	2.5
$Man.4$	4	4	4

Apart from the ratings, verbal comments of the pilot were recorded:

"*Optimal coupling between collective and pedals*"

"*The lack of motion makes it difficult to maintain altitude during lateral or longitudinal displacement*"

"*The overall evaluation is very good.*"

A consideration from the pilot's remarks was that the lack of motion made it difficult to fly the helicopter model. The main problem was to maintain altitude due to the fact that in the real helicopter the pilot

"feels" the movement more than he can see the movement. So we expected an improvement of the performance with a motion simulator. Table 3 shows performances reached for both simulators:

Table 3: Performances in the two simulators

	Panolab	CMS
$Metric\ 1$	$Adequate$	$Desired$
$Metric\ 2$	$Desired$	$Desired$
$Metric\ 3$	$NotReached$	$NotReached$

As expected there was an improvement of the first metric. Figure 15 highlights the vertical position during lateral displacement.

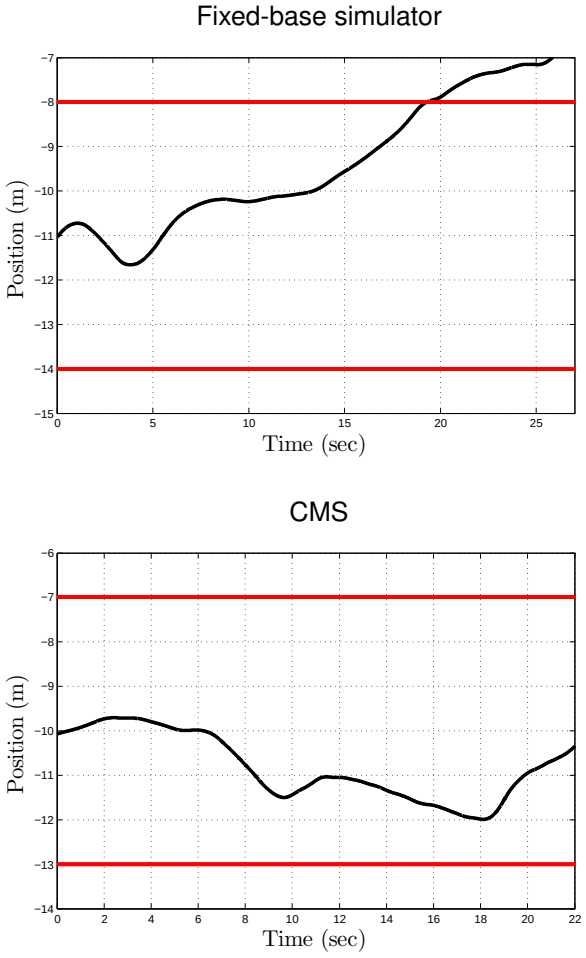

Figure 15: Vertical position in the two simulators during lateral displacement

The first problem caused by the lack of motion in the fixed-base simulator was the difficult to stop the vertical descend in front of the lower sphere. The second and most important problem was the continuous descent during all the lateral displacement. This resulted in adequate performance. Both these problems

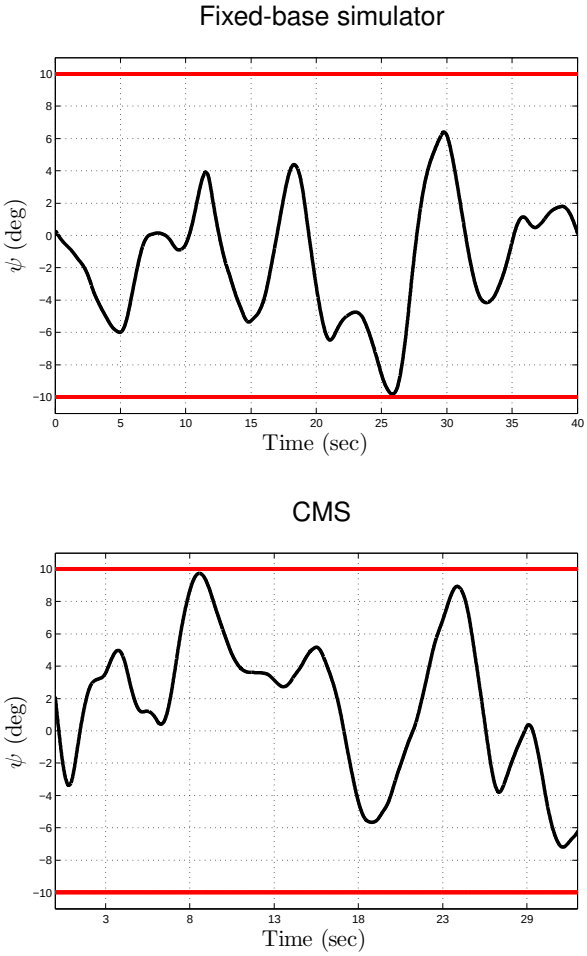

Figure 16: Yaw Euler angle during the entire maneuver

were not present in the CMS where the pilot stopped exactly in front of the lower sphere and stayed well within the performance bounds. In the motion simulator the performance was reached in a desired way.

Heading was maintained in a desired way in both simulators. Figure 16 shows the results.

The time of execution of the entire maneuver was of 35 seconds in the fixed-base simulator and of 31 seconds in the CMS. Since the performance is considered adequate if executed in 25 second, none of the two maneuvers was satisfactory. However the improvement obtained in the CMS suggests that with more training and better motion cueing might make it possible to reach this metric too.

5. CONCLUSIONS

This paper has presented the development and the validation of a fully non-linear helicopter model. The implementation of the model was briefly described.

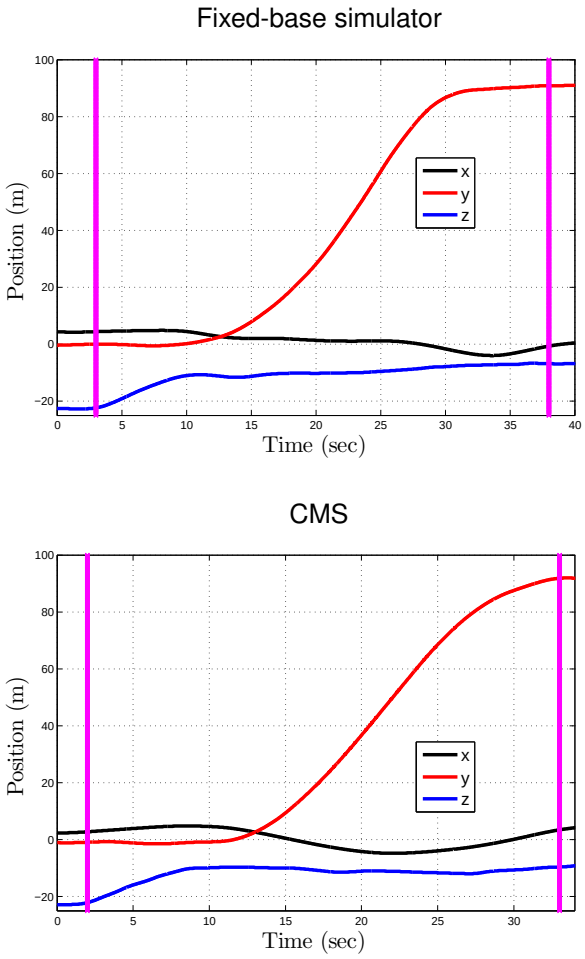

Figure 17: Inertial position along x-,y-,z-axes during the vertical remask maneuver. Two vertical lines indicate when the maneuver starts and when ends

Different kind of tests were done to validate the implemented model. Time and frequency domain tests showed the correctness of the implementation. Furthermore, validation measurements were performed on a fixed-base simulator and a motion simulator which showed favourable results.

Future steps involve further improvements to the model and the use of more pilots for testing. Moreover different MTEs will be tested to really understand the ability of the model to be used as a real helicopter.

ACKNOWLEDGEMENTS

Frank M. Nieuwenhuizen was supported by the myCopter project, funded by the European Commission under the 7th Framework Program (http://www.mycopter.eu).

REFERENCES

[1] Nieuwenhuizen, F. M., Jump, M., Perfect, P., White, M., Padfield, G., Floreano, D., Schill, F., Zufferey, J., Fua, P., Bouabdallah, S., Siegwart, R., Meyer, S., Schippl, J., Decker, M., Gursky, B., Hfinger, M., and Bülthoff, H. H., "myCopter: Enabling Technologies for Personal Aerial Transportation Systems," *3rd International HELI World Conference, Frankfurt/Main*, 2011.

[2] Drop, F. M., Pool, D. M., van Paassan, M. M., Mulder, M., and Bülthoff, H. H., "Feedforward and Feedback Control Behaviour in Helicopter Pilots during a Lateral Reposition Task," *AHS 69th Annual Forum, Phoenix, USA*, 21-23 May 2013.

[3] Olivari, M., Nieuwenhuizen, F. M., Bülthoff, H. H., and Pollini, L., "Pilot Adaptation to Different Classes of Haptic Aids in Tracking Tasks," *Journal of Guidance, Control, and Dynamics*.

[4] Geluardi, S., Nieuwenhuizen, F. M., Pollini, L., and Bülthoff, H. H., "Data Collection for Developing a Dynamic Model of a Light Helicopter," *39th European Rotorcraft Forum, Moscow, Russia*, 3-6 September 2013.

[5] Gula, P. and Gorecki, T., "Design, Experiments and Development of a Polish Unmanned Helicopter ILX-27," *39th European Rotorcraft Forum, Moscow, Russia*, 3-6 September 2013.

[6] Padfield, G. and White, M., "Flight simulation in academia HELIFLIGHT in its first year of operation at the University of Liverpool," *The Aeronautical Journal*, 2003.

[7] Stroosma, O., van Paassen, R., and Mulder, M., "Using the SIMONA Research Simulator for Human-Machine Interaction Research," *AIAA Modeling and Simulation Technologies Conference and Exhibit*, August 11-14 2003.

[8] Padfield, G. D., *Helicopter Flight Dynamics: The Theory and Application of Flying Qualities and Simulation Modelling Second Edition*, Blackwell Publishing, 2007.

[9] Hilbert, K. B., "A Mathematical Model of the UH-60 Helicopter," *NASA TM-85890*, 1984.

[10] Howlett, J. J., "UH-60A Black Hawk Engineering Simulation Program: Volume I - Mathematical Model," *NASA 166309*, 1981.

[11] Dreier, M. E., *Introduction to helicopter and tiltrotor simulation*, AIAA Education Series, 2007.

[12] Banks, C., “Lessons on Helicopter dynamic,” *(http://www.aerojockey.com/papers/helicopter)*.

[13] Li, Y., “Principles of Helicopter Aerodynamic chapter 4,” *(http://www.scribd.com/doc/48524322/Principles-of-Helicopter-Aerodynamics-Chapter-4)*.

[14] Bluman, J. E., *Reducing Trailing Edge Flap Deflection Requirements in Primary Control Through a Moveable Horizontal Tail*, Ph.D. thesis, The Pennsylvania State University, 2008.

[15] Blanken, C. L., Arterburn, D. R., and Cicolani, L. S., “Evaluation of Aeronautical Design Standard-33 Using a UH-60 A Black Hawk,” *AHS 55th Annual Forum, Montreal, Canada*, 25-27 May 1999.

[16] Baskett, B. J., “Aeronautical Design Standard performance specification Handling Qualities requirements for military rotorcraft,” Tech. rep., DTIC Document, 2000.

[17] Geluardi, S., Nieuwenhuizen, F., Pollini, L., and Bülthoff, H. H., “Frequency Domain System Identification of a Light Helicopter in Hover,” *AHS 70th Annual Forum, Montreal, Canada*, 20-22 May 2014.

[18] Zivan, L. and Tischler, M. B., “Development of a Full Flight Envelope Helicopter Simulation Using System Identification,” *Journal of the American Helicopter Society*, Vol. 55, No. 2.

COPYRIGHT STATEMENT